ORIGINAL CONTAINS
COLOR ILLUSTRATIONS

ORIGINAL CONTAINS
COLOR ILLUSTRATIONS

Computational Support of the Lamimar Flow Supersonic Wind Tunnel, CNSFV Code Development, Maglev, and Grid Generation

Goetz H. Klopfer

MCAT Institute
Final Report 95 - 06
January 1995

Corporate Agreement NCC2 - 616

MCAT Institute
3933 Blue Gum Drive
San Jose, CA 95127

Abstract

This final report covers the work done on corporate agreement NCC2-616 over a period of 5 1/2 years. It is broken into three segments of approximately 1 1/2 to 2 years each. The report is a summary report and is not intended to be comprehensive of all the work done under this corporate agreement. A more complete coverage of the work done is obained from the papers and reports listed in the "Papers" section. Additional reporting of significant work was done through "Technical Highlights" and "Research and Technical Summaries". A listing and copies are given in the "Technical Highlights and R and T" section. The work was also reported in a series of seminars, conference meetings, branch reviews, workshops, and project reviews. A list of these talks is given in the "Presentation" section. Also during this time three students ranging from high school to graduate level were supervised. A list of the students and the type of work accomplished is given in the "Mentoring" section. The report concludes with the "Appendices" sections which include the three papers produced during the last 1 1/2 years of this corporate agreement.

Computational Support of the Laminar Flow Supersonic Wind Tunnel, CNSFV Code Development, Maglev, and Grid Generation

Final Report
31 January 1995
Performance Period: 1 June 1989 - 31 January 1995
Nasa-Ames Cooperative Agreement No. NCC 2-616

G.H. Klopfer
MCAT Institute, M/S 258-1, (415) 604-3993
NASA Ames RC, Moffett Field, CA 94035

Section I June 1989 to June 1991

Grid Generation About Complex Three-Dimensional Aircraft Configurations

The study of the aerodynamics about complete aircraft by numerical methods is still limited by two (or more) problems. The first involves the lack of adequate turbulence models applicable to a wide range of flow regimes and the second has to do with obtaining three dimensional grids with sufficient resolution to resolve all the flow or other physical features of interest. This study is concerned with the latter problem.

The generation of a computational grid involves a series of compromises to resolve several conflicting requirements. On one hand one would like the grid to be fine enough and not too skewed to reduce the numerical errors and to adequately resolve the pertinent physical features of the flow field about the aircraft. On the other hand the capabilities of present or even future supercomputers are finite and the number of mesh points must be limited to a reasonable number, one which is usually much less than desired for numerical accuracy.

One technique to overcome this limitation is the 'zonal' grid approach. In this method the overall field is subdivided into smaller zones or blocks in each of which an independent grid is generated with enough grid density to resolve the flow features in that zone. The zonal boundaries or interfaces require special boundary conditions such that the conservation properties of the governing equations are observed. Much work has been done in 3-D zonal approaches with nonconservative zonal interfaces. A 3-D zonal conservative interfacing method that is efficient and easy to implement was developed during the past year.

As originally envisioned, the conservative interfacing was to be developed for finite difference codes which were the most prevalent codes at NASA/Ames. However during the course of the work it became apparent that such a procedure would become rather complicated and that it would be much more feasible to do the conservative interfacing with cell-centered finite volume codes. Accordingly, the CNS code was converted to finite volume form. This new version of the code is named CNSFV. The original multi-zonal interfacing capability of the CNS code was enhanced by generalizing the procedure to allow for completely arbitrarily shaped zones with no mesh continuity between the zones. While this zoning capability works well for most flow situations it is, however, still nonconservative. The conservative interface algorithm has also been implemented.

The results of this work has been reported in reference 1, a paper presented at the 10th AIAA CFD conference held on 24-27 June 1991. This paper essentially covers much of the work done during the first two years of the corporate agreement.

Section II July 1991 to May 1993

CNSFV Code Development, Virtual Zone Navier-Stokes Computations of Oscillating Control Surfaces and Computational Support of the Laminar Flow Supersonic Wind Tunnel,

Abstract

The work performed from mid-1991 to mid-1993 on this corporate agreement covered two major areas and two lesser ones. The two major items included further development and validation of the CNSFV code and providing computational support for the Laminar Flow Supersonic Wind Tunnel (LFSWT). The two lesser items involve a Navier-Stokes simulation of an oscillating control surface at transonic speeds and improving the basic algorithm used in the CNSFV code for faster convergence rates and more robustness. The work done in all four areas was in support of the High Speed Research Program at NASA Ames Research Center.

Introduction

The numerical simulation of the Navier-Stokes equations for complex configuations at realistic flight conditions is still limited by several problems. Included are the lack of adequate grid resolution, robust and efficient flow solvers, transition prediction techniques, and turbulence models. The work covered in this report involves the first three items only. The grid resolution and robust flow solver problems are included in the CNSFV code development work and the transition prediction technique is included in the work involving flow analysis of the laminar flow supersonic wind tunnel currently under development at NASA Ames. The flow analysis is by numerical simulation of the Navier-Stokes equations with the CNSFV code. In the following sections the work performed during this performance period in the four different categories are described in more detail.

CNSFV Code Development

The CNSFV code is a cell-centered finite volume version of the finite difference code, CNS. The reason for developing the finite volume code was to facilitate the implementation of conservative zonal interface boundary condition. The finite difference form is not practical for conservative interfacing. The CNSFV code was originally developed three years ago (see ref. 1) and has been under continuous improvement since its inception. During the past year (1993) further improvements have been made. These include simplifying the type and amount of input data required, implementing general boundary conditions, increasing the code efficiency in terms of vectorization and algorithmic improvements, and developing special zoning capabilities (called virtual zones) to ease the problem of generating grids with multiple zones about complex and dynamic aerodynamic configurations. An example of an application of the virtual zone technology is given in reference 2, where a complete wing-body configuration with control surfaces is simulated with the CNSFV code.

The diagonal ADI algorithm in the original finite difference code is a fast and robust scheme. However when the code was converted to finite volume form a sharp drop in the maximum allowable stable time step was noticed. Various types of local time step scalings were tried and the allowable time steps improved substantially but the time steps originally possible with the finite difference form were never achieved. The scaled allowable time steps were still too small however and the diagonal ADI scheme was replaced with the lower-upper symmetric Gauss Seidel (LU-SGS) scheme. This scheme is unconditional stable and arbitrarily large time steps can now be used. Most of the the work on implementing and validating the LU-SGS scheme in the CNSFV code is reported in an AIAA paper presented at the AIAA Fluid Dynamics Conference, ref.3.

A condensed version of an user's manual (ref. 4) for the CNSFV code has been written.

Computational Support for the LFSWT

During this period computational support has been provided for the Laminar Flow Supersonic Wind Tunnel (LFSWT). The objective of the effort is to develop computational tools so that the design of a test model and its placement within the test section of the LFSWT can be verified by numerical simulation of the Navier-Stokes equations before the model is constructed. For transition studies in the supersonic Mach regime it is important to know the extent of clean and undisturbed flow over the test model.

For the simulation, modified versions of the Upwind Parabolized Navier-Stokes (UPS, ref. 5) and the Compressible Navier-Stokes, Finite Volume (CNSFV) codes were used to solve the thin-layer Navier-Stokes equations for the laminar flow about the test model inside the LFSWT. The surface and flow field grids were generated with GRIDGEN (ref. 6). The faster UPS code was used for the higher Mach numbers investigated and the multi-zonal CNSFV code for the lower supersonic Mach regime.

Computations have been performed of flow fields about a NACA64A010 wing with a 70^0 leading edge sweep mounted on the top wall of the LFSWT for inviscid and viscous flows with the UPS and CNSFV codes, respectively. Various other model locations were studied to verify that the top wall mounted position provides for the largest extent of undisturbed flow on the model. The figure in the first technical highlight shows the inviscid shock pattern obtained with the UPS code. Shown are the impinging shocks on the tunnel walls as well as on the model itself. The undisturbed region on the model is the triangular region in front of the reflected shock wave impinging on the model. The flowfield behind the impinging shock wave is no longer undisturbed and, hence, that part of the model behind the shock is useless for any natural transition study.

Another series of computations were carried out on the NACA64A010 wing with four different leading edge sweep angles. The mean flow results were used to validate a Parabolized Stability Equation (PSE) code being developed by another group. In addition a full scale sized portion of the F16XL2 passive glove was gridded and a flow solution initiated in preparation for the wind tunnel tests scheduled for early 1994. The results of the computations were used to design the wind tunnel model of the F16XL2 wing. The wind tunnel tests are designed to validate the wind tunnel with flight tests.

An accurate prediction of the flow field inside the LFSW with various test models is important for maximizing the usefulness of the tunnel, especially when relatively small test sections are considered. Numerical simulations can also be used for designing tunnel modification and innovative passive and active tunnel devices to minimize the impact of reflected waves on the test model. This is a cost-effective means of increasing the usable size of the LFSWT.

Virtual Zone Navier-Stokes Computations of Oscillating Control Surfaces

Another area of effort conducted during the past year was to implement the virtual zone concept into a time accurate finite difference code, ENSAERO (ref. 7), for application to an oscillating control surface mounted on a clipped delta wing at transonic speeds. For a time accurate computation it is essential that the search procedure to find the interpolation coefficients for the inter-zonal communication be at least as efficient as the flow solver. Otherwise the code is not practical enough for routine use. Much of the work involved developing more efficient search procedures. The results of this effort were presented at the AIAA 11th CFD Meeting (ref. 8).

Algorithm Development

As mentioned in the CNSFV code development section, the LU-SGS scheme is unconditionally stable. However it does suffer slower convergence rates with increasing Reynolds number for viscous dominated flows. For this reason several modifications of the basic LU-SGS scheme were implemented. This work was initiated during this period and the results are reported in the section for the next performance period.

Section III June 1993 to January 1995

Computational Support of the Laminar Flow Supersonic Wind Tunnel, CNSFV Code Development, Maglev, and Grid Generation

Abstract

The work done in the last period of the corporate aggreement covered four major areas: computational support for the Laminar Flow Supersonic Wind Tunnel (LFSWT), further CNSFV code development, an example of dual use technology of CFD for the aerodynamic analysis of the magnetic flight vehicle (Maglev), and grid generation as needed for the LFSWT and Maglev efforts.

Computational Support for the LFSWT

The computational support for the Laminar Flow Suppersonic Wind Tunnel involved several facets. The primary one required CFD nalysis of of full scale F16xl-2 wing to ascertain the tunnel blockage and extend of clean flow in the test section. Since the LFSWT test section is quite small (8 in. high by 16 in. wide by 36 in. long) and the mean chord length of the F16xl-2 wing is approximately 200 in., just a small portion of the leading edge of the wing could be accommodated in the tunnel. Furthermore to prevent blockage effects the wing section had to be modified to reduce the section thickness. The CFD effort consisted of defining the surface shape of the test model, defining the surface grid and generating the volume grid including the wind tunnel walls, and doing a series of Navier- Stokes and Euler simulations to find the best model size and placement to optimize the usable size of the available test section.

Another facet of the effort was to provide numerical validation of the test results of the final F16xl-2 model at various angles of attack. Since the F16xl-2 wing design is considered proprietary, these results are not shown here. The agreement between the test results and numerical predictions are very good except where spurious shock waves emanating from various locations in the wind interfer with the model. These shock waves are not considered in the numerical simulations.

A third facet of the research is to provide CFD tools needed for predicting the transition from laminar to turbulent flow in the wind tunnel. Most of this effort involved developing better algorithms for the mean flow Navier-Stokes solver (CNSFV) to obtain better and faster convergence rates and more accurate results. This effort was critical since the flow is predominantly laminar, which is very slow to converge to a fully developed boundary layer due to the low levels of physical dissipation. Increasing the numerical dissipation levels distorted the boundary layer properties needed for transition predections. The main effort was to investigate several different modifications to the LU-SGS scheme. Several versions were successful for 2-d flows but did not carry over to 3-d flows. These results were reported in ref. 9. The paper in included in Appendix B.

The other results obtained under the LFSWT effort were reported on a periodic basis, namely monthly LFSWT reviews and semi-annual High Speed Research (HSR) Research and Technology (R and T) reviews. This work is still underway and will be documented at the completion of this effort.

Maglev

Another study carried out during this performance period was an numerical aerodynamic prediction of a ground-based transportation system. This is a good example of a dual-use technology. CFD tools developed for predicting aerodynamics about aircraft used for other applications. Since the flow regimes are quite different between aircraft and ground-based vehicles, some further development of the CFD tools was necessary; mostly in the turbulence modelling and in the volume gridding and blocking. Most of the details of this work are given in ref. 10. The paper is included in Appendix C.

Grid Generation

Much of the work in the LFSWT and the Maglev effort involved generating the surface definitions, generating the surface grids, setting up the grid blocking structure, and finally generating the volume grids. Flow simulations are then performed. If the flow results are inadequate on these grids, then the grids are adjusted until the numerical results are sufficiently accurate for th erequired needs. Dave Baker, a graduate student at Cal Poly helped with the gridding effort. A grid quality study was also conducted by Kevin Okamoto, a graduate student at UC Davis.

References

1. Klopfer, G. H. and Molvik, G. A.; "Conservative Multizonal Interface Algorithm for the 3-D Navier-Stokes Equations", AIAA Paper 91-1601, AIAA 10th CFD Conference, 24-27 June 1991, Honolulu, Hawaii.

2. Chaussee, D. S. and Klopfer, G. H.; "The Numerical Study for 3-D Flow Past Control Surfaces," AIAA Paper 92-4650, August 1992.

3. Klopfer, G. H. and Yoon, S.; "Multi-Zonal Navier-Stokes Code with the LU-SGS Scheme," AIAA Paper 93-2965, AIAA 24th Fluid Dynamics Conference, 6-9 July 1993, Orlando, Florida.

4. Klopfer, G. H.; "Preliminary Version of User's Manual for CNSFV," MCAT Report, May 1993.

5. Lawrence, S. L.; "Development of a Three-Dimensional Upwind Parabolized Navier-Stokes Code," AIAA J., Vol. 26, No. 6, June 1990, pp. 971-972.

6. Steinbrenner, J. P., Chawner, J. R., and Fouts, C. L.; "The GRIDGEN 3D Multiple Block Grid Generation System, Vol. I, Final Report," General Dynamics Corporation, WRDC-TR-90-3022, July 1990.

7. Obayashi, S. and Guruswamy, G. P.; "Navier-Stokes Computations for For Oscillating Control Surfaces," AIAA Paper 92-4431, August 1992.

8. Klopfer, G. H. and Obayashi, S.; "Virtual Zone Navier-Stokes Computations For Oscillating Control Surfaces," AIAA Paper 93-3363, AIAA 11th CFD Conference, 6-9 July 1993, Orlando, Florida.

9. Klopfer, G. H. and Kontinos, D. A.; "A Modified LU-SGS Scheme for High Reynolds' Number Navier-Stokes Flows," AIAA Paper 94-2356, AIAA 25th Fluid Dynamics Conference, June 1994, Colorado Springs, Colorado. (paper withdrawn)

10. Klopfer, G. H. and Mehta, U. B.; "Aerodynamic Computations for a High-Speed, Magnetic-Flight System," AIAA Paper 95-0749, AIAA 33rd Aerospace Sciences Meeting and Exhibit, January 1995, Reno, Nevada.

Papers

1. Klopfer, G. H. and Molvik, G. A.; "Conservative Multizonal Interface Algorithm for the 3-D Navier-Stokes Equations", AIAA Paper 91-1601, AIAA 10th CFD Conference, 24-27 June 1991, Honolulu, Hawaii.

2. Chaussee, D. S. and Klopfer, G. H.; "The Numerical Study for 3-D Flow Past Control Surfaces," AIAA Paper 92-4650, August 1992.

3. Klopfer, G. H. and Yoon, S.; "Multi-Zonal Navier-Stokes Code with the LU-SGS Scheme," AIAA Paper 93-2965, AIAA 24th Fluid Dynamics Conference, 6-9 July 1993, Orlando, Florida.

4. Klopfer, G. H.; "Preliminary Version of User's Manual for CNSFV," MCAT Report, May 1993.

5. Klopfer, G. H. and Obayashi, S.; "Virtual Zone Navier-Stokes Computations For Oscillating Control Surfaces," AIAA Paper 93-3363, AIAA 11th CFD Conference, 6-9 July 1993, Orlando, Florida.

6. Klopfer, G. H. and Obayashi, S.; "Virtual Zone Navier-Stokes Computations For Oscillating Control Surfaces," Fourteenth International Conference on Numerical Methods in Fluid Dynamics, 11-15 July 1994, Bangalore, India.

7. Klopfer, G. H. and Kontinos, D. A.; "A Modified LU-SGS Scheme for High Reynolds' Number Navier-Stokes Flows," AIAA Paper 94-2356, AIAA 25th Fluid Dynamics Conference, June 1994, Colorado Springs, Colorado. (paper withdrawn)

8. Klopfer, G. H. and Mehta, U. B.; "Aerodynamic Computations for a High-Speed, Magnetic-Flight System," AIAA Paper 95-0749, AIAA 33rd Aerospace Sciences Meeting and Exhibit, January 1995, Reno, Nevada.

Other Papers and Publications

9. Klopfer, G. H. and Nixon, D.; "Transonic Flows with Vorticity Transport Around Slender Bodies," Technical Notes, AIAA Journal, Vol. 27, No. 10, October 1989, pp. 1461-1464.

10. Nixon, D., Caruso, S. C., and Klopfer, G. H.; "Prediction of Transonic Flow with Vortex Effects," AIAA Paper 90-0389, AIAA 28rd Aerospace Sciences Meeting, January 1990, Reno, Nevada.

11. Nixon, D., Reisenthel, P. H., Torres, T. O., and Klopfer, G. H.; "Prediction of Unsteady Transonic Flow Around Missile Configurations," 31st AIAA/ASME/ASCE/AHS/ASC Structures, Structural Dynmaics and Materials Conference, April 1990, Long Beach, Callifornia.

12. Yee, H. C., Klopfer, G. H. and Montagne, J.-L.; "High-Resolution Shock-Capturing Schemes for Inviscid and Viscous Hypersonic Flows," Journal of Computational Physics, Vol. 88, 1990, pp. 31-61.

Presentations

1. Klopfer, G. H.; "Solution Adaptive Hyperbolic Grid Generation," NASA Ames RFA Grid Generation Seminar Series, September 1989, Moffett Field, CA.

2. Klopfer, G. H.; "Improved Initial Convergence Rates for ARC2D/ARC3D Codes," RFA Code Efficiency Workshop, 25 June 1990, NASA Ames Research Center, Moffett Field, CA.

3. Klopfer, G. H.; "Advanced Aircraft Project - AAP, CFD Tools Development," NASA Ames RFA Branch Review, 27 February 1991, Moffett Field, CA.

4. Klopfer, G. H. and Molvik, G. A.; "Conservative Multizonal Interface Algorithm for the 3-D Navier-Stokes Equations", NASA/OAET CFD Conference, NASA Ames Research Center, 12-14 March 1991, Moffett Field, CA.

5. Klopfer, G. H. and Molvik, G. A.; "Conservative Multizonal Interface Algorithm for the 3-D Navier-Stokes Equations", AIAA Paper 91-1601, AIAA 10th CFD Conference, 24-27 June 1991, Honolulu, Hawaii.

6. Klopfer, G. H.; "Patched Grid Schemes," Aerophysics Computational Fluid Dynamics Program, Peer Review, NASA Ames Research Center, 17-20 November 1992, Moffett Field, CA.

7. Klopfer, G. H.; "CNSFV - Code Development and Applications," RFA Branch Review, Nasa Ames Research Center, 22-24 March 1993, Moffett Field, CA.

8. Klopfer, G. H.; "CFD Support for Laminar Flow Supersonic Wind Tunnel," HSR SLFC Research and Technology Review, NASA Ames Research Center, 30 September 1993, Moffett Field, CA.

9. Klopfer, G. H.; "CFD Support for Laminar Flow Supersonic Wind Tunnel," HSR SLFC Research and Technology Review, NASA Ames Research Center, 23 May 1994, Moffett Field, CA.

Presentations (concluded)

10. Klopfer, G. H., Garcia, J., and Baker, M. D.; "CFD Support for Laminar Flow Supersonic Wind Tunnel," LFSWT CFD Review, NASA Ames Fluid Mechanics Laboratory, 2 June 1994, Moffett Field, CA.

11. Klopfer, G. H. and Yoon, S.; "Multi-Zonal Navier-Stokes Code with the LU-SGS Scheme," AIAA Paper 93-2965, AIAA 24th Fluid Dynamics Conference, 6-9 July 1993, Orlando, Florida.

12. Klopfer, G. H. and Obayashi, S.; "Virtual Zone Navier-Stokes Computations For Oscillating Control Surfaces," AIAA Paper 93-3363, AIAA 11th CFD Conference, 6-9 July 1993, Orlando, Florida.

13. Klopfer, G. H. and Obayashi, S.; "Virtual Zone Navier-Stokes Computations For Oscillating Control Surfaces," Fourteenth International Conference on Numerical Methods in Fluid Dynamics, 11-15 July 1994, Bangalore, India, (presented by Roger Strawn).

14. Klopfer, G. H.; "A Modified LU-SGS Scheme for High Reynolds' Number Navier-Stokes Flows," NASA Ames RFC Seminar Series, September 1994, Moffett Field, CA.

15. Klopfer, G. H. and Mehta, U. B.; "Aerodynamic Computations for a High-Speed, Magnetic-Flight System," AIAA Paper 95-0749, AIAA 33rd Aerospace Sciences Meeting and Exhibit, January 1995, Reno, Nevada.

Technical Highlights

1. Klopfer, G. H.; "Computational Verification for the Laminar Flow Supersonic Wind Tunnel," November 1992.
2. Klopfer, G. H. and Yoon, S.; "Comparison of the LU-SGS and Diagonal Beam-Warming Schemes for Viscous Compressible Flows," March 1993.

TECHNICAL HIGHLIGHT

Computational Verification for the Laminar Flow Supersonic Wind Tunnel

G.H. Klopfer
MCAT Institute, Computational Aerosciences Branch
Ext. 4-3993 November 1992
RTOP 537-03-23
Code RF

Research Objective

The objective is to develop computational tools so that the design of a test model and its placement within the test section of the Laminar Flow Supersonic Wind Tunnel (LFSWT) can be verified by numerical simulation of the Navier-Stokes equations before the model is constructed. For transition studies in the supersonic Mach regime it is important to know the extent of clean and undisturbed flow over the test model.

Approach

Modified versions of the Upwind Parabolized Navier-Stokes (UPS) and the Compressible Navier-Stokes, Finite Volume (CNSFV) codes were used to solve the thin-layer Navier-Stokes equations for the laminar flow about the test model inside the LFSWT. The surface and flowfield grids were generated with GRIDGEN. The faster UPS code was used for the higher Mach numbers investigated and the multi-zonal CNSFV for the lower supersonic Mach regime.

Accomplishment Description

Computations have been performed for a NACA64A010 wing with a 70^o leading edge sweep mounted on the top wall of the LFSWT at $M_\infty = 1.6$ for inviscid and viscous flows with the UPS and CNSFV codes, respectively. Various other model locations were studied to verify that the top wall mounted position provides for the largest extent of undisturbed flow on the model. The accompanying figure shows the inviscid shock pattern obtained with the UPS code. Shown are the impinging shocks on the tunnel walls as well as on the model itself. The undisturbed region on the model is the triangular region in front of the reflected shock wave impinging on the model. The flowfield behind the impinging shock wave is no longer undisturbed and, hence, that part of the model behind the shock is useless for any natural transition study.

Significance of Accomplishment

An accurate prediction of the flowfield inside the LFSWT with various test models is important for maximizing the usefulness of the tunnel, especially when relatively small test sections are considered. Numerical simulation can also be used for designing tunnel modifications and innovative passive and active tunnel devices to minimize the impact of reflected shock waves on the test model. This is a cost-effective means of increasing the usable size of the LFSWT.

Future Plans

The CNSFV code and technique described above will be extended to unsteady flows to study test model blockage and tunnel unstart problems.

LAMINAR FLOW SUPERSONIC WIND TUNNEL

INVISCID SHOCK PATTERN of 70°SWEEP NACA64a010 WING @ Mach = 1.6

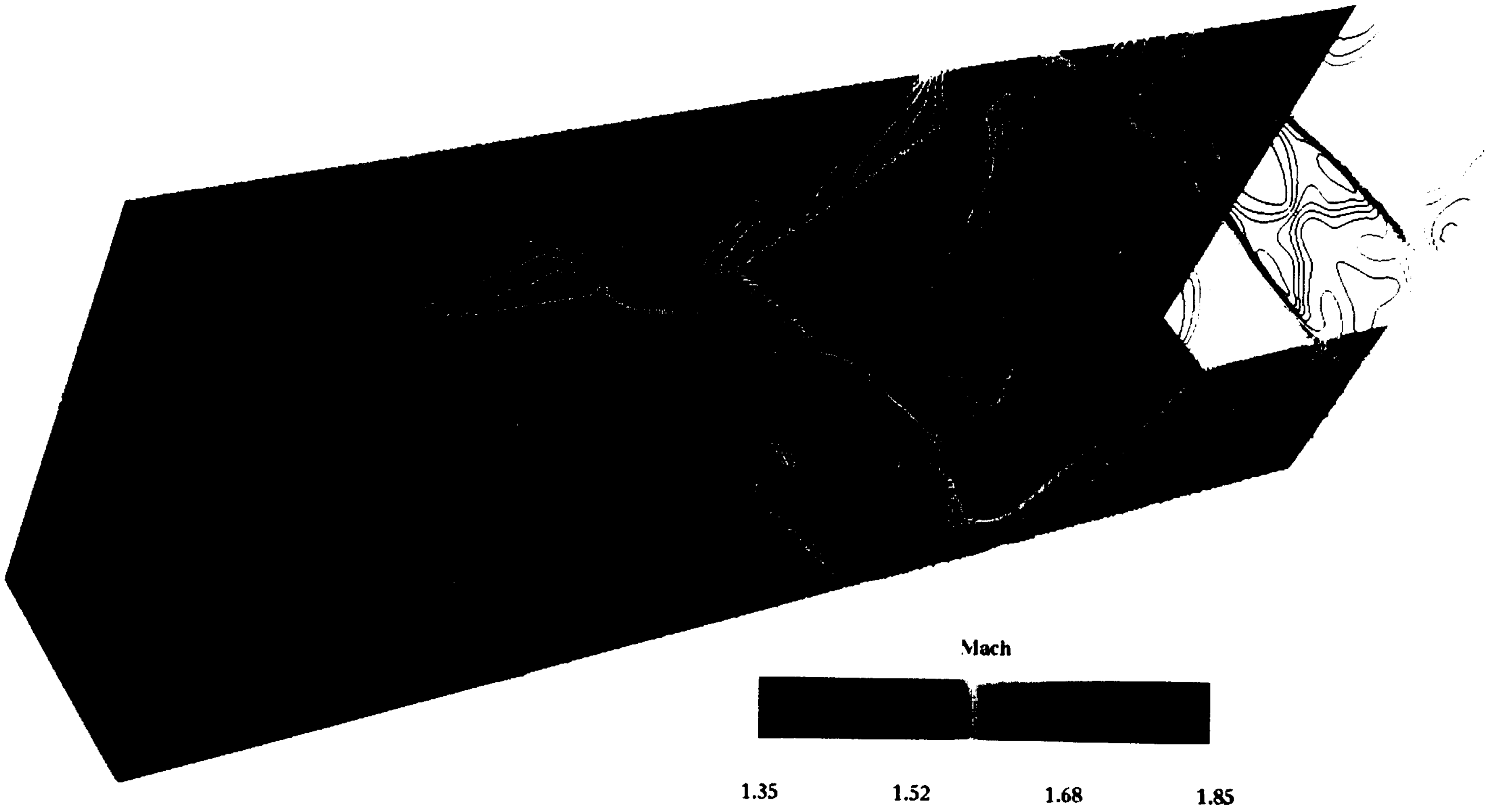

NASA - Ames RC 10/92

ORIGINAL PAGE
COLOR PHOTOGRAPH

TECHNICAL HIGHLIGHT

Comparison of the LU-SGS and Diagonal Beam-Warming Schemes for Viscous Compressible Flows

G.H. Klopfer and S. Yoon
MCAT Institute, Computational Aerosciences Branch
Ext. 4-3993 March 1993
RTOP 537-03-23
Code RF

Research Objective

It is well known that the finite volume form of the diagonal Beam-Warming scheme has a time step restrictions. For constant time steps, the largest CFL numbers are less than ten. With judicious time step scaling, the maximum CFL can be as high as 75. For numerical simulation of a realistic aerodynamic configuration, several dozen zones may be required and much user input is required to determine the optimum time step and time step scaling. Furthermore for simulations of unsteady viscous flows a constant time step is required and the allowable CFL of 10 is much too low for such a simulation to be practical. The objective of the present work is to utilize an alternative algorithm to the diagonal Beam-Warming scheme in the three-dimensional compressible Navier-Stokes code, CNSFV, so that the severe time step restriction is avoided. For steady flows, larger time steps will allow faster convergence to steady state. For unsteady flow the time step restriction will be based solely on accuracy considerations, rather than algorithmic limitations.

Approach

The LU-SGS (lower upper symmetric Gauss Seidel) algorithm has unconditional linear stablility. Hence this scheme is implemented in the CNSFV code and validated by simulating a transonic turbulent flow around the ONERA M6 transport wing.

Accomplishment Description

Computations have been performed for the ONERA M6 wing at $M_\infty = 0.8339$, $\alpha = 3.06^0$, and $Re_{mac} = 11.72 \times 10^6$ for turbulent flows with both the diagonal ADI and the LU-SGS schemes in the CNSFV code. The turbulence model is Baldwin-Lomax model. The grid consists of four zones with a total mesh size of $193 \times 49 \times 35$ points. The normal grid spacing at the wing surface is $y^+ \simeq 3$. The steady state results obtained with both schemes are indistinguishable and compared to experimental results as shown in the figure. However the computational cost for the LU-SGS has been reduced by a factor of two. The actual CFL numbers run with the LU-SGS scheme were $> 2 \times 10^5$ and no time step scaling was necessary.

Significance of Accomplishment

A multi-zonal compressible Navier-Stokes code has been improved by replacing the diagonal ADI algorithm with the LU-SGS scheme. With the new scheme the code is now much more robust, requires no user intervention to determine the optimum time step or time step scaling, converges faster, and requires only half the cpu time to obtain the same convergence level.

Future Plans

The CNSFV code and LU-SGS algorithm will be extended to unsteady flows to take advantage of the unconditional stability of the scheme. For steady flows, a multi-grid scheme will also be incorporated to obtain another factor of two to three in the convergence rate.

Reference

Klopfer, G.H. and Yoon, S.; AIAA Paper 93-2965, Orlando, Fla, July 1993.

VALIDATION OF THREE-DIMENSIONAL NAVIER-STOKES CODE, CNSFV

CONVERGENCE RATE COMPARISON BETWEEN LU-SGS AND DIAGONAL ADI SCHEMES

ONERA M6 WING
MACH 0.84
Re/mac 11.7×10^6
ANGLE OF ATTACK 3.06^0

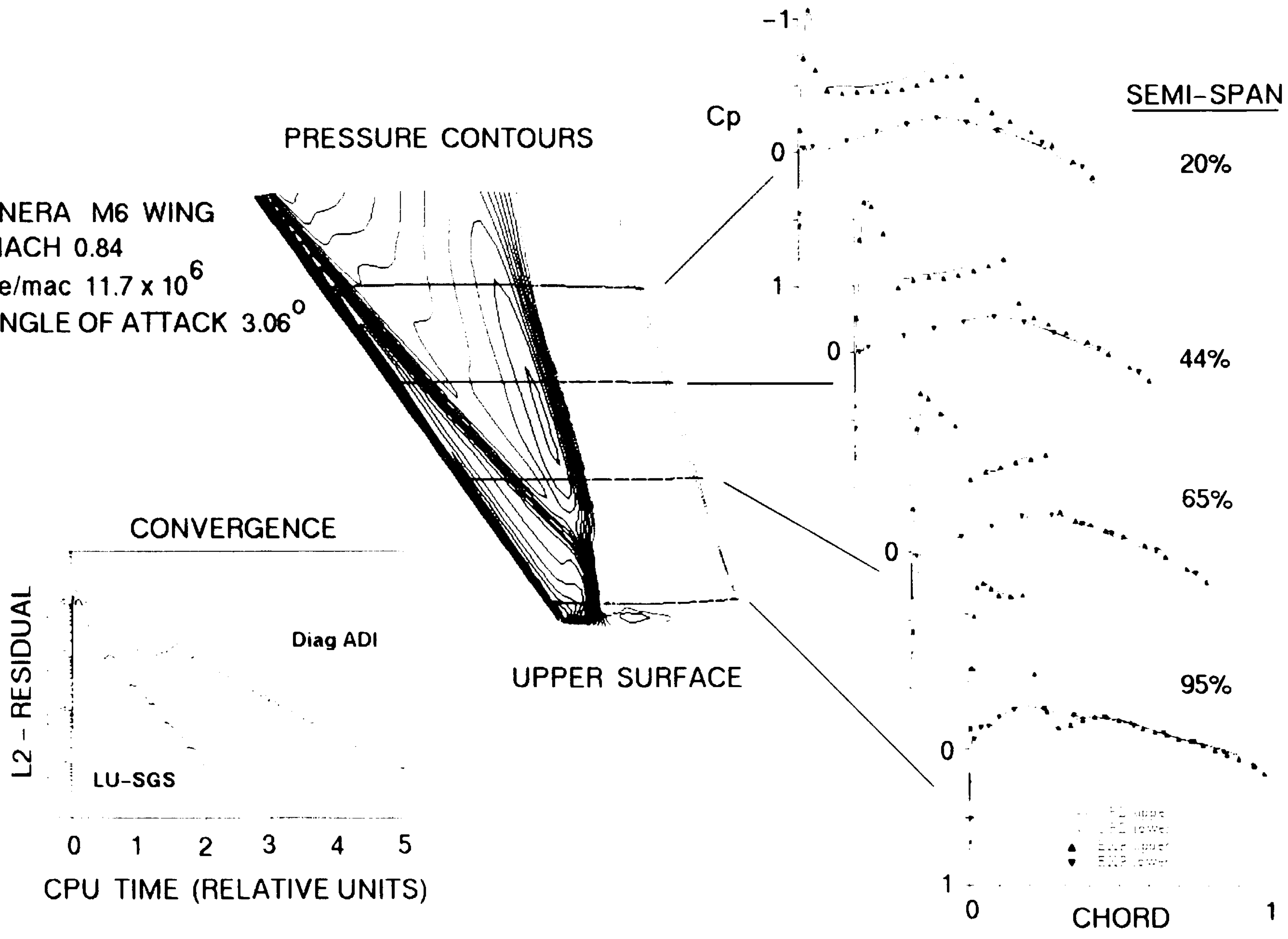

Research and Technology 1992 to 1994

1. Klopfer, G. H.; "Computational Verification for the Laminar Flow Supersonic Wind Tunnel," 1992.
2. Klopfer, G. H. and Yoon, S.; "The LU-SGS Scheme for a Viscous Compressible Flow Code," 1993.
3. Klopfer, G. H.; "F16xl-2 Model Design for the Laminar Flow Supersonic Wind Tunnel," 1993.
4. Mehta, U. and Klopfer, G. H.; "Magnetic Flight of a Vehicle," 1994.

'92 ?

Computational Verification for the Laminar Flow Supersonic Wind Tunnel

G.H. Klopfer

Computational tools were developed so that the design of a test model and its placement within the test section of the Laminar Flow Supersonic Wind Tunnel (LFSWT) could be verified by numerical simulation of the Navier-Stokes equations before the model is constructed. For transition studies from laminar to turbulent flow in the supersonic Mach regime it is important to know the extent of clean and undisturbed flow over the test model.

Modified versions of the Upwind Parabolized Navier-Stokes (UPS) and the Compressible Navier-Stokes, Finite Volume (CNSFV) codes were used to solve the thin-layer Navier-Stokes equations for the laminar flow about the test model inside the LFSWT. The faster UPS code was used for the higher Mach numbers investigated and the multi-zonal CNSFV for the lower supersonic Mach regime.

Computations have been performed for a NACA64A010 wing with a 70 degree leading edge sweep mounted on the top wall of the LFSWT at Mach 1.6 for inviscid and viscous flows with the UPS and CNSFV codes, respectively. Various other model locations were studied to verify that the top wall mounted position provides for the largest extent of undisturbed flow on the model. The accompanying figure shows the inviscid shock pattern obtained with the UPS code. Shown are the impinging shocks on the tunnel walls as well as on the model itself. The undisturbed region on the model is the triangular region in front of the reflected shock wave impinging on the model. The flowfield behind the impinging shock wave is no longer undisturbed and, hence, that part of the model behind the shock is not useful for any natural transition study.

The accurate prediction of the flowfield inside the LFSWT with various test models is important for maximizing the usefulness of the tunnel, especially when relatively small test sections are considered. Numerical simulation can also be used for designing tunnel modifications and innovative passive and active tunnel devices to minimize the impact of reflected shock waves on the test model. This is a cost-effective means of increasing the usable size of the LFSWT.

Ames-Moffett contact: G. H. Klopfer
(415) 604-3993 or FTS 464-3993
Headquarters program office: OAST

Figure Caption:

Computed shock waves on a test model at Mach 1.6 in the Laminar Flow Supersonic Wind Tunnel

LAMINAR FLOW SUPERSONIC WIND TUNNEL

INVISCID SHOCK PATTERN of 70°SWEEP NACA64a010 WING @ Mach = 1.6

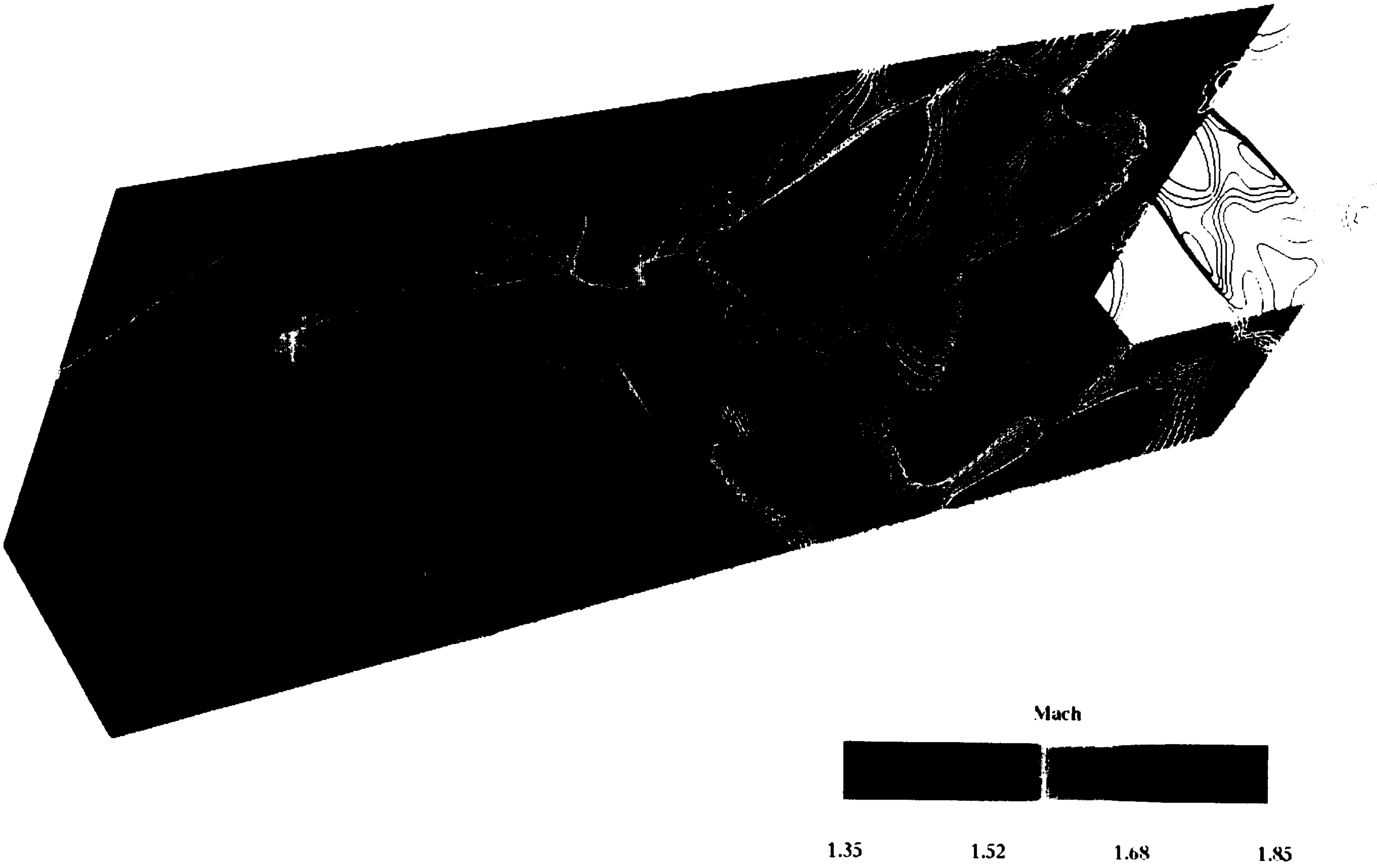

KLOPFER Figure 1

1993

The LU-SGS Scheme for a Viscous Compressible Flow Code

G. H. Klopfer and S. Yoon

It is well known that the finite volume form of the diagonal Beam-Warming scheme has a time step restriction. For constant time steps, the largest Courant-Friedrichs-Levy (CFL) numbers are less than ten. The CFL number is a nondimensional time step. With judicious time step scaling, the maximum CFL can be as high as 75. For numerical simulation of a realistic aerodynamic configuration, several dozen zones may be required and much user input is required to determine the optimum time step and time step scaling. Furthermore when simulating unsteady viscous flows a constant time step is required and the allowable CFL of 10 is much too low for such a simulation to be practical. The objective of the present work is to utilize an alternative algorithm to the diagonal Beam-Warming scheme in the three-dimensional compressible Navier-Stokes code, CNSFV, so that the severe time step restriction is avoided. For steady flows, larger time steps will allow faster convergence to steady state. For unsteady flow the time step restriction will be based solely on accuracy considerations, rather than algorithmic limitations. The LU-SGS (lower upper symmetric Gauss Seidel) algorithm has unconditional linear stablility. Hence this scheme is implemented in the CNSFV code and validated by simulating a transonic turbulent flow around the ONERA M6 transport wing.

Computations have been performed for the ONERA M6 wing at Mach 0.8339, angle of attack of 3.06 degrees, and Reynolds number of 11.72 million for turbulent flows with both the diagonal ADI and the LU-SGS schemes in the CNSFV code. The turbulence model is Baldwin-Lomax model. The grid consists of four zones with a total mesh size of 193 by 49 by 35 points. The normal grid spacing at the wing surface is sufficiently fine to resolve the viscous sublayer. The steady state results obtained with both schemes are indistinguishable and compared to experimental results as shown in the figure. However the computational cost for the LU-SGS has been reduced by a factor of two. The actual CFL numbers run with the LU-SGS scheme were 200,00 and no time step scaling was necessary.

A multi-zonal compressible Navier-Stokes code has been improved by replacing the diagonal ADI algorithm with the LU-SGS scheme. With the new scheme the code is now much more robust, requires no user intervention to determine the optimum time step or time step scaling, converges faster, and requires only half the cpu time to obtain the same convergence level.

Ames-Moffett Contact: G. H. Klopfer

(415) 604-3993 or FTS 464-3993

Headquarters Program Office: OAST

Figure Caption: Comparison of the LU-SGS and Diagonal Beam-Warming Schemes and CNSFV Code Validation.

VALIDATION OF THREE-DIMENSIONAL NAVIER-STOKES CODE, CNSFV

CONVERGENCE RATE COMPARISON BETWEEN LU-SGS AND DIAGONAL ADI SCHEMES

ONERA M6 WING
MACH 0.84
Re/mac 11.7 x 10^6
ANGLE OF ATTACK 3.06°

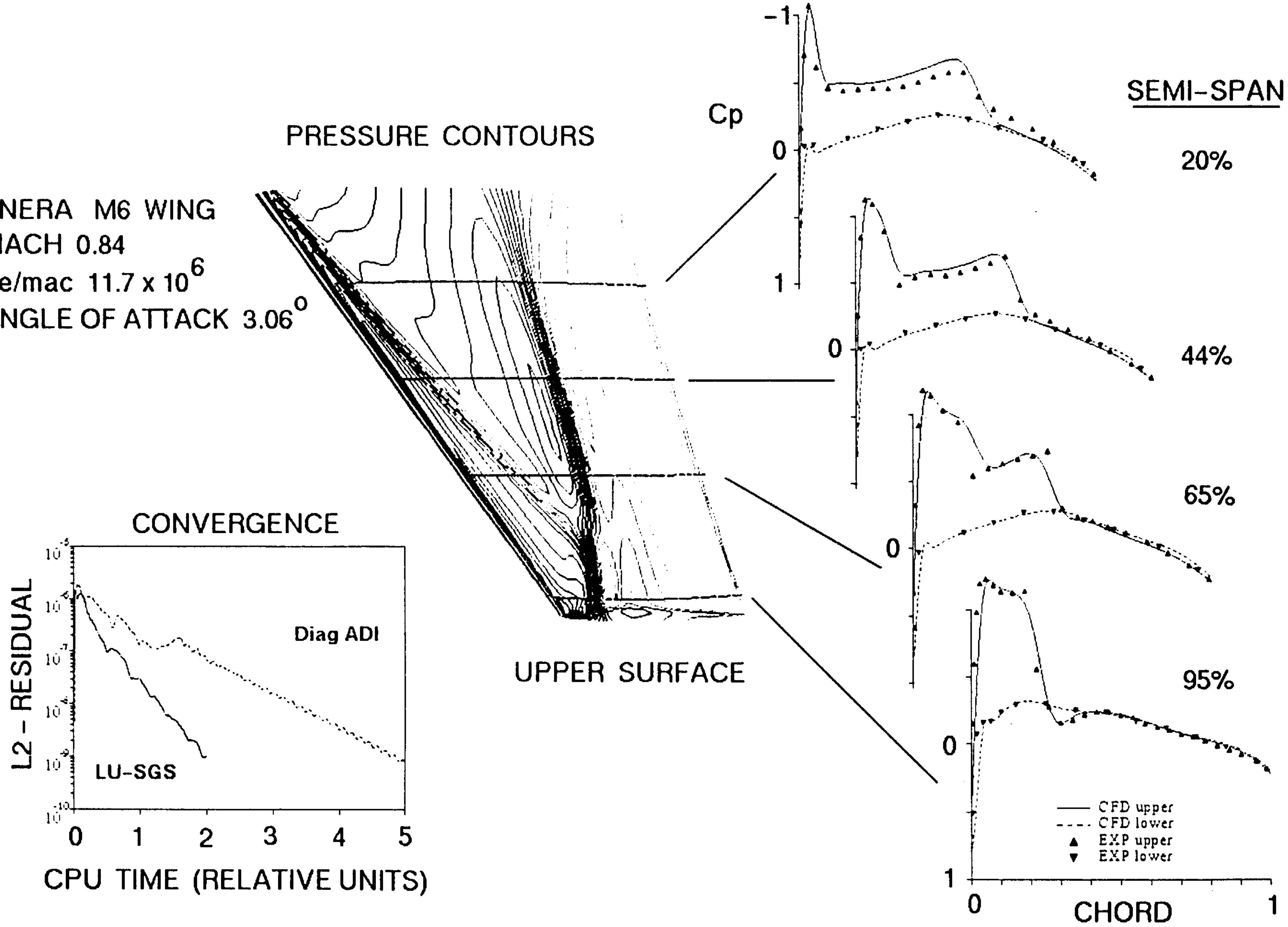

1993

F16XL-2 Model Design for the Laminar Flow Supersonic Wind Tunnel

G. H. Klopfer

Supersonic Laminar Flow Control (SLFC) is currently being researched to assess the feasibility of utilizing active and passive techniques to achieve laminar flow over a supersonic transport. If successful, SLFC has the potential to significantly reduce the drag and, therefore, increase the efficiency of future transport aircraft. The elements within the SLFC program include flight testing, wind-tunnel testing and computational fluid dynamics (CFD) research. These three elements form a "triad" of research which, ultimately, will contribute to the successful design and development of the next generation supersonic transport.

One of the activities within the CFD research element is computational support of wind-tunnel design and testing. A full scale test model of a portion of the passive glove of the F16XL Ship 2 was designed and its placement within the test section of the Laminar Flow Supersonic Wind Tunnel (LFSWT) was verified by numerically simulating the flow field with a Navier-Stokes code. The test section of the LFSWT is limited in size and it is important to design the model to fit in the tunnel to ensure that the tunnel operates in the laminar flow mode without any unstart problems. Only the leading edge portion of the passive glove needs to be modeled at full scale and numerical simulation is a cost effective way of designing the model and guaranteeing proper tunnel operation before the model is constructed. For transition studies from laminar to turbulent flow in the supersonic flight regime it is important to know the extent of clean and undisturbed flow over the test model. The extent of clean flow over the model is determined by the placement of the model in the tunnel test section as well as the proper design of splitter plates to eliminate shock wave interference on the model.

The figure depicts a planform view of the F16XL Ship 2 flight test vehicle, the passive glove as well as the portion of the passive glove that fits inside the test section of the LFSWT. In spite of the small portion of the wing being modeled for ground-based experiments, the size of the wing model is adequate since natural transition at flight conditions occurs within the first two percent of wing chord. The model encompasses 8 to 10 percent of chord of the full scale wing. However the wing thickness at 8 percent chord is thick enough to cause tunnel blockage problems. For this reason the lower surface of the test model is modified by reshaping to keep the tunnel blockage under 10 percent. For transition studies the leading edge and the upper surface of the wing are of primary interest and modification of the lower surface has negligible effect on the transition front location as can be verified by numerical prediction.

Ames-Moffett Contact: G. H. Klopfer
(415) 604-3993 or FTS 464-3993
Headquarters Program Office: OAST

Figure Caption: Planform view of the F16XL Ship 2 aircraft, passive glove and portion of passive glove modeled for the Laminar Flow Supersonic Wind Tunnel.

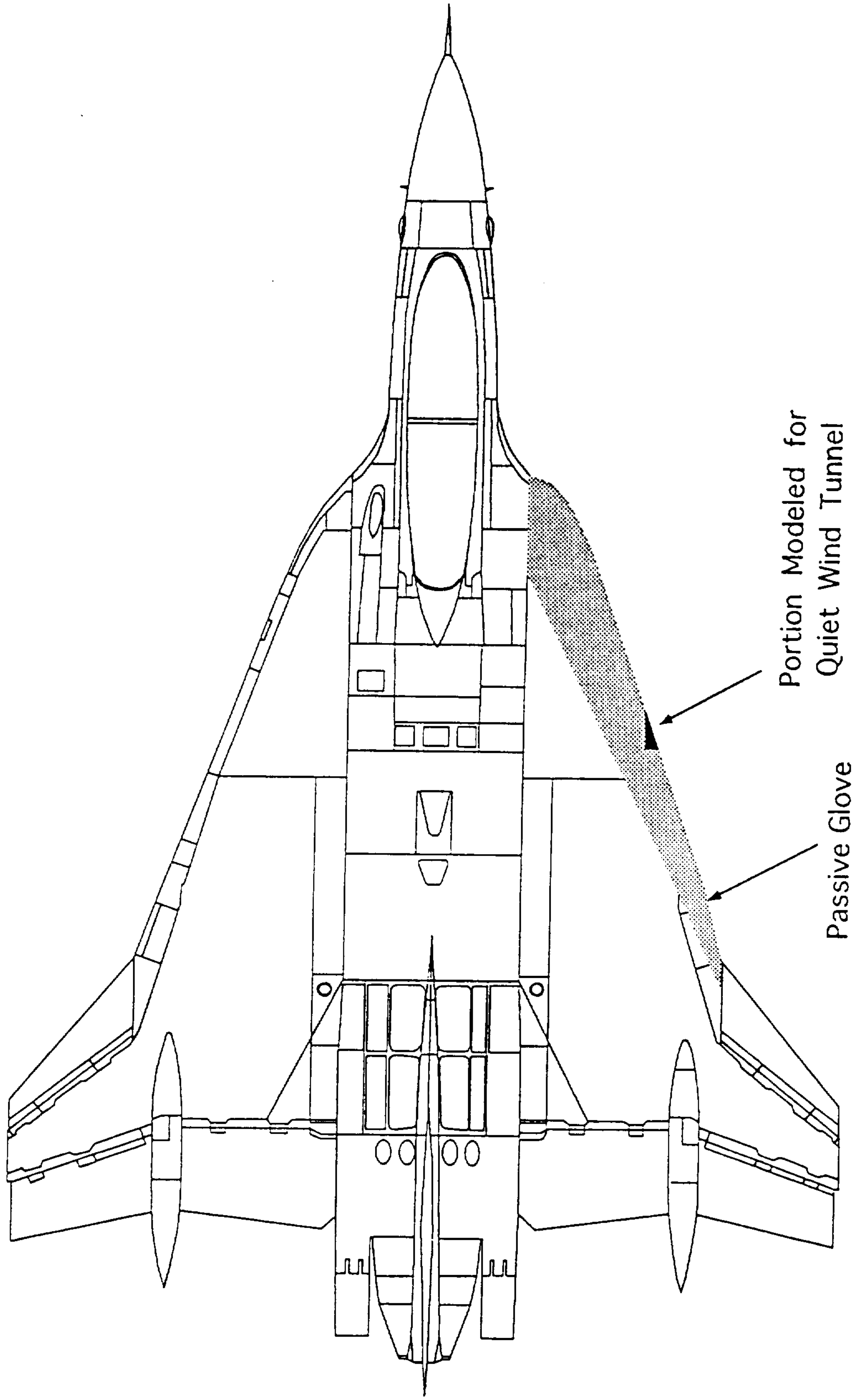
Portion Modeled for
Quiet Wind Tunnel
Passive Glove

1594

Magnetic Flight of a Vehicle

Unmeel Mehta, Goetz Klopfer

A magnetically propelled system that ``flies" may lead to a revolutionary progress in transportation. The system is off the ground, that is, it flies because of magnetic lift. This levitation technique requires the system to fly very close to the ground. High-speed, magnetic flight (magflight) vehicles glide above their guideways, suspended, guided, and propelled by magnetic forces. The possible rationale for magflight studies at NASA are the following: i) space opportunities are offered by launching earth-to-orbit systems with magflight based catapults; ii) aeronautics opportunities are provided for conducting hypersonic research by launching research vehicle with magflight catapults and by using magflight test tracks; and iii) commercial opportunity is the possibility of the high-speed, magflight ground transportation system.

Magflight has technical risks associated with vehicle/guideway interactions, guidance and control, and noise issues, with can be addressed only by aerospace technologies. These interaction issues and adverse effects of aerodynamic forces and moments require state-of-the-art computational fluid dynamics tools.

After the completion of the system concept definition studies for developing high-speed magnetic levitation (maglev) trains conducted under the National Maglev Initiative, the Federal Railroad Administration requested that NASA provide aeronautical expertise.

A conceptual magflight vehicle traveling at 300 miles per hour is considered. It uses a trough-shaped guideway for guidance. A newly developed computational fluid dynamics code is used to solve three-dimensional, Reynolds averaged, thin-layer, Navier-Stokes equations. The first figure shows complex pressure fields on the vehicle surface and the guideway surface. An outcome of this research study is that the shaping of the base region and of the nose region are equally important for lowering the vehicle drag. The base region of the shape investigated contributes to drag the most, because of flow separation and complex streamwise vortex pattern as shown in the second figure, followed by the nose region.

At present, Headquarters Offices of Aeronautics and of Space Access and Technology are in the process of identifying a compelling need for the NASA to get involved with magflight technology. If this need is found, the current study would lead to a comprehensive investigation of magflight aeronautical issues.

Contact: U. Mehta
(415) 604-6744

Headquarters program office: OA

Figure Captions

Fig. 1. The pressure contours on the surfaces of guideway and vehicle.

Fig. 2. Streamsurfaces, eminating from the nose region, manifest large streamwise vortices at the base of the vehicle.

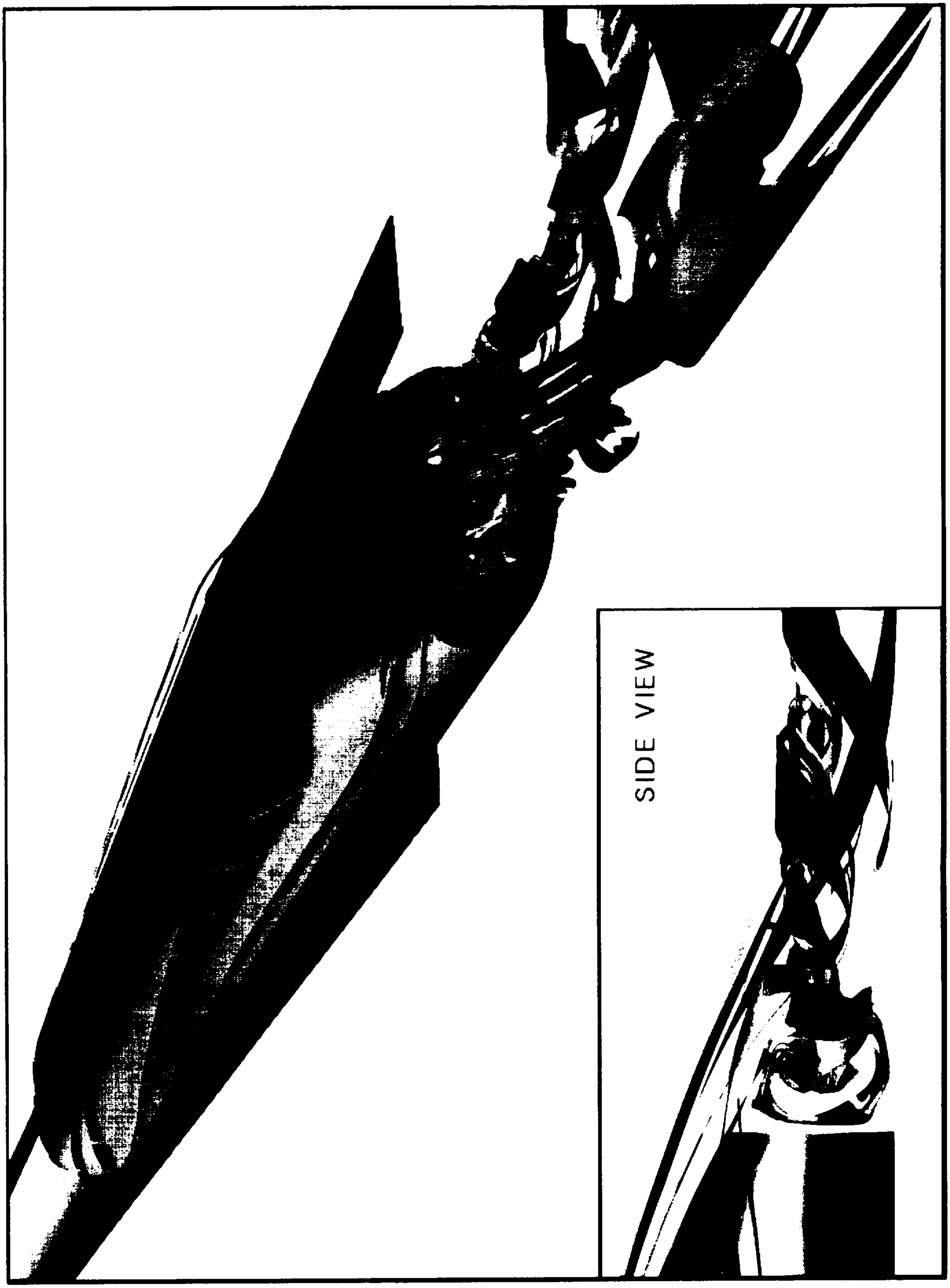
SIDE VIEW

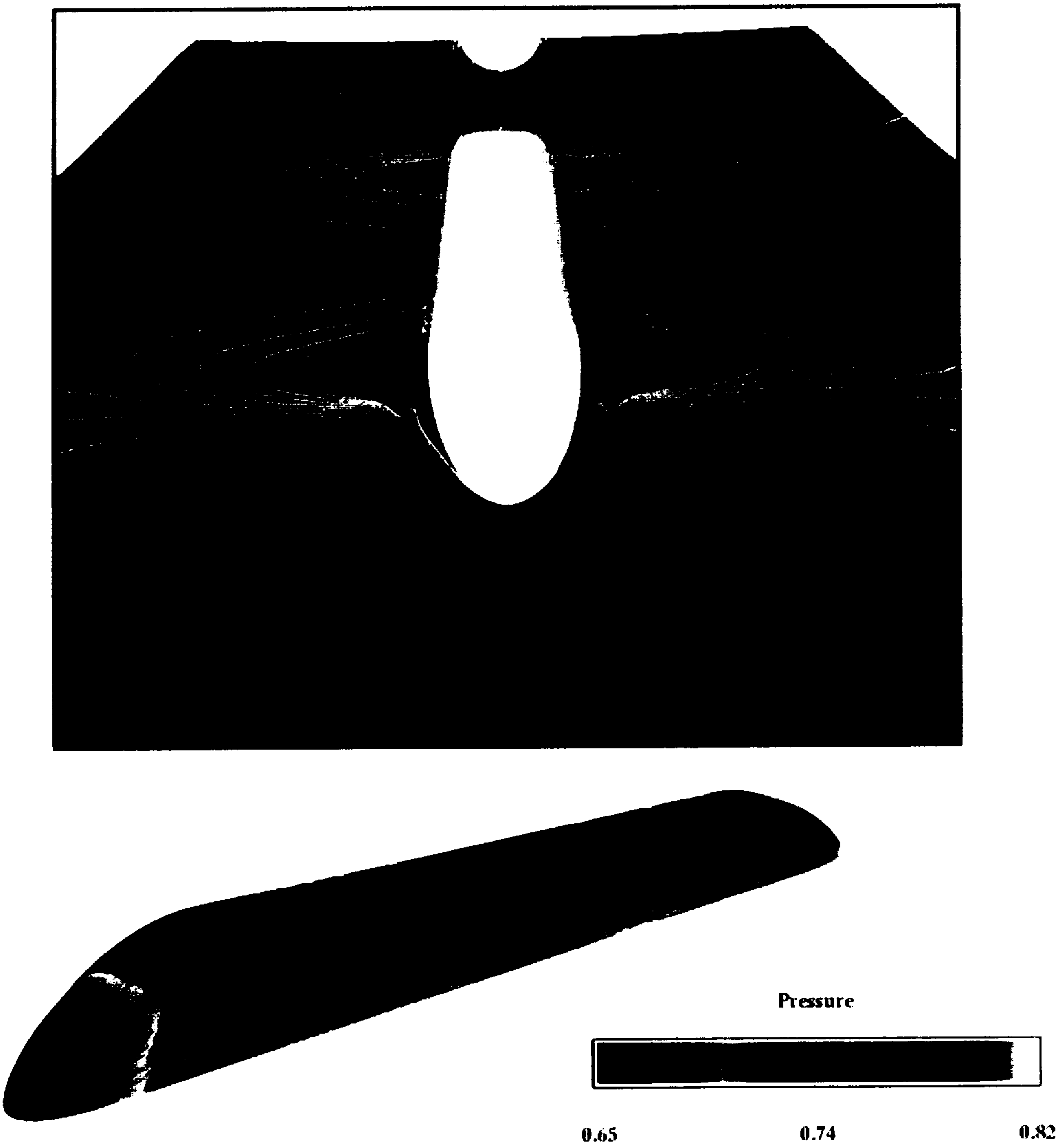
Pressure
0.65
0.74
0.82

Mentoring

The following students were mentored during the past four years. The main purpose of having students work with a mentor is to acquaint them with the type of work being done at Ames and to give them a flavor of working in a research environment under actual working conditions. Initially they were put to work on simple tasks such graphic processing of numerical results. As they become more proficient, they were involved with computer code development and numerical studies of specific problems. The three students involved are listed below as well as the type of work done by each.

1. David Dinh Yeh, high school student,

   September 1990 to June 1991, (one day per week)

   Code development, and graphics.

2. Michael David Baker, undergraduate student at Cal Poly Pomona,

   Summer 1992, summer 1993, March 1994 to September 1994,

   Code development for CNSFV, grid generation for the LFSWT Project, preparation of graphics for the LFSWT Project, and development of higher order accurate finite difference schemes.

3. Kevin K. Okamoto, graduate student at UC Davis,

   Summer 1992, summer 1993, and summer 1994,

   Force and moment code development and grid quality studies.

APPENDIX - A

Virtual Zone Navier-Stokes Computations For Oscillating Control Surfaces

**Klopfer, G. H. and
Obayashi, S.
MCAT, Inc.
Moffett Field
California**

VIRTUAL ZONE NAVIER-STOKES COMPUTATIONS FOR OSCILLATING CONTROL SURFACES

G. H. Klopfer* and S. Obayashi*†
NASA Ames Research Center
Moffett Field, CA 94035-1000

Abstract

A new zoning method called "virtual zones" has been developed for application to an unsteady finite difference Navier-Stokes code. The virtual zoning method simplifies the zoning and gridding of complex configurations for use with patched multi-zone flow codes. An existing interpolation method has been extensively modified to bring the run time for the interpolation procedure down to the same level as for the flow solver. Unsteady Navier-Stokes computations have been performed for transonic flow over a clipped delta wing with an oscillating control surface. The computed unsteady pressure and response characteristics of the control-surface motion compare well with experimental data.

Introduction

Present transport aircraft as well as highly maneuverable fighter aircraft are often subject to unsteady aerodynamics. In this unsteady environment aircraft designers utilize active controls to achieve controllability and safety of the aircraft. Active control can also be used to suppress transonic flutter characteristics of high aspect ratio wings and thus reduce the structural weight to achieve more efficient flight conditions.

In the transonic flow regime active controls have a pronounced effect on the aerodynamic and aeroelastic performance of a wing. This effect can be used to improve the airplane performance by improved design of the active control surfaces. To do this successfully requires accurately predicting the aerodynamic and aeroelastic performance of a wing. Experimental prediction of unsteady aerodynamic and aeroelastic performance is costly, risky and time consuming; numerical simulation of the unsteady Navier-Stokes equations is a much more cost effective alternative for predicting the performance of an active control surface.

The physics of unsteady transonic flow around a control surface has been simulated with small disturbance theory [1,2]. Unsteady Navier-Stokes simulations have been performed in two dimensions [3,4]. A more recent study [5] conducted a three dimensional simulation of the unsteady thin-layer Navier-Stokes equations on the flow field surrounding a wing with a forced oscillating control surface. In that study an unsteady Navier-Stokes code, ENSAERO, was extended to simulate unsteady flows over a rigid wing with an oscillating trailing-edge flap.

The numerical simulation of the unsteady Navier-Stokes equations about complex and realistic aerodynamic configurations requires the use of zonal methods. In this method the overall flow field domain is subdivided into smaller blocks or zones. In each of these zones the flow field is solved independently of the other zones. The boundary data for each zone is provided by the neighboring zones. A major difficulty of the zonal methods applied to oscillating control surfaces has been how to account for the variable exposure of the ends of the control surfaces to the flow field.

In Ref. 5 an algebraic grid generation technique was incorporated into the ENSAERO code. The grid moved at every time step to follow the deflection of the flap. The small unsteady deflections were handled using a sheared single mesh. The large mean deflections were handled using a zonal method [6]. The use of the single sheared grid did not permit the exact simulation of the unsteady flap-wing geometry. A gap had to be introduced between the ends of the flap and wing to allow sufficient space for the moving sheared mesh. The gap compromised the geometry and numerical predictions of the oscillating control surface flow field. The purpose of the present study is to rectify that compromise through the use of a new zoning technique called "virtual" zones.

The virtual zoning method, first implemented in a multizone finite volume code, CNSFV, [7], has been modified for application to the unsteady finite difference code, ENSAERO. The main purpose of these zones is to convert, for example, a solid wall boundary condition into an interface condition. The interface conditions are required for the interzonal communication. In a multi-zonal code the virtual zones are treated like real zones as far as boundary and interface conditions are concerned, however, no flow field computations are done within these zones. Hence, the name "virtual" zone is appropriate.

In addition to the introduction of the virtual zones, it is necessary to speed up the process of determining the interpolation coefficients required for the interzonal communication if the unsteady Navier-Stokes simulation is to be practical.

The present study considers the transonic vortical flow over a clipped delta wing. A view of the wing and the control surface is shown in Fig. 1. Unsteady Navier-Stokes computations for the clean wing were reported in Ref. 8. The forced oscillating control surface computations with the single zone sheared mesh were presented in Ref. 5.

Numerical Method

A brief description of the governing equations, grid and zonal system, and boundary conditions is given in this section. Most of the attention will be focussed on the virtual zoning concept and the unsteady interpolation procedure since these two items were crucial to the successful and practical application of the Navier-Stokes equations to

---

* Senior Research Scientist, MCAT Institute, San Jose, CA 95127

† Senior Member AIAA

Copyright © 1993 by the American Institute of Aeronautics and Astronautics, Inc. No copyright is asserted in the United States under Title 17, U.S. Code. The U.S. Government has a royalty-free license to exercise all rights under the copyright claimed herein for Government purposes. All other rights are reserved by the copyright owner.

oscillating control surfaces.

Governing Equations and Discretization

The governing equations are the Reynolds-averaged thin-layer Navier-Stokes equations. The laminar viscosity is taken from the freestream laminar viscosity and is assumed to be constant for the transonic flow considered in this study. The turbulent viscosity is obtained with the Baldwin-Lomax algebraic eddy viscosity model [9] with the Degani-Schiff modification [10] to properly handle the leading edge separation as well as the control flap vortical flow.

The numerical algorithm, time dependent metrics of the curvilinear coordinate system, and performance characteristics of the ENSAERO code have been described previously and will not be repeated here. The interested reader is referred to Ref. 5.

Control Surface Grid and Zones

The primary focus of the present study is to demonstrate the feasibility of using dynamic zones for the oscillating control surface case rather than minimizing the cpu run time for the case to be presented. Hence the flow domain was split into only three real zones. Each of the zones consists of a C-H topology. The two zonal boundaries were placed at the span stations located at the ends of the control surface. Four additional virtual zones were placed in the two cuts separating the flap and the wing. One pair of the virtual zones remains fixed with the wing and the other pair is fixed with the flap and moves with the flap during the control surface motion. Figure 2 shows the seven zones used in this study.

The C-H grid around a deflected control surface can be obtained in two ways. One is to shear every grid line normal to the control surface with the local deflection. The other is to algebraically regenerate the entire C-H grid with the control surface deflected at every time step. A previous study [5], showed that the computed surface pressures did not show any significant differences between the two methods. Therefore, for this study, the grids around the control flap were regenerated with the simpler shearing method.

Virtual Zone

The zoning capability of the CNSFV code [6] allows the possibility of a single face of a zone to interact with several other zones. The procedure of determining the interpolation coefficients is automatic in that no additional information is required other than identifying the faces that are in contact with each other. To further extend the flexibility of the zoning method for the case of control surface aerodynamics, the idea of "virtual" zones was introduced in Ref. 7.

Virtual zones are zones of zero thickness (for a finite volume formulation) which serve to transfer solid wall (or other) boundary conditions to an interface condition. Thus multiple boundary conditions can be imposed on a block face with the same flexibility as an interface condition. Virtual zones also decouple the process of volume grid zoning from the surface grid patches which define the aerodynamic configuration under study. Surface grid patches are required in order to impose the proper boundary conditions. The volume grid zones should be set up to obtain the proper mesh qualities required for numerical accuracy. Another advantage of the decoupling is that much fewer zones are now needed, thus easing the effort and time required to generate the grids about complex and realistic configurations.

Perhaps the simplest way to explain the virtual zoning concept is through the use of a generic wing/flap configuration represented by two cylinders sliding past each other as shown in Fig. 3. In Fig. 3a(i) the two cylinders are in contact and aligned. A convential zoning scheme has no difficulties for this configuration. In Fig. 3a(iii) the two cylinders are completely separated from each other and again a convential zoning scheme is adequate. However a convential zoning scheme may not be possible at the instance where the two cylinders are in partial contact as in Fig. 3a(ii). The topology of the grids and zones in these three instances is not the same, and thus it is not possible to conveniently use the convential zoning procedure for such dynamic configurations.

On the other hand, as Fig. 3b illustrates, with the virtual zone concept the topology of the grids and zones does need to not change during the movement of the upper cylinder over the lower one. By covering the cut ends of the cylinders with a virtual zone so that the variable solid wall boundary conditions become interface conditions, the upper zone communicates with the lower zone only through the interface condition irrespective of the relative position of the two cylinders. As also shown in the figure, the grid topology of the virtual zones can be, and usually is, different from the topology of the volume grid in contact with the virtual zone. By this simple idea of converting boundary conditions into interface conditions through the use of virtual zones, dynamic configurations which were previously difficult to zone and grid with patched grids become tractable.

The virtual zones also allow the zonal boundaries to cut through the configuration surfaces, which is an important property of control surfaces. The region of the configuration that intersects the zonal face is covered with a virtual zone to convert that region into another interface condition. Once a zone has been defined along with its associated virtual zones, its definition is complete and is not influenced by any of its neighboring zones. In other words, the real zone communicates with the other zones (real or virtual) only through the interface conditions. Thus a particular zone can be altered or substituted with another zone without any need to redefine the interface conditions of the other zones. For example, a zonal grid can be set up for a wing with control flaps with one zone for each (say, undeflected) flap. For the deflected flap case, only the flap zone needs to be replaced with a zone containing a deflected flap. The boundary and interface conditons of all other zones remain unchanged, even though they may now have a solid surface exposed to the flow field, e.g., the edge of the exposed end of the wing and flap.

The original zoning capability of the ENSAERO code was extended by including the above capability of multiple interface conditions on a single block face. Since the code is a finite difference code the zones required an overlap at the boundaries of the zones to allow for the proper interblock communication (i.e., interfacing). In this study a one-cell overlap was chosen. For this kind of zoning the virtual zones of zero thickness used for the finite volume formulation are not appropriate. Instead, the thickness of the virtual zones had to be expanded to include the extent of the overlap of the zones and, thus, the virtual zones for the present formulation are now one cell thick. This formulation results in a slight mismatch of one-half cell thickness between the location of the actual solid wall and the virtual zone boundary. The solid wall boundary condition is applied at the proper location and the slight mismatch has no discernable influence on the overall flow field, especially in the case where the ends of the flaps and wings are treated with the no-slip viscous boundary condition, rather than with the inviscid tangency condition.

An example of the virtual zones required for the present case is shown in Figs. 4-6 for the inboard end of the control surface. The two virtual zones slide through each other with the control surface motion. It can be seen in the figures that different regions of the virtual zones are then exposed to, or in contact with, the real zones surrounding the wing and the flap. The virtual zones transfer the solid wall boundary condition to an interface condition and thus allows for the automatic inclusion of the variable exposure of the ends of the flap and wing to the flow field. The area where the wing and flap virtual zones overlap represents the unexposed portions of the flap and wing. Since the flow field is not updated in the virtual zones by the flow solver, nothing happens in the virtual zone overlap region nor does it influence the rest of the flow field.

Zonal Interface Interpolation

The original interpolation procedure used in CNSFV and ENSAERO is based on a global area search. Even though it is highly vectorized, it still requires 5000 μsec per target point on a Cray YMP on an interface with 2500 points for both the target and base domains. In this paper a target point is the point to be interpolated using the data from the base points. The global area search is, thus, much too slow for a dynamic interpolation procedure where the interpolation coefficients have to be updated at every time step. By replacing the area search with a clipping search procedure based on a polygon clipping algorithm (also called window clipping, Ref. 11), the search time to find the interpolants is reduced by two orders of magnitude. This improvement brought the cpu run time for determining the interpolation coefficients down to the same level as required for the flow solver. In addition to the clipping search, the nested loop (or shell) search, directed hunt, and range limiting search are used to speed up the process and are described below.

The clipping search is based on the well-known polygon clipping algorithm. However, instead of clipping a polygon to fit inside a window, only one point designated the target points is used. The window is formed from the four base points and we are trying to find the four base points that surround the target point. In general the four base points do not form a rectangular window and the "coarse clip" circumscribes the four base points as shown in Fig. 7. The clipping proceeds as follows:

1. Circumscribe the four base points with a rough window.

2. Target point to the right of left boundary? If so, continue with 3. If not, go to next set of base points since target cannot be inside this window.

3. Target point above bottom boundary? If not, go to next set of base points; if so continue with 4.

4. Target point to the left of right boundary? If not, go to next set of base points; if so continue with 5.

5. Target point below top boundary? If not, go to next set of base points; if so target point inside the rough window and the "coarse clip" is successful, continue with 6.

6. Transform the four base points into a unit square aligned with the coordinate axis using a bilinear transformation, as sketched in Fig. 7. Locate the target point in the transformed space and repeat the search procedure 2-5. If this "fine clip" is successful then have located the four base points that surround the target point and can now go to 7.

7. Determine the bilinear interpolation coefficients for this target point and go to 8.

8. Proceed to next target point and go to 1.

The efficiency of the clipping search comes from two factors: the first is that non-candidate base points are rejected as quickly as possible with a minimal amount of operations performed. Secondly, the bilinear transformation is done only if the target point is inside the rough window. The bilinear transformation is relatively expensive to compute compared to setting up a rough window which requires only a few minmax function operations on the four base points, especially when the degenerate cases of the four base points collapsing into triangles must be considered.

In the best-case scenario where the first guess of the base points is the correct one, the Cray YMP cpu time per target point is 35 μsec for the above clipping search procedure. This includes the coarse clip, bilinear transformation, fine clip, and determining the interpolation coefficients. The worst case is when the target points are not within the domain of the base points. In this case assuming grids with 2500 points for both the target and base grids, about 600 μsec are required. The reason that the times are not larger is that only the coarse clip procedure needs to be executed. In spite of the slow times, the worst case times are about 10 times faster than the vectorized global area search procedure.

To obtain the times of the best case, it is clearly necessary to obtain the best guess possible for the base points so that only a small neighborhood needs to searched. For the steady-state problem a good starting guess for a new target point is the base points found from the previous target point. For unsteady cases, where the target grid is moving relative to the base grid, a good strategy for the starting base points is to use the base points found for this target point at the previous time step. For highly clustered meshes where a target point can move across several dozen base points during a time step, a better approach is to use the one for the steady state case. In this paper, however, we use the previous time step guess. With the starting guess for the base points, two procedures called the "shell search" and "directed hunt" are used with variable success. A third method called "range limiter" is developed to reduce the time required for the worst case or near worst case situation which happens quite often for the oscillating control surface configuration. All three methods are described below in further detail.

The shell search uses the clip search as the basic engine. The shell search refers to the sequence in which the four base points are tested against the clip search. The innermost shell depicted as $n = 1$ in Fig. 8 is the starting guess for the base points. If the clip test is unsuccessful, then the search proceeds to the next shell and loops around the inner shell until the clip test succeeds or until all the $8(n-1)$ sets of base points are tested. If again unsuccessful, the search proceeds to the next shell. The number of tests increases as $(2n-1)^2$ where n is the shell number. If the shell intersects a boundary of the base grid, then the shell is truncated at that boundary. The maximum number of shells searched is equal to the maximum dimension of the base grid. If the guessed starting set of base point is not good, then the shell search is not much better than searching the entire base grid with the clip search. However, if the starting guess is good and the target points have not moved across too many base points, then the shell search is successful within 2 or 3 shells, requiring at most 9 or 25 clip searches. Tests with various cases have shown that it is more efficient to stop after the second shell and do the range limiter (explained below) before proceeding with the next shell. Typical test cases show that the shell hunt cpu times vary from 35 μsec to 150 μsec per target point.

A potentially more efficient procedure than the shell search is the directed hunt. In this method, the best guess for the four base points and the target point is transformed into the unit square window. Let the transformed coordinates of the target point be (k_t, l_t) as shown in Fig. 9. If the coordinates are positive and less than one, the four base points have been found; if not, the next guess for the reference base point coordinates is given by

$$k_n = k_o + int(k_t - 1)$$

$$l_n = l_o + int(l_t - 1)$$

where k_o, l_o are the indices of the reference point of the four base points, as shown in Fig. 9. Typically, the directed hunt should find the base points with only 2 to 3 steps. However the bilinear transformation often breaks down because of degenerate base points, or the direction takes the search to the outside of the base domain boundaries (e.g., in crossing the wake boundary of a C-mesh). In the latter case one has to step along the boundary until the directed hunt can be continued. For these reasons the directed hunt has not been reliable and efficient enough for the oscillating control surface problem. Since the directed hunt has the potential of being 2 to 3 times faster than the shell search, especially if the first guess is poor, work is continuing on developing a reliable directed hunt procedure.

The cost of computing the searching procedure increases as the number of base points increases. What is needed is an efficient procedure to reduce the number of base points over which to search, or to eliminate them entirely if the target point is not within the domain of the base points as in the worst-case scenario mentioned above. The "range limiter" was developed for this purpose. As with the shell search the basic engine is again the clip test. The range limiter can be described with the help of Fig. 10 as follows:

1. Circumscribe the domain of the base points with the window shown in Fig. 10a.

2. Apply the clip test to the target point; if target is inside window, continue with 3; if not, target point cannot be interpolated with the given base points. Go on to next target point.

3. Subdivide the base domain in half and choose the subdivision which produces the smallest overlap area as shown in Fig. 10b and 10c. If overlap areas are equal, choose the partition which operates on the larger of the two dimensions; if the dimensions are the same, use the first of the two subdivisions.

4. Apply the clip test to the target point with both of the subdomains. If the target point is in one but not the other of the subdomains, then define the domain of base points to be the domain in which the target point lies and continue with 1. If the target point lies in both of the subdomains (i.e., it lies in the overlap area) then cut off the two subdomains at the ends opposite the overlap region and redefine the domain to be the central portion of the base point domain and continue with 1. The clip test is applied to the cutoff portions to make sure that the trimmed portions do not contain the target point.

5. The subdivision along any one direction stops if the dimension in that direction is less than 5, since at that point the shell search is more efficient.

Although the range limiter appears cumbersome, it is quite useful and efficient especially if the domain of base points is larger than the domain of target points, and it very quickly excises the portions of the base domain which are not close to the target point. Once the base domain has been trimmed, the shell search or directed hunt is used for the local search. Another way of trimming the base domain is to place search limits on the base domain beyond which the search will not be conducted. This last method is effective only if the search limits are known a priori, as for the present case of the oscillating control surface.

It is of interest to compare the present method with the so-called Domain Connectivity Function method of Ref. 12. The present method is just slightly faster than the dynamic mode of the DCF method. Compared to the static mode of the DCF method, where the inverse mapping needs to be determined, the present method is substantially faster (approx. 10 times). For the oscillating control surface problem, the DCF method would have to be run in the static mode and thus is too slow to be pratical.

Results

The test case considered in the present study is a clipped delta wing with an oscillating trailing edge control surface [13]. The wing planform is shown in Fig. 1. The wing has a leading edge sweep angle of 50.4 deg and a 6% thick circular arc airfoil section. At $M_\infty = 0.9$ and $\alpha = 3$ deg, both a leading edge vortex and a shock wave are present on the upper surface of the wing. The C-H grids of the three real zones consist of $151 \times 13 \times 34$, $151 \times 15 \times 34$, and $151 \times 20 \times 34$ points from inboard to outboard as shown in Fig. 2. Since the experiment was conducted using a Freon test medium, the ratio of specific heats, γ, is set to 1.135 in the present computations. As stated before, the modified Baldwin-Lomax model is used to account for the leading edge and control surface vortices. However, the boundaries normal to the edges of the control surface and the wing cuts are treated with the solid wall tangency condition. Steady state and rigid pitching calculations of this wing were reported in Ref. 8.

Figure 11 shows the unsteady pressures coefficients with the control surface oscillating at a frequency of 8 Hz and an amplitude of 6.65 deg at $M_\infty = 0.9, \alpha = 3$ deg and $Re_c = 17 \times 10^6$ based on the root chord. The results are shown as the amplitude and phase angle of the upper surface pressure coefficients at the three span stations as indicated on the figure. In general, the agreement with the experimental results is good. Because the accuracy of experiment has its own limitations, the virtual zone results are also compared with the single grid results of Ref. 5. There is quite a discrepancy between the virtual zone results and the single grid results (the $151 \times 44 \times 34$ grid), especially in the amplitudes at the center of the control surface. This discrepancy is most likely due to the gap that was introduced between the flap and wing in the single grid case to accommodate the shearing grid. If the gap is reduced by increasing the spanwise resolution of the wing and control surface, the computational results of the refined single grid case ($151 \times 87 \times 34$) approach those of the virtual zone. This particular example demonstrates the importance of simulating the geometry of the control surface/wing configuration accurately.

Figure 12 shows the upper surface pressures as well as the instantaneous streamline traces emanating from the leading edge of the wing (black traces), the lower edges of the wing at the control surface cut (blue traces), and the upper edges of the control flaps (red traces). The interaction between the leading edge vortex and the outboard edge of the control surface vortices during the flap motion cycle is well demonstrated. Although not apparent in this figure, the computations also show that the flow on the leading side (defined as upper surface during the upstroke motion and lower surface during the downstroke motion) of the inboard section of the control surface is separated.

Figure 13 shows the velocity vectors at the inboard edge of the control surface as the flap is in the upstroke mode at the instant of zero deflection. The flow field is shown in much more detail at the trailing edge of the control surface. The detailed views show the velocities of the trailing edge of the control surface. As can be seen, these velocities are small, even when compared to the flow field in the inner regions of the boundary layer. Figure 14 shows the surface streamlines on the inboard edge and upper surface of the control surface. The particle traces are computed at each instant of time by freezing the flow field during the tracing procedure. The temporal changes in the surface particle traces as the control surface oscillation cycle is executed are quite apparent, both on the upper surface and the edge of the control surface as it is exposed and covered by the wing edge. The first view of Figure 14 shows that the flow is separated near the inboard trailing edge corner of the control surface. Preliminary studies with a viscous (albeit laminar) treatment of the control surface edges and wing cuts indicate that the separated region on the upper surface of the flap increases.

Conclusions

An unsteady interface algorithm based on the idea of virtual zones has been developed for a finite difference code, ENSAERO. The new "virtual" zoning technique simplifies the zoning of complex geometries, such as control surfaces, and makes possible the use of standard multizonal codes for complex configurations. A fast search routine based on a window clipping algorithm has also been developed and is fast enough for the interpolation coefficients to be recomputed at every time step. For the example presented in this study, the computational effort required for the interpolation coefficients is less than that for the flow solver.

Both of the above developments have made practical a complete unsteady Navier-Stokes simulation of a forced oscillating control surface on a clipped delta wing in the transonic flow regime. The method has been validated against experimental data as well as numerical simulations based on a shearing single-zone grid. The numerical result confirms that the accurate representation of geometry by "virtual zones" is superior to the single zone computations of the same grid size.

Acknowledgements

The first author's work was supported by NASA Grant NCC 2-616 and the second author's by NCC 2-605.

References

1. Ballhaus, W., Goorjian, P. M., and Yoshihara, H.; "Unsteady Force and Moment Alleviation in Transonic Flow," AGARD Conference Proceeding No. 227, May 1981.

2. Guruswamy, G. P. and Tu, E. L.; "Transonic Aeroelasticity of Fighter Wings with Active Control Surface," Journal of Aircraft, Vol. 26, No. 7, July 1989, pp. 682-684.

3. Steger, J. L. and Bailey, H. E.; "Calculation of Transonic Aileron Buzz," AIAA Journal, Vol. 18, March 1980, pp. 249-255.

4. Horiuti, K., Chyu, W. J., and Buell, D. A.; "Unsteady Transonic Flow Computation for an Airfoil with an Oscillating Flap," AIAA Paper 84-1562, June 1984.

5. Obayashi, S. and Guruswamy, G.; "Navier-Stokes Computations for Oscillating Control Surfaces," AIAA Paper No. 92-4431, August 1992.

6. Klopfer, G. H. and Molvik, G. A.; "Conservative Multizonal Interface Algorithm for the 3-D Navier-Stokes Equations," AIAA Paper No. 91-1601CP, June 1991.

7. Chaussee, D. S. and Klopfer, G. H.; "The Numerical Study of 3-D Flow Past Control Surfaces," AIAA Paper No. 92-4650, August 1992.

8. Obayashi, S. and Guruswamy, G.; "Unsteady Shock-Vortex Interaction on a Flexible Delta Wing," Journal of Aircraft, Vol. 29, No. 5, Sept-Oct 1992, pp. 790-798.

9. Baldwin, B. S. and Lomax, H.; "Thin-Layer Approximation and Algebraic Model for Separated Turbulent Flows," AIAA Paper 78-257, January 1978.

10. Degani, D. and Schiff, L. B.; "Computations of Turbulent Supersonic Flows Around Pointed Bodies Having Crossflow Separation," Journal of Computational Physics, Vol. 66, No. 1, September 1986, pp. 173-196.

11. Pavlidis, T.; **Algorithms for Graphics and Image Processing**, Computer Science Press, Inc., MD, 1982.

12. Meakin, R. L.; "A New Method For Establishing Inter-Grid Communication Among Systems of Overset Grids," AIAA Paper No. 91-1586CP, June 1991.

13. Hess, R. W., Cazier, F. W., Jr., and Wynne, E. C.; "Steady and Unsteady Transonic Pressure Measurements on a Clipped Delta Wing for Pitching and Control-Surface Oscillations," NASA TP-2594, Oct. 1986.

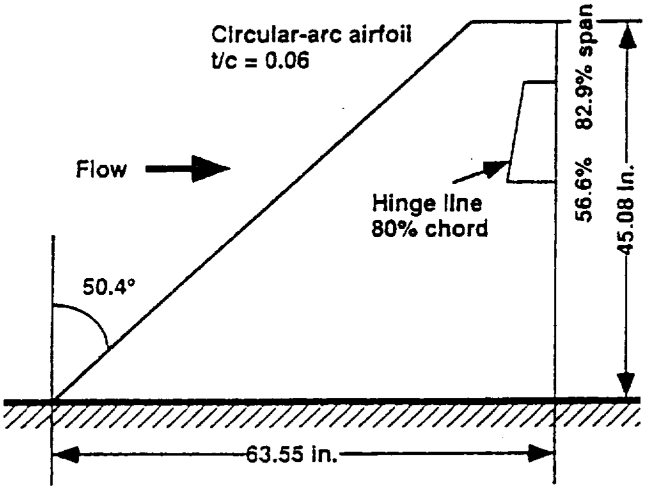
Circular-arc airfoil
t/c = 0.06
Flow
Hinge line
80% chord
50.4°
56.6%
82.9% span
45.08 in.
63.55 in.

Fig. 1. Planform of clipped delta wing with trailing edge flap.

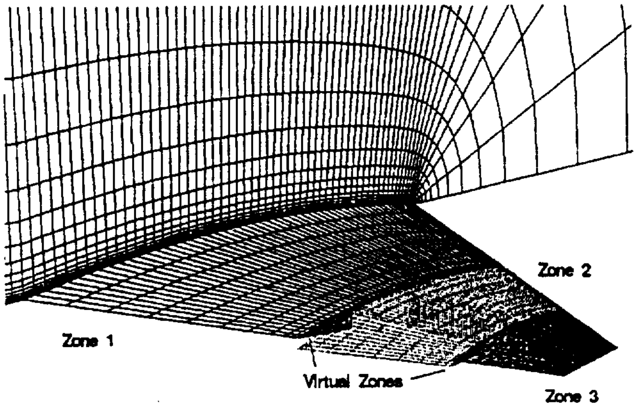
Zone 1
Zone 2
Zone 3
Virtual Zones

Fig. 2. Surface grids and zonal boundaries of wing/flap configuration.

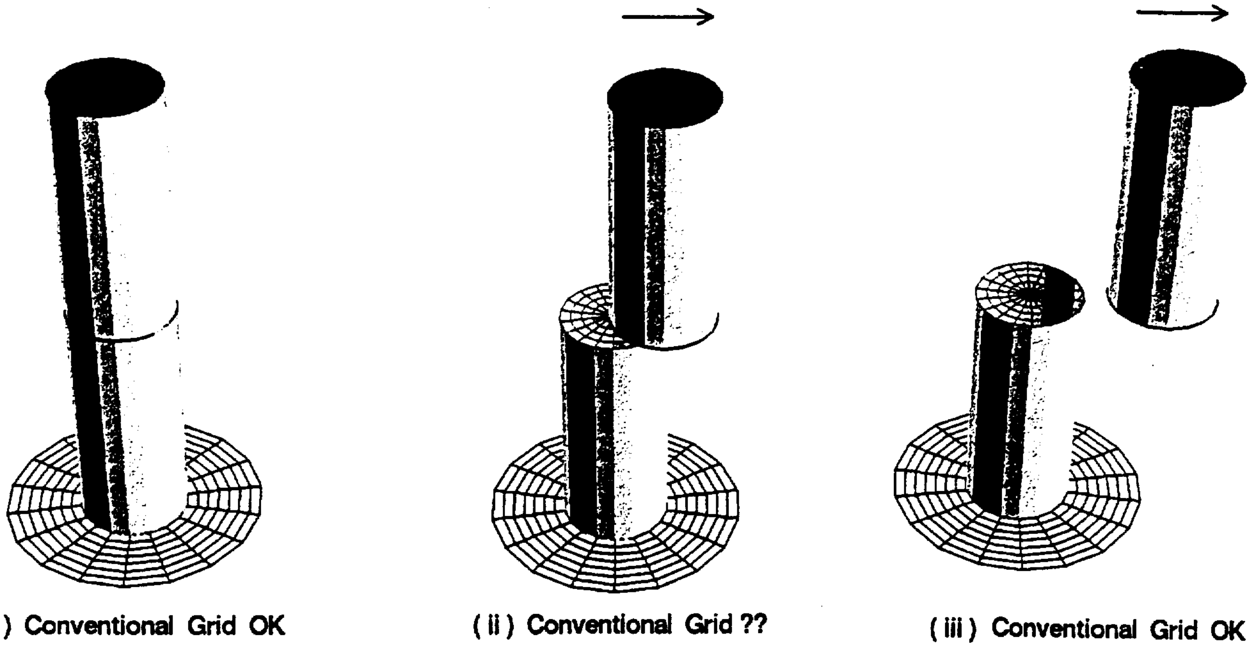
(i) Conventional Grid OK
(ii) Conventional Grid ??
(iii) Conventional Grid OK

Fig. 3a. Generic wing/flap configuration with conventional zones. The top cylinder is sliding over the face of the bottom cylinder.

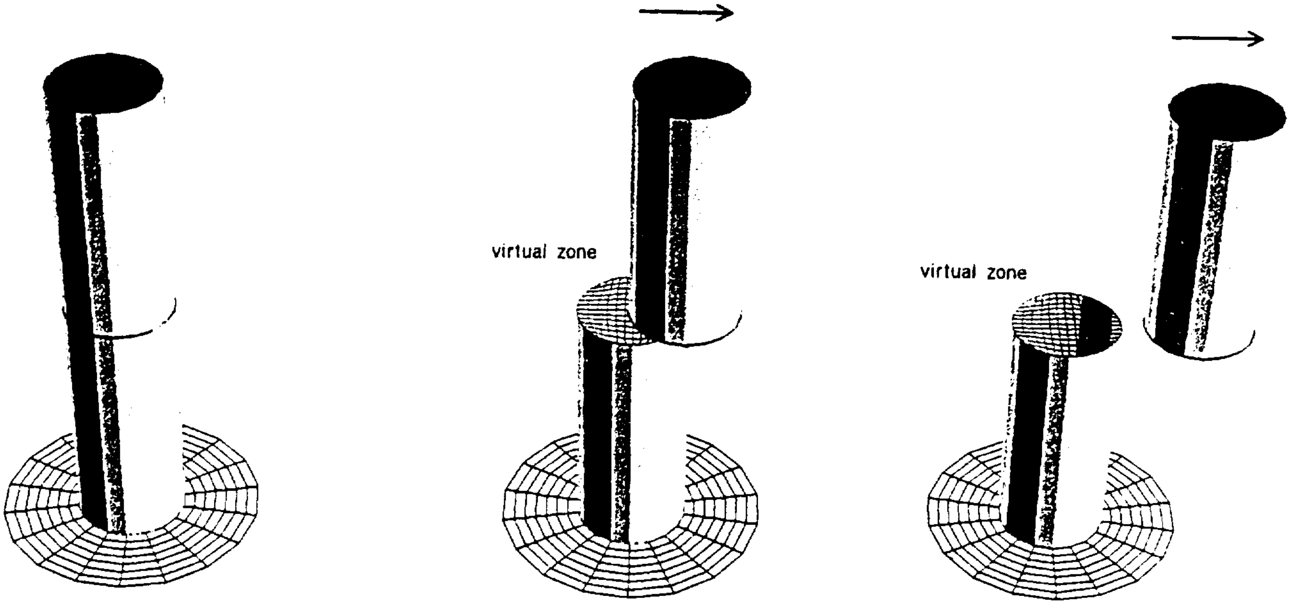

(i) (ii) (iii)

Fig. 3b. Generic wing/flap configuration demonstrating the virtual zone concept. The top cylinder is sliding over the face of the bottom cylinder.

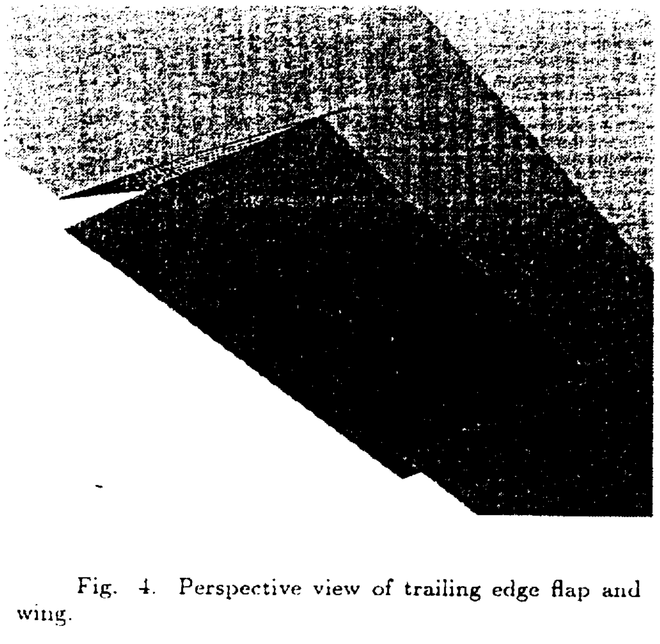

Fig. 4. Perspective view of trailing edge flap and wing.

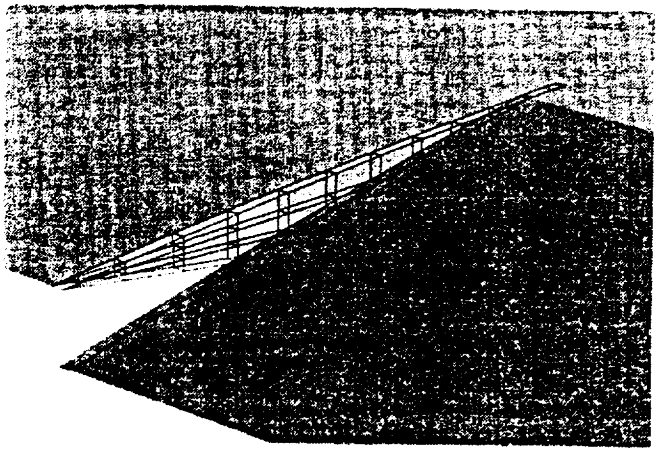

Fig. 5. Perspective view of trailing edge flap and wing with the inboard wing and flap virtual zones.

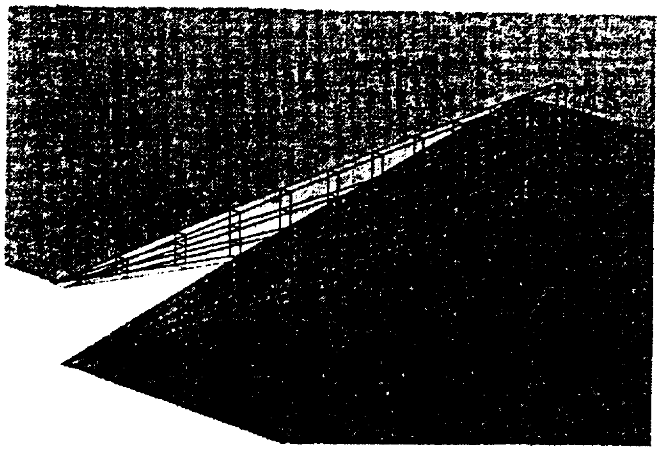

Fig. 6. Perspective phantom view of trailing edge flap and wing with the inboard wing and flap virtual zones.

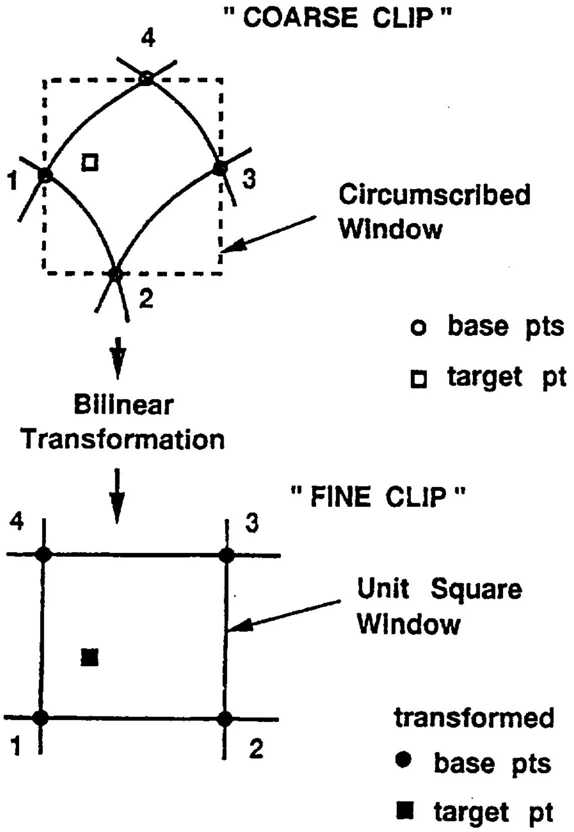
" COARSE CLIP "
4
1
3
2
Circumscribed Window
o base pts
□ target pt
Bilinear Transformation
" FINE CLIP "
4
3
1
2
Unit Square Window
transformed
● base pts
■ target pt

Fig. 7. Clip search procedure; Coarse clip, bilinear transformation and fine clip test.

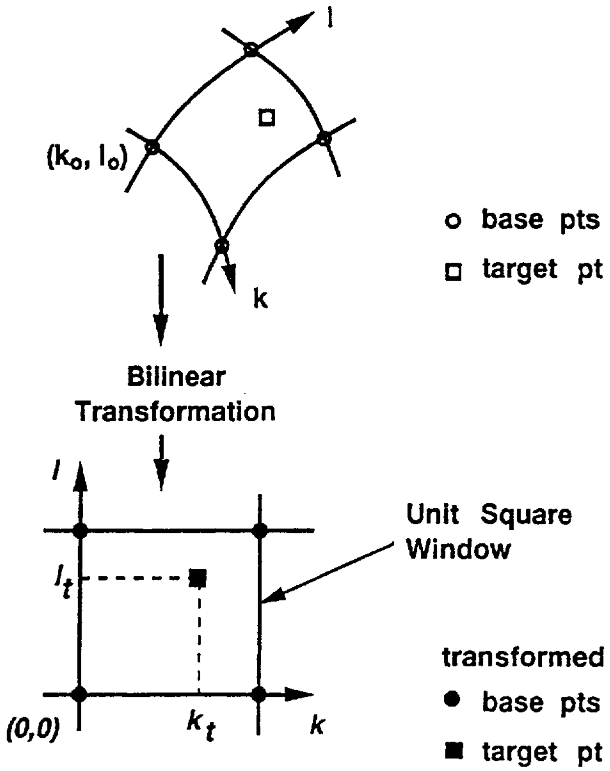
l
(k₀, l₀)
k
o base pts
□ target pt
Bilinear Transformation
l
l_t
(0,0)
k_t
k
Unit Square Window
transformed
● base pts
■ target pt

Fig. 9. The directed hunt procedure.

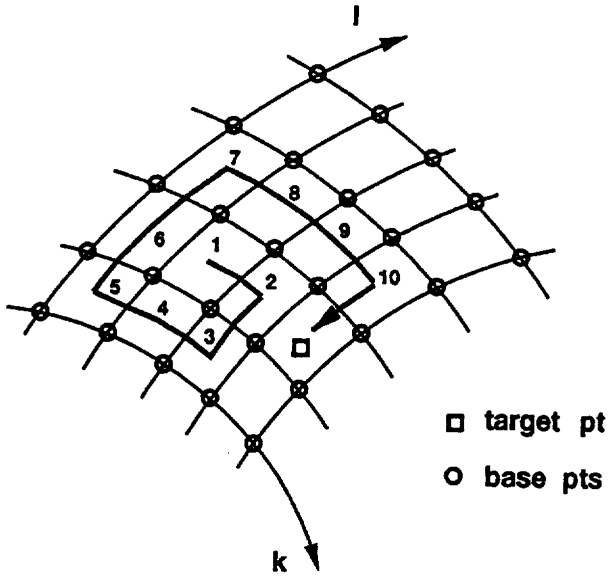
l
7
8
6
1
9
5
4
2
10
3
□ target pt
O base pts
k

Fig. 8. The sequence of steps required for the shell search procedure.

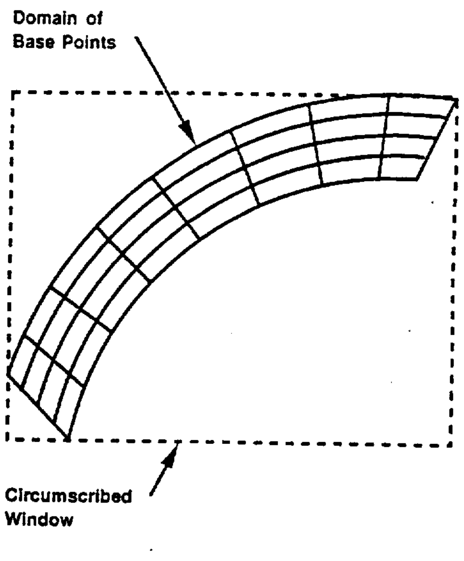
Domain of Base Points
Circumscribed Window

(a)

Fig. 10. The range limiter procedure.

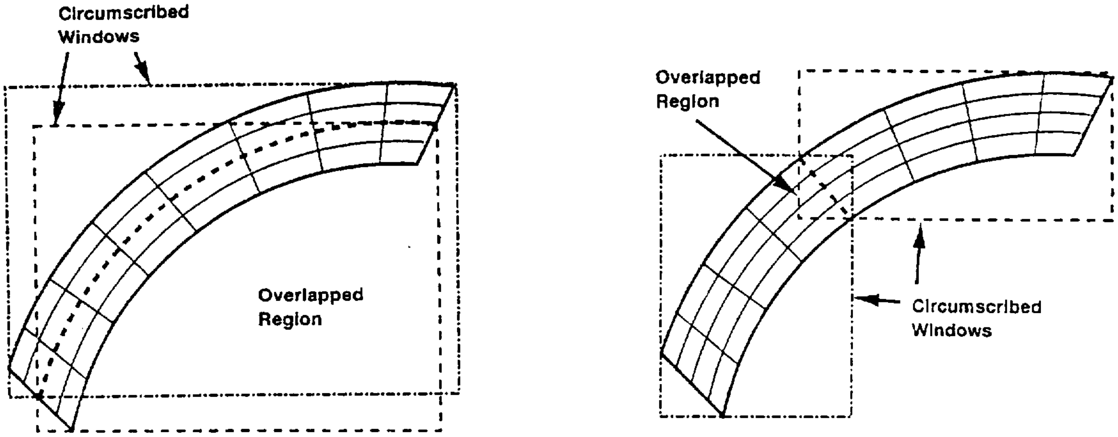
Circumscribed Windows
Overlapped Region
Overlapped Region
Circumscribed Windows

(b) First Partition

(c) Second Partition

Fig. 10. The range limiter procedure.

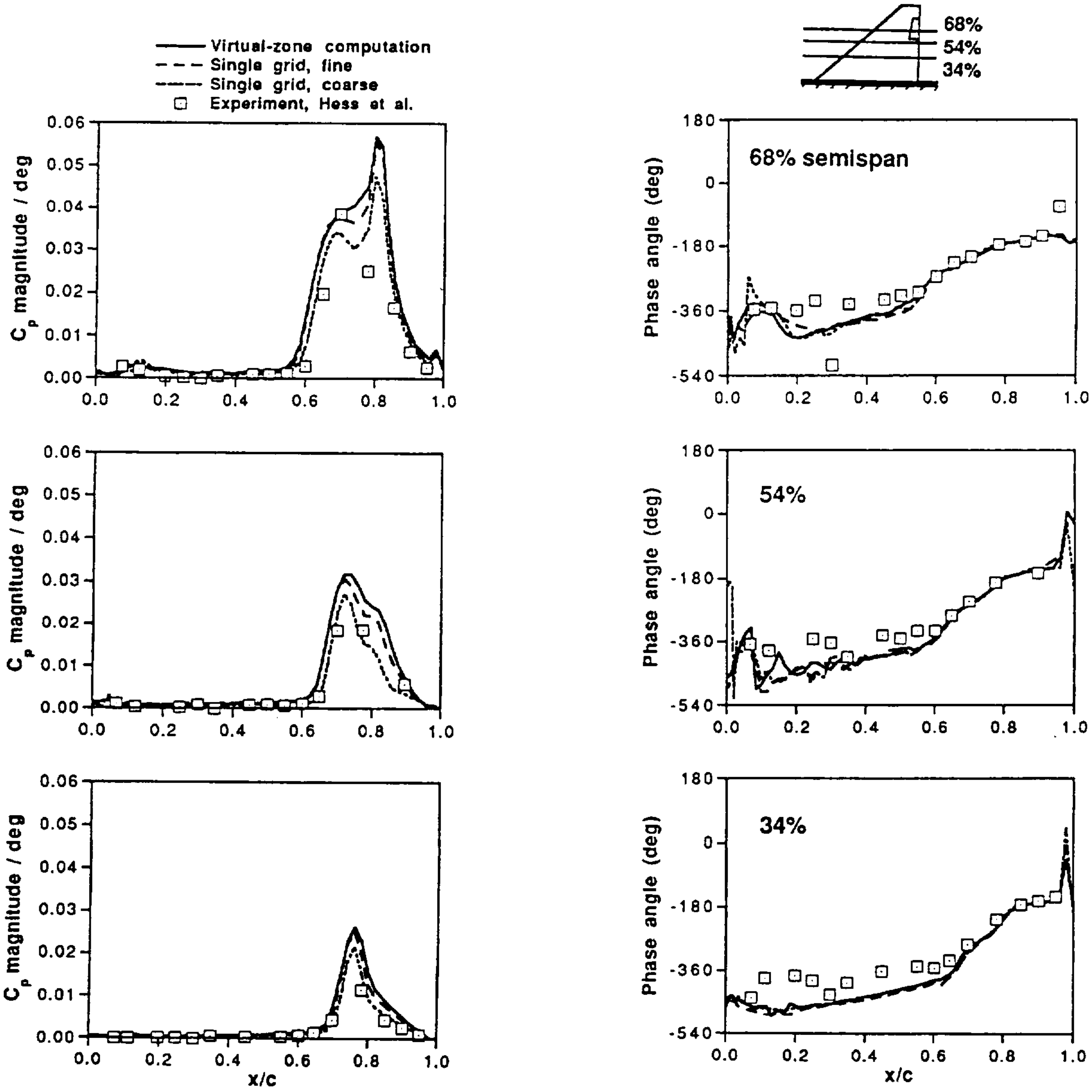

Fig. 11. Comparison of unsteady pressure coefficients between experiment (Ref. 13) and computations using virtual zones and single grids.

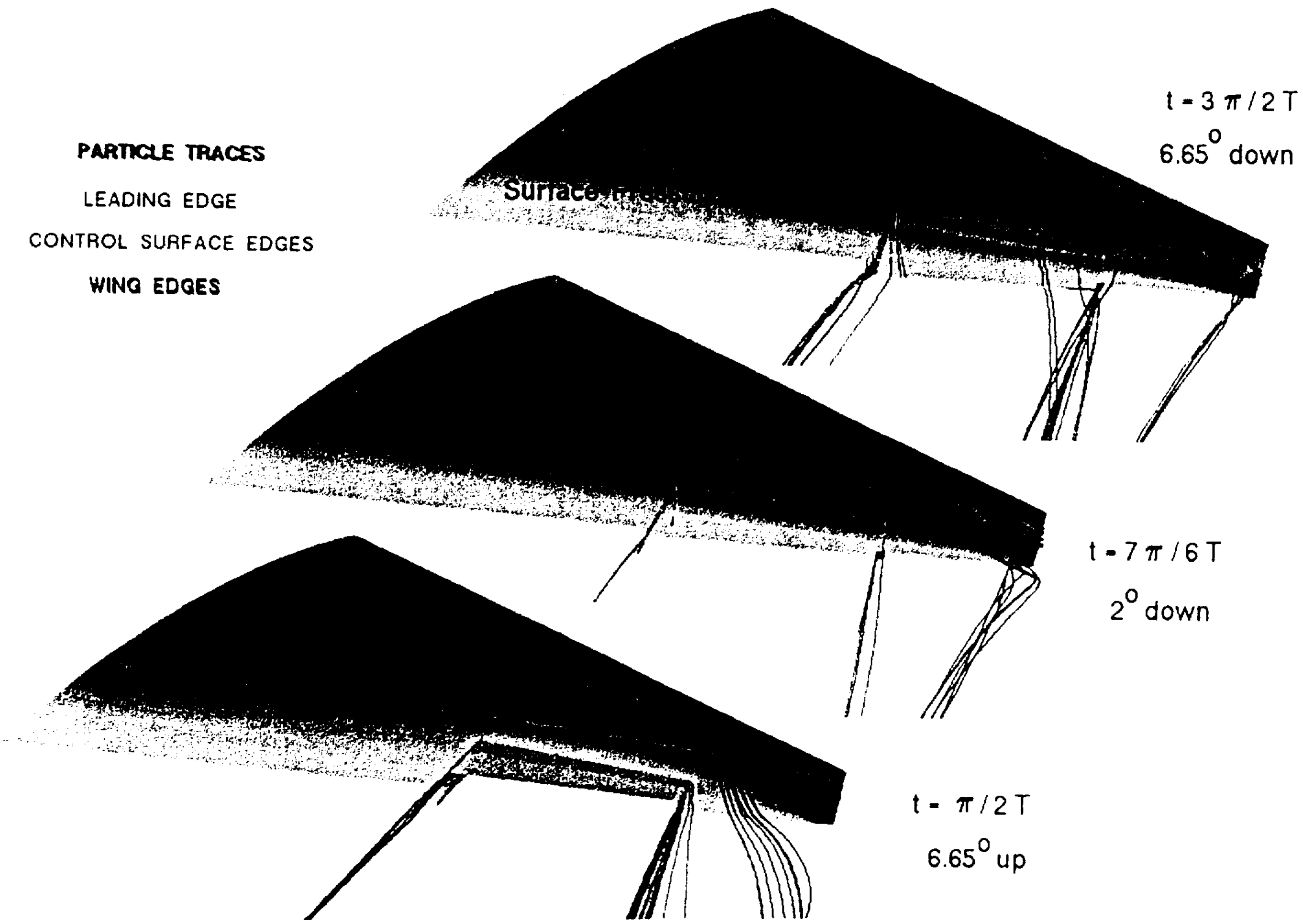
PARTICLE TRACES
LEADING EDGE
CONTROL SURFACE EDGES
WING EDGES
t - 3 π / 2 T
6.65° down
t - 7 π / 6 T
2° down
t - π / 2 T
6.65° up

Fig. 12. Upper surface pressures and instantaneous streamlines emanating from the leading edge and the edges of the control surface.

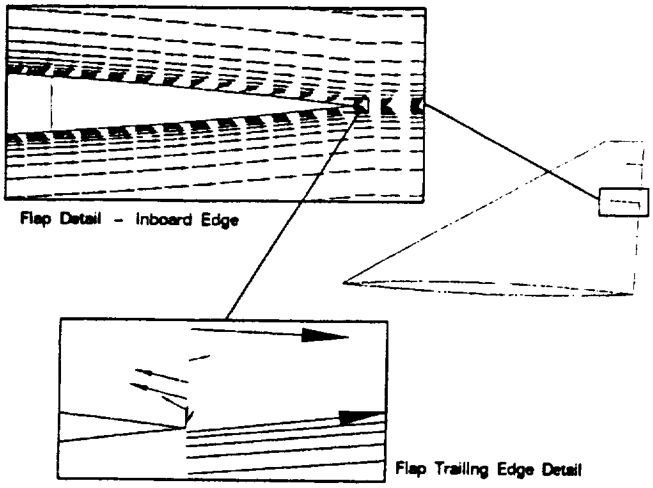
Flap Detail - Inboard Edge
Flap Trailing Edge Detail

Fig. 13. Velocity vector plots near the inboard edge of the control surface at the instant of zero deflection and maximum flap velocity.

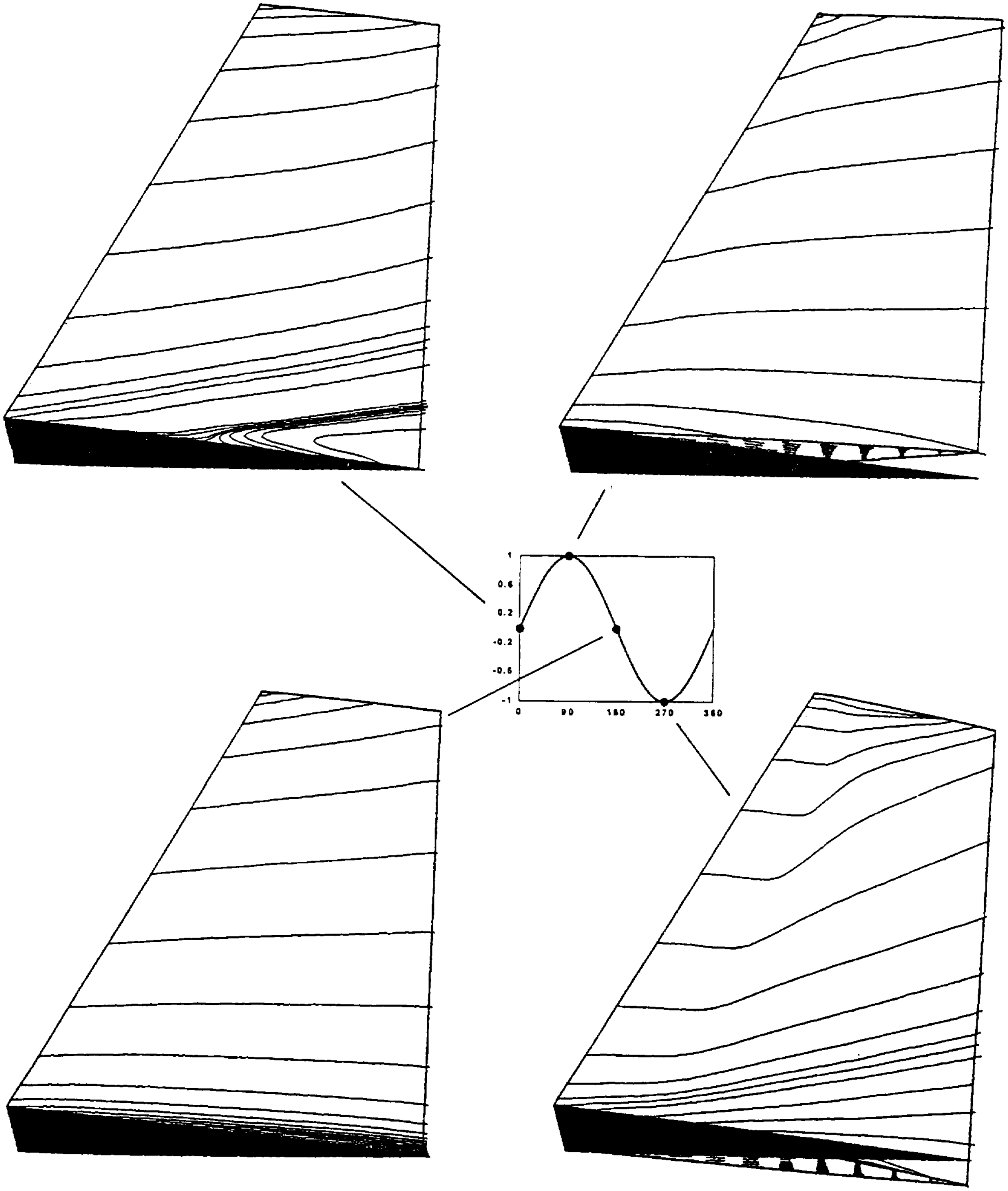
1
0.6
0.2
-0.2
-0.6
-1
0
90
180
270
360

Fig. 14. Surface particles traces on the upper surface and inboard edge of the control surface at four instances of the control surface cycle.

APPENDIX - B

AIAA-94-2356

N[illegible]

A Modified LU-SGS Scheme for High Reynolds' Number Navier-Stokes Flows

Klopfer, G. H. and Kontinos, D. A.
MCAT, Inc.
Moffet Field
California

A MODIFIED LU-SGS SCHEME FOR HIGH REYNOLDS' NUMBER NAVIER-STOKES FLOWS

G.H. Klopfer
Senior Research Scientist
MCAT Institute, Moffett Field, CA 94035
and
D.A. Kontinos
Graduate Research Assistant
N. C. State University

Abstract

A modified LU-SGS scheme is developed which does not suffer reduced convergence rates with increasing Reynolds numbers. The standard and modified version of the LU-SGs are derived and the improved performance of the modified scheme is demonstrated with several flat plate compressible boundary layer flows, hypersonic compression ramp, and in the full paper transonic flow about an ONERA M6 wing and a supersonic flow about a generic HSCT configuration or an incompressible flow about a submarine.

Introduction

In recent years the lower-upper symmetric Gauss-Seidel (LU-SGS) scheme has become the flow solver of choice for solving the Euler and Navier-Stokes equations because of its robustness and fast convergence rates. The scheme is fully implicit and in the scalar form, the operation count per time step and grid point rivals that of explicit schemes. The scheme performs well for a large variety of flows, ranging from subsonic to hypersonic flows with non-equilibrium gases. While the convergence rates are fairly good for transonic flows at moderate Reynolds' numbers, the convergence slows down as the Reynolds numbers increase. When the Reynolds' numbers approach those typical for flows around high speed civil transport and submarines ($R_e \geq 10^8$) the scheme barely convergences and often is caught in a limit cycle. For this reason the scheme has not been widely used in production Navier-Stokes codes.

The cause of the problem is due to the approximation used to diagonalize the Jacobian matrices. While the approximation allows for scalar matrix inversion, the diagonalization is rather poor and thus slows down convergence with increasing Reynolds' numbers. A better approximation is developed which still allows for the scalar matrix inversion but demonstrates a much better convergence rate with increasing Reynolds' number. The operation count of the modified scheme is only slightly more than the original scheme.

In this study we investigate an alternative formulation of the LU-SGS algorithm with the hope of keeping the low operation count of the original scheme and improving the convergence rates at high Reynolds number flows. In the following sections the original LU-SGS scheme is derived, the behavior of the scheme under various conditions demonstrated, and possible causes for that behavior identified. Once the cause for poor performance has been identified, an alternative formulation will be presented and the improved performance of the modified scheme will be illustrated with a series of flat plate compressible boundary layer flow with increasing Reynolds numbers. For the complete paper the modified scheme will be exercised for a supersonic flow about a generic HSCT configuration or an incompressible flow about a submarine for which the standard LU-SGS scheme was unable to converge at all and for a transonic flow about an ONERA M6 wing.

Navier-Stokes Equations

The three-dimensional thin-layer Navier-Stokes equations in strong conservation law form in curvilinear coordinates are

$$\partial_\tau \hat{V} Q + \partial_\xi F + \partial_\eta G + \partial_\zeta H$$

$$= Re^{-1}(\partial_\xi F_v + \partial_\eta G_v + \partial_\zeta H_v) \tag{1}$$

where

$$Q = \begin{pmatrix} \rho \\ \rho u \\ \rho v \\ \rho w \\ e \end{pmatrix}, F = \begin{pmatrix} \rho U \\ \rho u U + \xi_x \hat{V} p \\ \rho v U + \xi_y \hat{V} p \\ \rho w U + \xi_z \hat{V} p \\ (e+p)U - \xi_t \hat{V} p \end{pmatrix},$$

$$G = \begin{pmatrix} \rho V \\ \rho u V + \eta_x \hat{V} p \\ \rho v V + \eta_y \hat{V} p \\ \rho w V + \eta_z \hat{V} p \\ (e+p)V - \eta_t \hat{V} p \end{pmatrix}, H = \begin{pmatrix} \rho W \\ \rho u W + \zeta_x \hat{V} p \\ \rho v W + \zeta_y \hat{V} p \\ \rho w W + \zeta_z \hat{V} p \\ (e+p)W - \zeta_t \hat{V} p \end{pmatrix} \tag{2}$$

The contravariant velocity components are defined as

$$\begin{aligned} U &= \hat{V}(\xi_t + \xi_x u + \xi_y v + \xi_z w), \\ V &= \hat{V}(\eta_t + \eta_x u + \eta_y v + \eta_z w), \\ W &= \hat{V}(\zeta_t + \zeta_x u + \zeta_y v + \zeta_z w) \end{aligned} \tag{3}$$

and the viscous fluxes are given by

$$F_v = \mu \hat{V} \begin{pmatrix} 0 \\ m_1 u_\xi + m_2 \xi_x \\ m_1 v_\xi + m_2 \xi_y \\ m_1 w_\xi + m_2 \xi_z \\ m_1 m_{0_\xi} + m_2(\xi_x u + \xi_y v + \xi_z w) \end{pmatrix},$$

$$G_v = \mu \hat{V} \begin{pmatrix} 0 \\ m_3 u_\eta + m_4 \eta_x \\ m_3 v_\eta + m_4 \eta_y \\ m_3 w_\eta + m_4 \eta_z \\ m_3 m_{0_\eta} + m_4(\eta_x u + \eta_y v + \eta_z w) \end{pmatrix},$$

$$H_v = \mu \hat{V} \begin{pmatrix} 0 \\ m_5 u_\zeta + m_6 \zeta_x \\ m_5 v_\zeta + m_6 \zeta_y \\ m_5 w_\zeta + m_6 \zeta_z \\ m_5 m_{0_\zeta} + m_6(\zeta_x u + \zeta_y v + \zeta_z w) \end{pmatrix} \tag{4}$$

with

$$\begin{aligned} m_0 &= (u^2 + v^2 + w^2)/2 + (Pr(\gamma - 1))^{-1}(a^2), \\ m_1 &= \xi_x^2 + \xi_y^2 + \xi_z^2, \\ m_2 &= (\xi_x u_\xi + \xi_y v_\xi + \xi_z w_\xi)/3, \\ m_3 &= \eta_x^2 + \eta_y^2 + \eta_z^2, \\ m_4 &= (\eta_x u_\eta + \eta_y v_\eta + \eta_z w_\eta)/3, \\ m_5 &= \zeta_x^2 + \zeta_y^2 + \zeta_z^2, \\ m_6 &= (\zeta_x u_\zeta + \zeta_y v_\zeta + \zeta_z w_\zeta)/3 \end{aligned} \tag{5}$$

The pressure is given by the equation of state

$$p = (\gamma - 1)(e - \rho(u^2 + v^2 + w^2)/2) \tag{6}$$

where γ is the ratio of specific heats. The sound speed is denoted by a. The nondimensional parameters are the Reynolds number Re and the Prandtl number Pr. The coefficient of viscosity μ and thermal conductivity k are decomposed into laminar and turbulent contributions as follows:

$$\mu = \mu_l + \mu_t$$

$$\frac{k}{Pr} = \frac{\mu}{Pr} = \left(\frac{\mu_l}{Pr_l} + \frac{\mu_t}{Pr_t}\right)$$

where Pr_l and Pr_t are the laminar and turbulent Prandtl numbers and $k = \mu$ with the nondimensionalization used in this paper. The standard Baldwin-Lomax turbulent eddy viscosity model [5] is chosen for this study. The nondimensional parameters chosen for this code are the same as those in the CNS code [6]. The normalizing parameters are the freestream density $\tilde{\rho}_\infty$, the freestream sound speed $\tilde{a}_\infty$, the freestream viscosity coefficient $\tilde{\mu}_\infty$, and a characteristic length $\tilde{l}$.

The metrics used above have a different meaning for a finite volume formulation compared to the finite difference formulation of [6]. The finite volume metrics denoted by $(s_{\_,j+\frac{1}{2}}, s_{\_,k+\frac{1}{2}}, s_{\_,l+\frac{1}{2}})$ are the cell face area normals in each of the curvilinear coordinates (ξ, η, ζ) , see, for example, ref. [7]. They are related to the metrics introduced in eqns. (1 - 5) as follows

$$\begin{aligned}
\xi_x \hat{V} &= s_{x,j+\frac{1}{2}} \\
\xi_y \hat{V} &= s_{y,j+\frac{1}{2}} \\
\xi_z \hat{V} &= s_{z,j+\frac{1}{2}} \\
\\
\eta_x \hat{V} &= s_{x,k+\frac{1}{2}} \\
\eta_y \hat{V} &= s_{y,k+\frac{1}{2}} \\
\eta_z \hat{V} &= s_{z,k+\frac{1}{2}}
\end{aligned} \tag{8}$$

$$\zeta_x \hat{V} = s_{x,l+\frac{1}{2}}$$

$$\zeta_y \hat{V} = s_{y,l+\frac{1}{2}}$$

$$\zeta_z \hat{V} = s_{z,l+\frac{1}{2}}$$

where $\hat{V}$ is the volume of the computational cell.

Numerical Method

The governing equations are integrated in time for both steady and time accurate calculations. The unfactored linear implicit scheme is obtained by linearizing the flux vectors about the previous time and dropping second and higher order terms. The resulting scheme in finite volume form is given by

$$[I + \hat{V}^{-1}\hat{h}(\delta_\xi A^n + \delta_\eta B^n + \delta_\zeta C^n - Re^{-1}(\delta_\xi L^n + \delta_\eta M^n + \delta_\zeta N^n))]\Delta Q^n = -\hat{V}^{-1}\hat{h}R^n \quad (10)$$

where the residual R^n is

$$R^n = [\delta_\xi F^n + \delta_\eta G^n + \delta_\zeta H^n - Re^{-1}(\delta_\xi F_v^n + \delta_\eta G_v^n + \delta_\zeta H_v^n)] \quad (11)$$

The convective flux jacobians A, B, C and the viscous flux jacobians L, M and N are defined in the appendix of [1].

Solving the above equation set by direct matrix inversion is still not practical for three dimensional problems. However there are several indirect or approximate methods available, including the diagonal Beam-Warming scheme and the lower-upper (LU-SGS) factorized scheme of Yoon and Jameson. In a previous study [8], the LU-SGS scheme was the basic flow solver algorithm for the multi-zonal compressible Navier- Stokes finite volume code, CNSFV. While the scheme worked well for moderate Reynolds' numbers, the performance deteriorated with increasing Reynolds' numbers. Because of this problem, a modified LU-SGS scheme which is Reynolds' number independent is derived in this study. Descriptions of both schemes are presented below.

LU-SGS Scheme

The unfactored scheme of eqn. (10) is given in terms of central differences for the implicit operator. It can also be represented in terms of upwinded differences. Dropping the viscous terms in the implicit operator, eqn. (10) is in terms of upwind differences as follows:

$$[I + \hat{V}^{-1}\hat{h}(\delta_\xi^- A^+ + \delta_\xi^+ A^- + \delta_\eta^- B^+ + \delta_\eta^+ B^- + \delta_\zeta^- C^+ + \delta_\zeta^+ C^-)]\Delta Q^n = -\hat{V}^{-1}\hat{h}R^n \tag{12}$$

where δ_ξ^+ and δ_ξ^- are, for example, the forward and backward $\xi-$ difference operators. Similarly, A^+ and A^- are the Jacobian matrices which contain non-negative and non-positive eigenvalues, respectively.

The Yoon and Jameson version of the LU scheme can be obtained from the above equation by a simple reordering of the matrix elements and approximately factoring into two matrices. Define D, $\tilde{L}$, and $\tilde{U}$ to be matrices which contain the diagonal, sub-diagonal and super-diagonal elements of the implicit operator of eqn. (12), respectively.

$$[D + \tilde{L} + \tilde{U}]\Delta Q^n = -\hat{V}^{-1}\hat{h}R^n$$

which can be factored into

$$[D + \tilde{L}]D^{-1}[D + \tilde{U}]\Delta Q^n = -\hat{V}^{-1}\hat{h}R^n$$

Redefine $L = D + \tilde{L}$ and $U = D + \tilde{U}$ to yield the final form of the LU-SGS scheme.

$$LD^{-1}U\Delta Q^n = -\hat{V}^{-1}\hat{h}R^n \tag{13}$$

where

$$\begin{aligned} L &= I + \hat{V}^{-1}\hat{h}(\delta_\xi^- A^+ + \delta_\eta^- B^+ + \delta_\zeta^- C^+ - A^- - B^- - C^-) \\ D &= I + \hat{V}^{-1}\hat{h}(A^+ - A^- + B^+ - B^- + C^+ - C^-) \\ U &= I + \hat{V}^{-1}\hat{h}(\delta_\xi^+ A^- + \delta_\eta^+ B^- + \delta_\zeta^+ C^- + A^+ + B^+ + C^+) \end{aligned} \tag{14}$$

A variety of LU-SGS schemes can be obtained by different choices of the Jacobian matrices of the flux vectors. For robustness and to ensure that the scheme converges to a steady state, the matrices should be diagonally dominant. To ensure diagonal dominance, the Jacobian matrices can be constructed so that + matrices have nonnegative eigenvalues and − matrices have nonpositive eigenvalues. For example, the diagonalization used for the diagonal Beam-Warming scheme [2] can be used to obtain the ± matrices.

$$\begin{aligned} A^{\pm} &= T_{\xi}\Lambda_{\xi}^{\pm}T_{\xi}^{-1} \\ B^{\pm} &= T_{\eta}\Lambda_{\eta}^{\pm}T_{\eta}^{-1} \\ C^{\pm} &= T_{\zeta}\Lambda_{\zeta}^{\pm}T_{\zeta}^{-1} \end{aligned} \tag{15}$$

Another method to obtain diagonal dominance is to construct approximate Jacobian matrices:

$$\begin{aligned} A^{\pm} &= [A \pm \tilde{\rho}(A)I]/2 \\ B^{\pm} &= [B \pm \tilde{\rho}(B)I]/2 \\ C^{\pm} &= [C \pm \tilde{\rho}(C)I]/2 \end{aligned} \tag{16}$$

where $\tilde{\rho}(A) = max[|\lambda(A)|]$ and represent a spectral radius of the Jacobian matrix A with the eigenvalues $\lambda(A)$. These eigenvalues are, e.g., $\lambda(A) = U, U, U, U \pm a\sqrt{[s_x^2 + s_y^2 + s_z^2]_j}$, where the metric terms at cell centers are obtained by averaging the metrics defined by eqn. (8). Other methods of increasing the diagonal dominance of the LU operator include the addition of some approximation of the viscous terms and the artificial dissipation in the implicit operator [11].

The inversion of eqn. (13) is done in three steps. The block inversion along the diagonal is eliminated if the approximate Jacobian of eqn. (16) are used instead of eqn. (15). If first-order one-sided differences are used, eqn. (14) reduces to

$$\begin{aligned} L &= I + \hat{V}^{-1}\hat{h}(\tilde{\rho}I - A^{+}_{j-1,k,l} - B^{+}_{j,k-1,l} - C^{+}_{j,k,l-1}) \\ D &= I + \hat{V}^{-1}\hat{h}(\tilde{\rho}I) \\ U &= I + \hat{V}^{-1}\hat{h}(\tilde{\rho}I + A^{-}_{j+1,k,l} + B^{-}_{j,k+1,l} + C^{-}_{j,k,l+1}) \end{aligned} \tag{17}$$

where

$$\tilde{\rho} = \tilde{\rho}(A) + \tilde{\rho}(B) + \tilde{\rho}(C)$$

This algorithm requires only scalar diagonal inversions since the diagonal of L or $U = D$. The true Jacobians matrices of eqn. (15) may permit better convergence rates, but require block diagonal inversions with approximately twice the computational effort per iteration. This abstract considers the scalar version only, however the full matrix version will be included for comparison purposes in the full paper.

Modified LU-SGS

While the approximate jacobians obtained from the spectral radius splitting allows for scalar diagonal inversion and performs quite well for a large variety of flows, the approximation is rather crude and for flow cases where there is a large difference in the spectral radii, the convergence rates slow down. The spectral radii splitting alters all the characteristic speeds except for the maximum one. This is shown in the following table. Here the eigenvalues are compared to the exact splitting, eqn. (15), and the spectral radius splitting, eqn. (16). In the tabulation we assume subsonic flow with a positive convection speed so that one of the eigenvalues is negative and the remainder positive.

Eigenvalue	*exact*	*splitting*	*approximate*	*splitting*
unsplit	*similarity*	*transformation*	*spectral*	*radius*
λ	λ^+	λ^-	λ^+	λ^-
u	u	0	$u+a/2$	$-a/2$
u	u	0	$u+a/2$	$-a/2$
u	u	0	$u+a/2$	$-a/2$
$u+a$	$u+a$	0	$u+a$	0
$u-a$	0	$u-a$	u	$-a$

As can be seen from the table, the spectral radius splitting alters four out of the five characterstic speeds. The errors (defined as the deviation of the approximate values from the exact values relative to the spectral radius) can be as large as 50% in the subsonic and transonic Mach regime. Not until the flow reaches high supersonic mach numbers do the errors fall below 10%. These large errors in the eigenvalues of the approximate jacobians result in a poor linearization of the true jacobians and are the cause of the poor convergence rates. As the spectral radius increases, as for example for high Reynolds' number flows, the convergence rate deteriorates.

The exact eigenvalue splitting does not alter the characteristic speeds. But the advantage of the scalar diagonal matrix inversion is lost. One alternative method of splitting the eigenvalues while still maintaining the scalar inversion is to use the exact splitting in one direction only and spectral radius splitting in the remaining two directions. The obvious choice for the direction of the exact splitting is the direction with the largest spectral radius. This type of hybrid splitting produces a biased scheme if the choice is predetermined according to some expectation of the flow field spectral radii. The type dependent splitting can be automated so that the proper choice of the exact splitting direction is determined by the local values of the spectral radii in the three directions. The automated unbiased scheme is given by

$$TLD^{-1}UT^{-1}\Delta Q^n = -\hat{V}^{-1}\hat{h}R^n \tag{18}$$

with

$$\begin{gathered}
L = D - \hat{V}^{-1}\hat{h}\{[T^{-1}T_\xi(\lambda_\xi^+ + \frac{\epsilon}{2}\tilde{\rho}(\lambda_\xi)I)T_\xi^{-1}T]_{j-1,k,l} \\
+[T^{-1}T_\eta(\lambda_\eta^+ + \frac{\epsilon}{2}\tilde{\rho}(\lambda_\eta)I)T_\eta^{-1}T]_{j,k-1,l} + [T^{-1}T_\zeta(\lambda_\zeta^+ + \frac{\epsilon}{2}\tilde{\rho}(\lambda_\zeta)I)T_\zeta^{-1}T]_{j,k,l-1}\} \\
D = I + \hat{V}^{-1}\hat{h}\{(1+\epsilon)\tilde{\rho}I \\
+\omega_\xi[|\lambda_\xi| - \tilde{\rho}(\lambda_\xi)I] + \omega_\eta[|\lambda_\eta| - \tilde{\rho}(\lambda_\eta)I] + \omega_\zeta[|\lambda_\zeta| - \tilde{\rho}(\lambda_\zeta)I]\} \qquad (19)
\end{gathered}$$

$$\begin{gathered}
U = D + \hat{V}^{-1}\hat{h}\{+[T^{-1}T_\xi(\lambda_\xi^- - \frac{\epsilon}{2}\tilde{\rho}(\lambda_\xi)I)T_\xi^{-1}T]_{j+1,k,l} \\
+[T^{-1}T_\eta(\lambda_\eta^- - \frac{\epsilon}{2}\tilde{\rho}(\lambda_\eta)I)T_\eta^{-1}T]_{j,k+1,l} + [T^{-1}T_\zeta(\lambda_\zeta^- - \frac{\epsilon}{2}\tilde{\rho}(\lambda_\zeta)I)T_\zeta^{-1}T]_{j,k,l+1}\}
\end{gathered}$$

where

$$\begin{gathered}
T = \omega_\xi T_\xi + \omega_\eta T_\eta + \omega_\zeta T_\zeta \\
T^{-1} = \omega_\xi T_\xi^{-1} + \omega_\eta T_\eta^{-1} + \omega_\zeta T_\zeta^{-1}
\end{gathered}$$

and

$$\omega_\xi = Int\{\tilde{\rho}(\lambda_\xi)/max[\tilde{\rho}(\lambda_\xi), \tilde{\rho}(\lambda_\eta), \tilde{\rho}(\lambda_\zeta)]\}$$

$$\omega_\eta = Int\{\tilde{\rho}(\lambda_\eta)/max[\tilde{\rho}(\lambda_\xi), \tilde{\rho}(\lambda_\eta), \tilde{\rho}(\lambda_\zeta)]\}$$

$$\omega_\zeta = Int\{\tilde{\rho}(\lambda_\zeta)/max[\tilde{\rho}(\lambda_\xi), \tilde{\rho}(\lambda_\eta), \tilde{\rho}(\lambda_\zeta)]\}$$

The ω parameters are either unity or null and no more than one of them can be unity at any one location or instant. Because of the restrictions on the ω's the matrices T and T^{-1} are the inverse of each other. Furthermore matrices like $T^{-1}T_\xi$ dependent only on the metrics and not on the solution. Thus the scheme is not much more complicated than the standard LU-SGS scheme, eqn. (17). The terms in the modified LU-SGS scheme, eqn. (18) involving ϵ are due to the entropy fix (also called implicit residual smoothing) required to stabilize the scheme at the locations where the individual eigenvalues change sign. This smoothing is similar to that required in the flux vector splitting scheme of Steger and Warming. The full paper will go into more detail in developing the modified LU-SGS scheme and discuss accuracy and stability issues.

Results

For this abstract two set of results will be presented. The first set is a series of Mach 2 flat plate boundary layer flows with increasing Reynolds' numbers to demonstrate the influence of increasing cell aspect ratio on the convergence rates of the standard and modified LU-SGS schemes. The second set of results is for a Mach 14.1 compression ramp flow to compare the two schemes with a more realistic and complicated flow field. The full paper will consider other configurations and flow situations to fully exercise the new scheme and verify the improved performance.

Flat Plate Boundary Layer

The flat plate bondary layer flow consists of a laminar flow over a flat plate at Mach 2, isothermal walls with the wall temperature fixed at the free stream values. Three different Reynolds' numbers were chosen to represent typical Reynolds' number encountered in typical configurational aerodynamics, namely 10^6 and 10^8 which are typical for flows over isolated wings and complete aircraft (e.g. HSCT), respectively. Finally a low Reynolds' number of 10^4 was also chosen to test the performance of the schemes for highly viscous flows. The computational grids have variable spacing in the wall normal direction with an initial normal spacing such that the y^+ is less than 5 for all three cases. The actual y^+ varies since the number of points in the boundary layer was fixed at 20 for all three Reynolds' numbers. The stretching rate was also fixed at 1.1. The streamwise spacing is constant for all three cases at 0.1. The cell aspect ratio varied from 20 at the low Reynolds' number range to 600 at the high range.

The convergence rates with the standard LU-SGS scheme at the three Reynolds' numbers is shown in figure 1 for a fixed time step with the indicated maximum CFL number. As the Reynolds' number is increased the performance rapidly deteriorates. At the highest Reynolds' number almost 60000 iterations are required to drive the residual to machine accuracy on a Cray YMP. The use of local time step scaling such that each computational cell is updated with the same CFL number is shown in figure 2. As shown the local time step scaling does not improve the performance of the standard LU-SGS scheme.

The performance of the modified LU-SGS scheme is quite different. For the case where ω_ξ is fixed at unity and ω_η is zero, the modified scheme behaves the same as the standard scheme. This is as expected since the maximum spectral radius is in the η-direction and thus the modified scheme does not treat the largest eigenvalues any more accurately than the standard scheme. If the value of the ω_η is now fixed at one and $\omega_\xi = 0$, then a sharp increase in the convergence rates is noted for both the fixed time step and locally scaled time step cases. The only exception seems to be for the fixed time step run at the lowest Reynolds' number. The reason seems to be that at this Reynolds' number the leading edge shock is quite strong and the maximum spectral radius is not in the η (wall normal) direction. At the highest Reynolds' number the performance of the modified scheme improved by a factor of 20 for the fixed time step case to 60 for the locally scaled time step case.

Compression Ramp

The next case tested with the new scheme is the compression ramp at a hypersonic Mach number of 14.1. The Reynolds' number is a moderate 10^5. This case has experimental data available in ref. 14. Figure 3 shows the convergence rate comparison for the two schemes. As can be expected from the flat plate results only a moderate improvement is noted due to the low Reynolds' number. The remaining two figures show the skin friction and surface pressures along the compression ramp. In these figures x_{ref} is the location of the foot of the ramp. The agreement with the experimental results is good and the results obtained with the two schemes were identical as expected.

The above results are obtained with the 2nd order accurate Roe's upwind scheme for the explicit operator on the right hand side of eqn. (18). In the full paper the other cases to be compared will also include the central difference scheme with the 2nd and 4th order smoothing in the explicit operator.

Conclusions

A modification to the standard LU-SGS scheme is developed and shown to be essentially independent of Reynolds' numbers and cell aspect ratio effects. For high Reynolds' number flows the scheme is shown to be robust and exhibit rapid convergence rates. The new scheme is not much more complicated than the original scheme. Hopefully with the present modification more utilization of the LU-SGS scheme will be seen for production Navier-Stokes codes.

Acknowledgments

The first author's work was supported by NASA Grant NCC2-616 and the second author's by NASA Grant No. NAGW-1331 to the Mars Mission Research Center, additional support has been allocated by the NASA Ames Research Center, Moffett Field, CA under Interchange No. NCA2-719.

References

1. Beam, R. and Warming, R. F.; "An Implicit Factored Scheme for the Compressible Navier-Stokes Equations," AIAA Journal, Vol. 16, Apr. 1978, pp. 393-402.

2. Pulliam, T. H. and Chaussee, D. S.; "A Diagonal Form of an Implicit Approximate Factorization Algorithm," Journal of Computational Physics, Vol. 39, 1981, pp. 347-363.

3. Yoon, S. and Jameson, A.; "Lower-Upper Symmetric Gauss Seidel Method for the Euler and Navier-Stokes Equations," AIAA Journal, Vol. 26, Sept. 1987, pp. 1025-1026.

4. Yoon, S. and Kwak, D.; "An Implicit Three-Dimensional Navier-Stokes Solver for Compressible Flow," AIAA Paper 91-1555-CP, June 1991.

5. Baldwin, B. S. and Lomax, H.; "Thin-Layer Approximation and Algebraic Model for Separated Turbulent Flow," AIAA Paper 78-0257, Jan. 1978.

6. Flores, J. and Chaderjian, N. M.; "Zonal Navier-Stokes Methodology for Flow Simulations about Complete Aircraft," Journal of Aircraft, Vol. 27, No. 7, July 1990, pp. 583-590.

7. Vinokur, M.; "An Analysis of Finite Difference and Finite Volume Formulation of Conservation Laws," NASA CR-177416, June 1986.

8. Klopfer, G. H. and Yoon, S.; "Multizonal Navier-Stokes Code with the LU-SGS Scheme," AIAA Paper 93-2965, July 1993.

9. Chaussee, D. S. and Klopfer, G. H.; "The Numerical Study fo 3-D Flow Past Control Surfaces," AIAA Paper 92-4650, August 1992.

10. Turkel, E. and Vatsa, V. N.; "Effect of Artificial Viscosity on Three-Dimensional Flow Solutions," AIAA Paper 90-1444, June 1990.

11. Shih, T. I-P., Steinthorsen, E., and Chyu, W. J.; "Implicit Treatment of Diffusion Terms in Lower-Upper Algorithms," AIAA J., Vol. 31. No. 4, 1993, pp. 788-791.

12. Schmitt, V. and Charpin, F.; "Pressure Distributions on the ONERA M6 Wing at Transonic Mach Numbers," AGARD-AR-138, Report of the Fluid Dynamics Panel, May 1979.

13. Rumsey, C. L. and Vatsa, V. N.; "A Comparison of the Predictive Capabilities of Several Turbulent Models Using Upwind and Central-Difference Computer Codes," AIAA Paper 93-0192, Jan. 1993.

14. Holden, M. S. and Moselle, J. R.; "Theoretical and Experimental Studies of the Shock Wave-Boundary Layer Interaction on Compression Surfaces in Hypersonic Flow," CALSPAN, Buffalo, New York, Report AF-2410-A-1, Oct. 1969.

List of Figures

Figure 1. Convergence rate for the standard and modified LU-SGS schemes for Mach 2 flat plate boundary layer flows at three Reynolds' numbers. Fixed time step with the indicated maximum CFL number.

Figure 2. Convergence rate for the standard and modified LU-SGS schemes for Mach 2 flat plate boundary layer flows at three Reynolds' numbers. Locally scaled step with uniform CFL numberas indicated.

Figure 3. Convergence rate for the standard and modified LU-SGS schemes for Mach 14.1 compression ramp flow at $Re = 10^5$.

Figure 4. Skin friction coefficient for Mach 14.1 compression ramp flow at $Re = 10^5$.

Figure 5. Pressure coefficient for Mach 14.1 compression ramp flow at $Re = 10^5$.

APPENDIX - C

AIAA-95-0749

NZB

Aerodynamic Computations for a High-Speed, Magnetic-Flight System

Klopfer, G.H. and
Mehta, U. B.
MCAT Institute
Moffett Field
California

NDB

AIAA-95-0749

Aerodynamic Computations for a High-Speed, Magnetic-Flight System

Goetz H. Klopfer
MCAT Institute
NASA Ames Research Center
Moffett Field, CA 94035-1000

and

Unmeel B. Mehta
NASA Ames Research Center
Moffett Field, CA 94035-1000

33rd Aerospace Sciences Meeting and Exhibit
January 9-12, 1995 / Reno, NV

For permission to copy or republish, contact the American Institute of Aeronautics and Astronautics
370 L'Enfant Promenade, S.W., Washington, D.C. 20024

Aerodynamic Computations for A High-Speed, Magnetic-Flight System

Goetz H. Klopfer
MCAT Institute, NASA Ames Research Center, Moffett Field, California
and
Unmeel B. Mehta*
NASA Ames Research Center, Moffett Field, California

Abstract

Computations are carried out to study the aerodynamics associated with magnetic flight, an advanced concept for a high-speed transportation system. Three-dimensional, thin-layer, Reynolds-averaged Navier-Stokes equations are solved with an implicit, factored, finite-volume scheme. An algebraic turbulence model is used. Experimental data for turbulent Couette flows without pressure gradients verify the computed velocity profiles in such flows. A computational fluid dynamics design tool is developed for conducting aerodynamic trade-off studies related to magnetic flight vehicles. A more complex turbulence model and much finer grid-resolution are needed for quantitatively accurate computations. The base region of the magnetic flight vehicle is as important as the nose region in reducing overall vehicle drag.

Introduction

The Committee on Aeronautical Technologies of the National Research Council has sought evolutionary improvements in the conventional aeronautical transportation systems for the twenty-first century.[1] The Committee recommended how these improvements may be achieved, but it did not suggest a new mode of propulsion for achieving them. As correctly observed by H. Julian Allen at the beginning of his Twenty-First Wright Brothers lecture, "[p]rogress in transportation has been brought about more by revolutionary than by evolutionary changes in methods of propulsion."[2] A magnetically propelled system that "flies" may lead to a revolutionary progress in transportation. Magnetic flight (which we call Magflite) is an advanced concept for a high-speed transportation system in which vehicles glide above their guideways – suspended, guided, and propelled by magnetic forces. The vehicles lift off the ground because of magnetic levitation (usually called Maglev). This levitation technique requires the vehicles to fly very close to the guideway. The development of this kind of transportation system hinges on proven aerospace technologies.[3] For example, there are technical risks associated with the vehicle/guideway interaction and with the adverse effects of aerodynamic forces and moments.[4–6] These issues can only be addressed using computational fluid dynamics (CFD), because wind-tunnel tests at high-speeds are not feasible. This paper presents a progress report for developing CFD-design tools for use in investigating the aerodynamics of Magflite.

The technologies used in existing civil and military transportation systems are nearing saturation in terms of performance and efficiency. At best, these systems can be improved only incrementally. Furthermore, it is unlikely that the commercial systems and the systems derived from the military transportation systems will meet projected demands for intercity transportation by the 2020-2025 time period. The goal of a new commercially feasible transportation system is to complement existing modes of transportation (airplanes, automobiles, and trains). Magflite vehicles can travel at speeds of 250 miles/hour (402 km/hr) or higher. This mode of transportation offers an attractive and convenient alternative for travelers on trips between large urban areas or on trips over distances up to 600 miles (964 km). It would also relieve projected transportation congestion on the highways and at airports. In addition to this utility of Magflite for ground transportation, Magflite offers the following aeronautical opportunities: (1) Earth-to-orbit launch systems may be launched with Magflite-based catapults;[7] (2) hypersonic research vehicles can be launched with catapults using Magflite; and (3) hypersonic test and development activities can be conducted with Magflite test tracks.[8]

---

*Associate Fellow, AIAA.

Copyright © 1995 by the American Institute of Aeronautics and Astronautics, Inc. No copyright is asserted in the United States under Title 17, U. S. Code. The U. S. Government has a royalty-free license to exercise all rights under the copyright claimed herein for Governmental purposes. All other rights are reserved by the copyright owner.

At low speeds, aerodynamic forces play a negligible role and the electromagnetic forces dominate. With increasing speeds, aerodynamic forces increase and eventually become significant. Overcoming aerodynamic drag on the vehicles is the dominant factor in energy consumption at 300 miles/hr (482 km/hr).[5] The system drag is composed of, for example, exposed skin friction, gap skin friction within the guideway, forebody drag, base drag, intercar joint or protuberance drag, and induced drag of aerodynamic control surfaces. Minimizing the system drag will lead to a more cost-efficient vehicle requiring less energy for propulsion and guidance. In addition, at speeds above 155 miles/hr (249 km/hr), most of the noise produced by a vehicle is of aerodynamic origin.[5]

Four Magflite concepts were developed under the National Maglev Initiative (NMI).[4,5] In three of these concepts, an electrodynamic suspension (EDS) system is used and in the fourth, an electromagnetic suspension (EMS) system is used. The Japanese Magflite trains (MLU001, MLU002, and MUL002N) use the EDS system, whereas the German Magflite train (TR07) uses the EMS system. The dimensions of the air gaps between these trains and their guideways vary from 0.4 in (1 cm) to 5.9 in (15 cm).

A CFD-design tool utilizes appropriate models for the physics and for the computations necessary to provide trends or increments in performance quantities and global flow features at an affordable cost. This requirement means, for example, that simple rather than complex turbulence models and fewer grid-points rather than more are preferable, and that fine scale details are not important. In order to demonstrate some aspects of the CFD-design tools that have been developed for studying the flight of a vehicle in extreme ground effects, computations are presented for a generic Magneplane EDS system.[9] The emphasis is on computing satisfactorily the skin friction of the unexposed part of the vehicle by using an algebraic turbulence model.

Previous Studies

A limited amount of experimental force data exist for unpowered, high-speed vehicles moving very close to the ground. In a series of tests, the cross-wind effects on the aerodynamic forces and moments of six models were investigated.[10] These tests were conducted over a moving-belt ground plane at a free-stream dynamic pressure of 10 lb/ft^2 (478.8 N/m^2), corresponding to a free-stream velocity of approximately 60 miles/hr (96 km/hr) and to a Reynolds number based on a free-stream velocity and model length of about 3.7×10^6. There were some difficulties in accurately maintaining the distance between the test model and the moving belt at small gap heights because of belt deflection. Other limitations of wind-tunnel tests involved Reynolds number scale effects. Wind-tunnel tests at speeds in excess of 250 miles/hr (402 km/hr) are not possible at present. The achievable Reynolds numbers in these tunnels are two orders of magnitude smaller than those likely to be observed for high-speed Magflite vehicles. Moreover, actual wind-tunnel simulation of either the EMS or the EDS system with its guideway is not possible.

In Ref. 11, a CFD study was conducted for a Magflite vehicle in which three-dimensional, Reynolds-averaged Navier-Stokes computations were carried out for a generic form of the Grumman concept. In this concept, the underside of the vehicle was wrapped around an elevated V-shaped guideway. The vehicle had a drooped nose and tail for aerodynamic efficiency; there was about 2 inches (5 cm) of clearance between the vehicle and the guideway for the EMS with superconducting magnets. The flow field around the vehicle, including the flow field in the gap, was simulated with a finite-volume, multistage Runge-Kutta explicit time-integration scheme and the Baldwin-Lomax model on a single grid block containing 468, 149 grid-points. The free-stream flow conditions were $M_\infty = 0.4$ and $Re \approx 9.17 \times 10^6/\text{m}$, corresponding to a speed of 298 miles/hr (480 km/hr). The computed velocity profiles in the gap did not approach the developed, plane-turbulent Couette flow profile.

In Ref. 12, a CFD code was claimed to be validated for use as a design tool by verifying only computed pressure distributions with those obtained in field testing of the Japanese MLU002 train. An implicit, approximately factored finite-difference procedure is used to solve the three-dimensional, thin-layer, Reynolds-averaged Navier-Stokes equations on 840, 000 grid-points. The free-stream flow conditions were $M_\infty = 0.41$ and $Re \approx 9.28 \times 10^6/\text{m}$, corresponding to a speed of 310 miles/hr (500 km/hr). An algebraic turbulence model of the Baldwin-Lomax type was used. This code was then used to quantitatively evaluate several candidate frontal shapes so that the shape with the minimum aerodynamic drag could be chosen.[13] The outcome of this trade-off study in terms of the preferred shape may be acceptable, but the credibility of the actual value of drag was not established.

Approach

In the present study, a finite-volume method for space discretization is used to avoid problems related to metric singularities and to conserve the conservative variables. The thin-layer, Reynolds-averaged Navier-Stokes equations are integrated in time for steady-state computations by using an implicit time-stepping method. Central differences are used to model the continuous spatial derivatives. Second-

and fourth-order numerical dissipation are utilized to control high-frequency nonlinear discretization errors. The unfactored linear implicit scheme is obtained by linearizing the flux vectors about the previous time-step and dropping the second- and higher-order terms. The scheme is factored in terms of directions. This scheme is implemented in the multi-zonal code called CNSFV, and the results obtained from this code are verified with wind-tunnel data for a turbulent simulation of attached transonic flow around an ONERA M6 wing.[14,15]

Computational grids are generated by using the GRIDGEN code.[16] Multiple grid blocks are generated by appropriate zoning of the flow field domain. Because of the smallness of the gap between the guideway and the Magflite vehicle, the generation of an appropriate grid system is the major challenge of this investigation. Special attention is also required in distributing the surface grid points to maintain grid orthogonality at the boundaries and to globally minimize grid skewness, and to resolve the flow in the viscous/shear layers satisfactorily. In each zone the flow field is solved separately from the other zones. The boundary data for each zone are provided by its neighboring zones.

The flow in the wake of the Magflite vehicle, in the gap, and along the exposed portion of the vehicle, except in the boundary layer on the nose region, would be turbulent. Computations are done with the assumption that the flow is fully turbulent. The flow in the gap between a single bogie of the vehicle and the guideway is the Couette flow, except for the fact that there would be some flow release from the sides of the gap. This gap flow is analogous to the basic flow problem occurring in all hydrostatic, hydrodynamic, thrust, and slider bearings. In the absence of free-stream cross-flow, along the plane of symmetry the flow is the two-dimensional developing, plane-turbulent Couette flow. Parts of this Couette flow would be under the influence of pressure gradients, particularly near the nose of the vehicle. The Baldwin-Lomax model[17] is used everywhere except in the gap, where it is adjusted to match the computed wall skin friction and velocity profile with experimental data[18] and computed results,[19] for plane, zero-pressure-gradient turbulent Couette flow.

The Baldwin-Lomax model is expressed in terms of a turbulence velocity scale v and a turbulence length scale ℓ. On dimensional grounds, a combination of these scales determines the value of the kinetic eddy viscosity:

$$\nu_t = c_t v \ell \tag{1}$$

where c_t is sometimes referred to as the Clauser constant. From this expression we can determine the dynamic eddy viscosity, $\mu_t = \rho\nu_t$.

The turbulent boundary layer is regarded as a composite layer consisting of inner and outer regions. In each region, the distributions of v and ℓ are prescribed by two different empirical expressions. In the inner (log-law) region, ℓ is proportional to y, the distance normal to the wall. In the outer layer, ℓ is proportional to the shear-layer thickness. In the inner region, the proportionality of ℓ to y is extended to the viscous sublayer using the Van Driest damping function. In the outer (wake) region, the vorticity, $\overline{\Omega}$, is used to define the boundary-layer thickness.

The region of validity of the inner and outer scales is determined by y_c, which is defined to be the smallest value of y at which the values of the inner and outer eddy viscosity are the same. The Baldwin-Lomax model is an eddy-viscosity type of turbulence model, and is not valid for flows with anisotropic turbulence intensities.

In the inner layer, $0 \leq y \leq y_c$, the expressions for v and ℓ are

$$\begin{aligned} (v)_{inner} &= \ell|\overline{\Omega}| \\ (\ell)_{inner} &= \alpha_1 y\left[1 - e^{(-y^+/A^+)}\right] \\ A^+ &= 26 \end{aligned} \tag{2}$$

with $\alpha_1 = 0.40$ in Eq. (2) and $c_t = 1.0$ in Eq. (1). In this case, the wall coordinate y^+ in Eq. (2) is based on the value of the density at the wall.

In the outer region, where $y > y_c$, the expressions for v and ℓ are

$$\begin{aligned} (v)_{outer} &= minimum \quad of\left(L_{max},\ \frac{U_{diff}^2}{4L_{max}}\right) \\ (\ell)_{outer} &= y_{max} C_{BL}\, \alpha_2 \end{aligned} \tag{3}$$

If the function $L(y)$ is defined to be

$$L(y) = y|\overline{\Omega}|\left[1 - e^{(-y^+/A^+)}\right] \tag{4}$$

the quantity L_{max} is the maximum value of $L(y)$ that occurs in this equation, and y_{max} is the value of y at which it occurs. The above exponential term is negligible in the outer part of the shear layer. The quantity U_{diff} is the difference between the absolute velocity at y_{max} and the minimum value of the absolute velocity, the value of C_{BL} is 1.6, and the Klebanoff intermittency factor, α_2, is given by

$$\alpha_2 = \left[1 + 5.5\left(\frac{C_K y}{y_{max}}\right)^6\right]^{-1} \tag{5}$$

where the Klebanoff constant $C_K = 0.3$. The Clauser constant c_t, in Eq. (1), is

$$c_t = 0.0168 \tag{6}$$

Turbulent Couette Flow

Plane-turbulent Couette flows in the absence of a streamwise pressure gradient are computed to study the effects of grid resolution and numerical dissipation and to develop an engineering/design turbulence model. This flow is characterized primarily by the following facts: (1) the velocity profile is S-shaped; (2) the cross-stream gradient of the shear stress is zero, that is, the shear stress is uniform across the gap; (3) both the mean vorticity and turbulent shear stress are symmetric about the center of the gap, yielding a finite production rate of turbulent kinetic energy even in the core region; and (4) the turbulence intensities manifest themselves in an anisotropic turbulence structure.[20] An attempt is made to reproduce these flow characteristics in the computations.

Uniform grid-cells are used in the Couette flow computations simply because uniform grid-cells are used in the computation of the gap flow when the Magflite flow is simulated. The computations are carried out until the errors, that is, the residuals, in the governing equations are reduced by at least four orders of magnitude. In all Couette flow computations, Reynolds numbers are based on the gap height and maximum velocity and a Mach number of 0.2 is used.

The effect of grid resolution on the velocity profile and previous experimental and computed profiles are shown in Fig. 1. In this figure the phrase "inner model" refers to Eq. (2). The measurement accuracy of the test data is not available. The previously computed results[19] were obtained using the Elrod-Ng turbulence model. This model is not used in the present study, because it is developed for and applicable to only the gap region. Note that Ref. 19 provides no information about the computational grid resolution. With the same turbulence model and the same numerical fourth-order dissipation coefficient (dis4), the present results for 120 and 240 grid-cells are comparable, but those for 60 grid-cells are slightly off. However, a smaller value of the coefficient of fourth-order numerical dissipation makes the velocity profile with 60 cell-centers comparable to those presented with finer grids (Fig. 2).

The Baldwin-Lomax model does not predict the slope of the velocity profile away from the walls (Fig. 3). The outer/wake model (Eq. (3)) is activated at $y^+ \approx 100$ rather than at about 1,000 (Fig. 4). Because of this shortcoming, the outer model is not used. The inner turbulence model alone gives the desired slope of the velocity profile in the core region of the gap with 60 uniform grid-cells (Fig. 3). Another goal is to obtain the right value of skin friction at the walls with the inner model. This goal is achieved by adjusting the Clauser constant. Its appropriate value is found to be 0.16 when the coefficient of the fourth-order dissipation term is reduced to 10^{-6}. These adjustments in the turbulence model and numerical dissipation give local friction coefficients that are almost constant across the gap (Fig. 5) and that are almost comparable with the test data (Fig. 6). The friction coefficient is normalized by the averaged velocity in the gap. Note that the value of y^+ at the first cell-center off the wall is about 8.5, with 60 cell-centers in the gap (Fig.5).

The effect of grid resolution on wall skin-friction coefficient is shown in Fig. 7. Test data from Ref. 18, computed values from Ref. 19, and the extrapolation of these results to higher Reynolds numbers are also shown. At low Reynolds numbers, the computed wall friction coefficients with 120 and 240 grid-cells are comparable to the experimental values. In particular, at higher Reynolds numbers the values of the friction coefficient are not acceptable when 60 grid-cells are used. Figure 8 shows that the difference between the values of the friction coefficients at the wall and at the center of the gap increases with increasing value of the coefficient of the fourth-order dissipation, given the same turbulence model and the same number of grid-cells, namely, 60. Over the investigated Reynolds number range, the differences between the values of the friction coefficients at the wall and those at the centerline are the smallest, and the actual values are on the whole closer to the test data and their extrapolated values, but only if the inner model is used with the Clauser constant being 0.16 and if the value of the coefficient of fourth-order dissipation term is reduced to 10^{-6} (Fig. 6). The highest Reynolds number considered is $Re = 1.35 \times 10^6$. This Reynolds number corresponds to $Re = 9 \times 10^6$ per meter, which is used for the Magflite vehicle flow computations. Figure 9 shows that the local friction coefficient is nearly constant and that y^+ at the first cell-center is about 55.

Computations Around a Magflite Vehicle

A conceptual, single bogie Magflite vehicle[21] (Fig. 10) is used to study the extreme ground effects encountered by such vehicles. This system uses a trough-shaped guideway for guidance. There are three body sections – nose, center, and rear. For each section, the cross-section coordinates are obtained by following the sequence of derived parameters, starting with the given parameters and their values. This procedure is illustrated for the center region in Fig. 10(c). Twelve grid blocks, with a total of 876,912 grid-cells, are used to discretize the flow field (Fig. 11). Figure 12 shows this system and the computational grids in the symmetry plane. The 5.9 in (15 cm) gap between the the vehicle and the guideway contains 60 grid-cells (the number of grid-cells was constrained to keep the computational time affordable). In all blocks, Cartesian grid systems are used, except in the vehicle-base block and in the upstream plane of the nose block where polar grid systems are utilized.

Both the air and the guideway are moving at free-stream velocity corresponding to $M_\infty = 0.4$ and $Re = 9 \times 10^6$ per meter, while the vehicle is stationary. The no-slip condition and no-temperature-gradient condition are applied on the guideway and vehicle surfaces. At the far-field boundaries, characteristic types of boundary conditions are applied at the inflow and outflow planes, and free-stream conditions are imposed on the remaining boundaries. The "ground" plane connecting the far-field to the guideway was also treated as a moving, no-slip, adiabatic boundary. In the gap between the vehicle and the guideway, the scaled inner turbulence model (discussed in the previous section) is used. Everywhere else the Baldwin-Lomax model is used. Instead of using 10^{-6} as the value of the fourth-order dissipation coefficient in the gap, its value is varied as follows. At all grid-cells, except the four cell-centers next to the wall, the value of this coefficient is chosen to be 0.05. This value is reduced by one order of magnitude at each cell-center as the wall is approached until its value is 0.00005 at the cell-center next to the wall. This variation of dis4 was used to speedup the dissipation of pressure transients.

The flow field was initialized by the free-stream condition and the no-slip boundary condition was slowly turned on over 30 time-steps. The trick employed in the Couette flow computations was to initialize the flow field with one half the free-stream speed and to accelerate the wall to full speed over several dozen time-steps. This procedure was not employed. Initially, the fourth-order dissipation was not reduced in the wall region until the major transients had dissipated. Most of the transients consisted of pressure waves propagating longitudinally in the gap region. These pressure waves persisted for a surprisingly long time. The convergence rate was accelerated by the use of local time-stepping. Other acceleration methods were not employed, but will be needed for future computations. The calculations were halted after the residuals were reduced by three to five orders of magnitude.

Pressure contours on the guideway surface and on the vehicle surface are shown in Fig. 13. The nose and the tail regions of the vehicle are the high-pressure regions, and the regions surrounding the junctions of the nose and the center body and of the tail and the center body are low-pressure regions. The stream surfaces emanating from the nose region, from the side, and from under the vehicle travel toward the upper surface of the vehicle (Fig. 14). Because of the blunt base of the tail region, these surfaces roll up into two large streamwise vortices in the near wake of the vehicle. The base region of this vehicle contributes the most to the vehicle drag.

The surface particle traces emanating from the nose region and traveling along the length of the vehicle are shown in Figs. 15 and 16. In the nose region the upper surface flow moves to the side and over the cusp line of the vehicle and immediately after crossing this line the flow separates. The flow near the nose is sucked into the gap region. Along the main body of the vehicle and along its tail, the flow gradually escapes from the gap region and moves upward on the vehicle.

The development of the velocity profile along the guideway in the plane of symmetry is shown in Fig. 17. As the nose of the vehicle is approached, the flow is retarded upstream of the vehicle. A developing turbulent Couette flow is now observed under the vehicle. Around station 5 the air is moving in the core region of the gap faster than the guideway. At station 10, there is still accelerated flow in the core. Around station 30 the flow is like a plane-turbulent Couette flow. Downstream of the gap the flow departs from this Couette-type of flow.

Concluding Remarks

In conclusion, the following remarks are set out:

1. A CFD-design tool is developed for conducting trade-off studies.
2. The credibility of computations is indirectly established by presenting the credibility of computed plane-turbulent Couette flow in the absence of a streamwise pressure gradient.
3. Numerical dissipation should not be used in the direction normal to the wall in the boundary layer.
4. Quantitatively accurate Magflite computations require a turbulence model more complex those based on the eddy-viscosity concept and more grid-cells than those used.
5. The shaping of both the nose region and the tail region is important for reducing the vehicle aerodynamic drag.

Acknowledgment

The assistance provided by Dr. Kalpana Chawla of Overset Methods, Inc. and by Mr. David Baker, a graduate student at California Polytechnic College, San Luis Obispo, for generating the 12-block grid system is appreciated.

References

[1] *Aeronautical Technologies for the Twenty-First Century*, Aeronautics and Space Engineering Board,

National Research Council, 1992.

[2] Allen, H. J., "Hypersonic Flight and the Re-entry Problem," The Twenty-First Wright Brothers Lecture, *Journal of the Aerospace Sciences*, Vol. 25, No. 4, April 1958.

[3] DeMeis, R., "Magnetic Levitation for the Masses," *Aerospace America*, Sept. 1993.

[4] *Maglev for the United States*, U. S. Army Corps of Engineers, 1993.

[5] *Final Report on The National Maglev Initiative (NMI)*, DOT/FRA/NMI-93/03, Sept. 1993.

[6] deBenedet, D., Gilchrist, A. J., and Karanian, L., "Maglev Program Test Plan," Final report No. DOT/FRA/NMI-92/11, Martin Marietta Corporation, Air Traffic Systems Division.

[7] Mankins, J. C., "The MagLifter: An Advanced Concept Using Electromagnetic Propulsion in Reducing the Cost of Space Launch," AIAA Paper 94-2726.

[8] "Holloman Sled Track Targets Mach 12, Magnetic Levitation," *Aviation Week & Space Technology*, June 13, 1994.

[9] *System Concept Definition Report*, Magneplane International, Inc., September 1992.

[10] Grunwald, K. J., "Aerodynamic Characteristics of Vehicle Bodies at Crosswind Conditions in Ground Proximity," NASA TN D-5935, August 1970.

[11] Siclari, M. J., Carpenter, G., and Ende, R., "Navier-Stokes Computation for a Magnetically Levitated (Maglev) Vehicle in Ground Effect," AIAA Paper 93-2950.

[12] Kaiden, T., Hosaka, S., and Maeda, T., "A Validation of Numerical Simulation with Field Testing of JR Maglev Vehicle," STEC Japan, November 1993.

[13] Miyakawa, J., and Hosaka, S., "Aerodynamic design of Frontal Shape for JR Maglev Train," STEC Japan, November 1993.

[14] Klopfer, G. H., Molvik, G. A., "Conservative Multizonal Interface Algorithm for the 3-D Navier-Stokes Equations," AIAA Paper 91-1601.

[15] Klopfer, G. H., and Yoon, S., "Multizonal Navier-Stokes Code with the LU-SGS Scheme," AIAA Paper 93-2965.

[16] "The GRIDGEN 3D Multiple Block Grid Generation System, Vol. II: User's Manual," WRDC-TR-90-3022, February 1991; and GRIDGEN code, Version 8.

[17] Baldwin, B. S., and Lomax, H., 1978, "Thin Layer Approximation and Algebraic Model for Separated Turbulent Flows," AIAA Paper 78-257.

[18] Robertson, J. M., "On Turbulent Plane-Couette Flow," 6th Midwestern Conference on Fluid Mechanics, University of Texas, 1959.

[19] Elrod, Jr, H. G., and Ng, C. W., "A Theory for Turbulent Fluid Films and its Application to Bearings," *Transactions of the ASME Journal of Lubrication Technology*, July 1967.

[20] El Telbany, M. M. M., and Reynolds, A. J., "Velocity Distributions in Plane Turbulent Channel Flows," J. Fluid Mech., Vol. 100, Pt. 1, 1980.

[21] Judd, M., MIT Lincoln Laboratory, *private communication*, 1993.

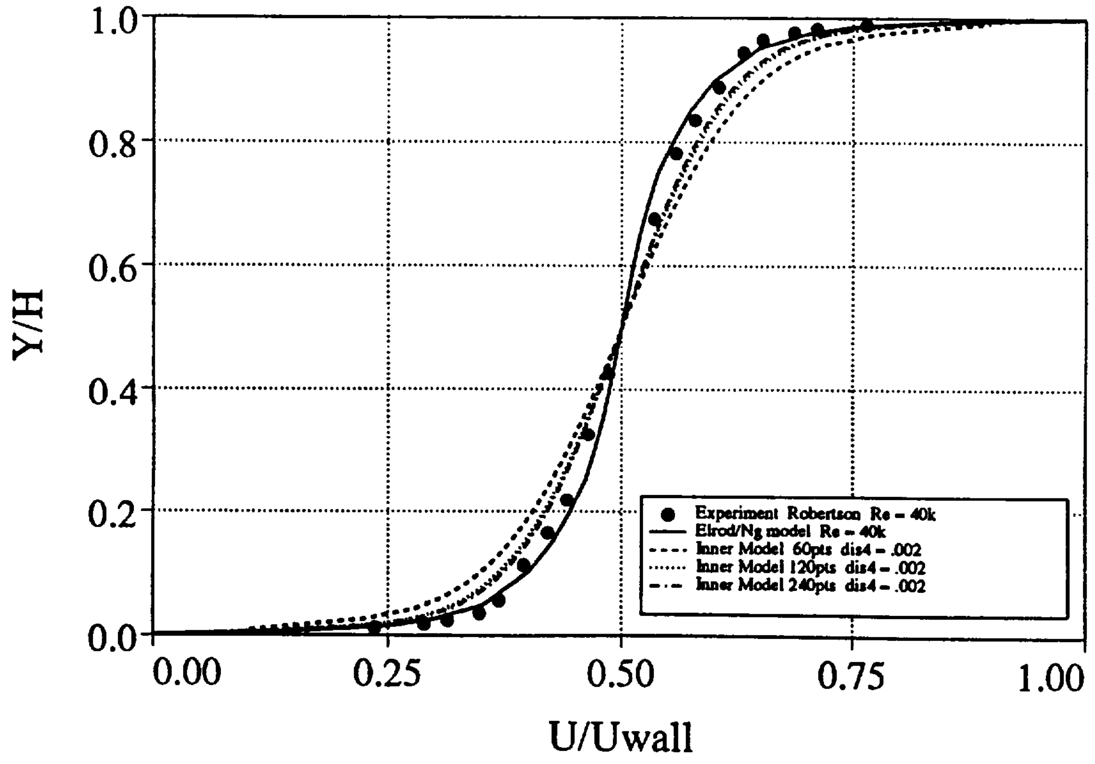

Figure 1. The effect of grid resolution on plane turbulent Couette flow velocity profile. Present computations at Re = 38,180.

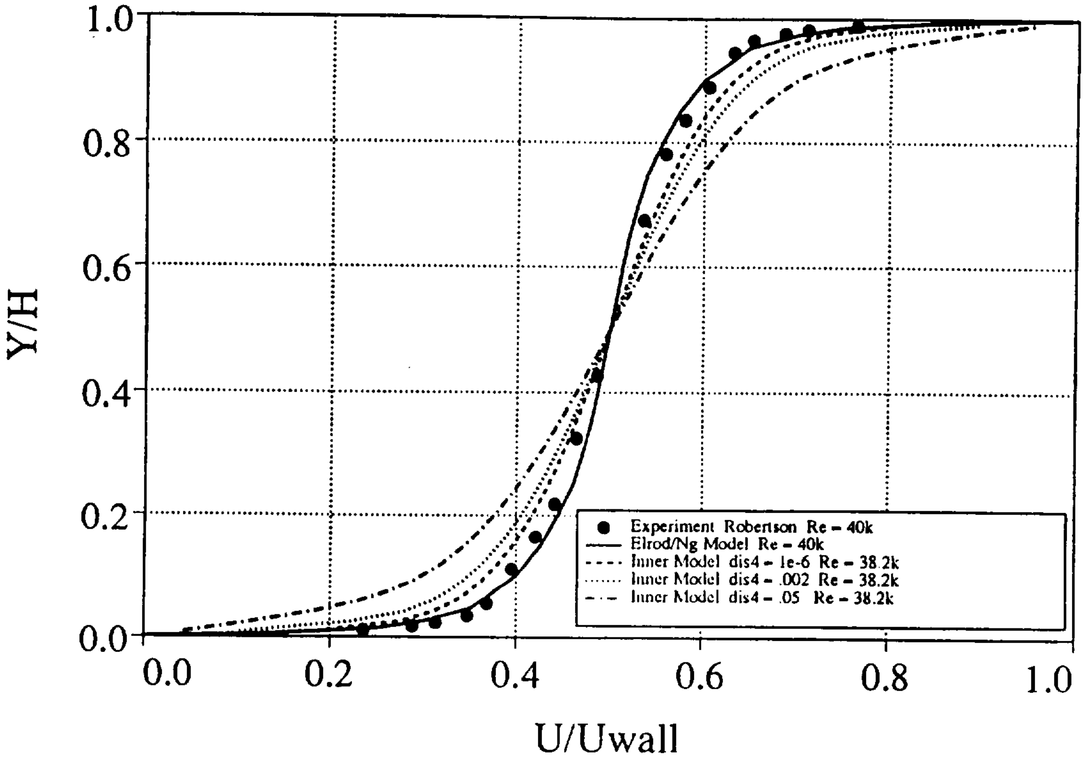

Figure 2. The effect of numerical viscosity on plane turbulent Couette flow velocity profile. Present computations with 60 grid-points.

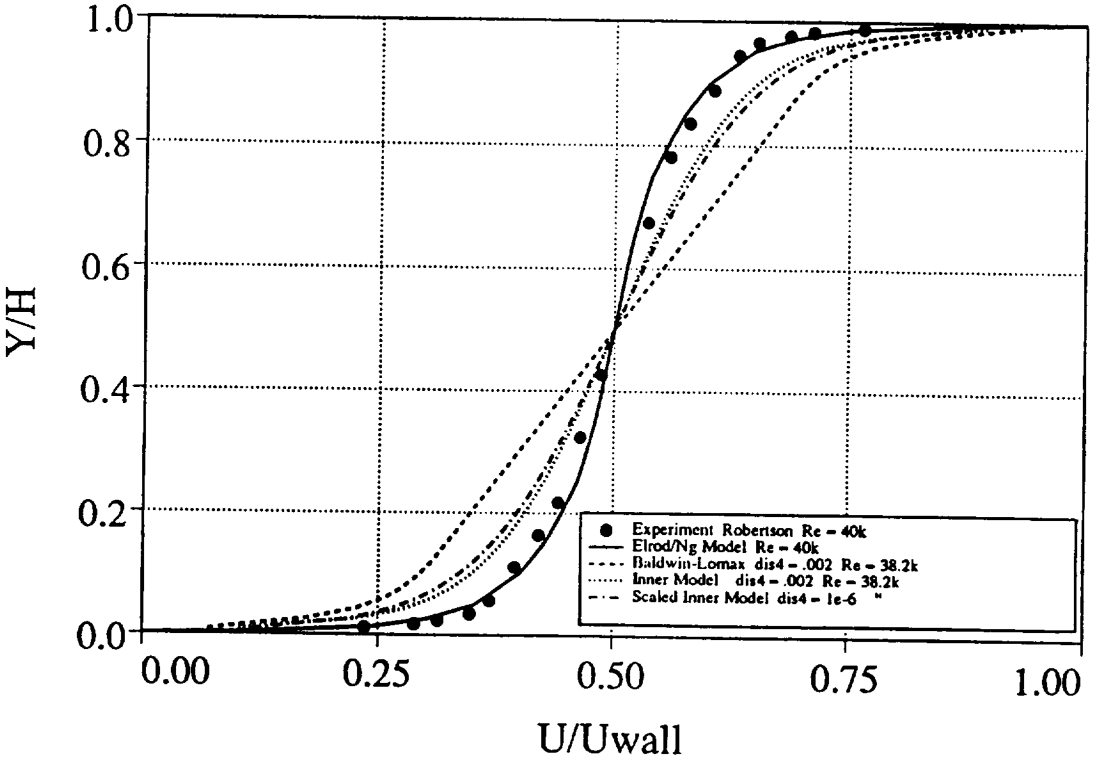

Figure 3. The effect of turbulence model on Couette flow velocity profile. Present computations with 60 grid-points.

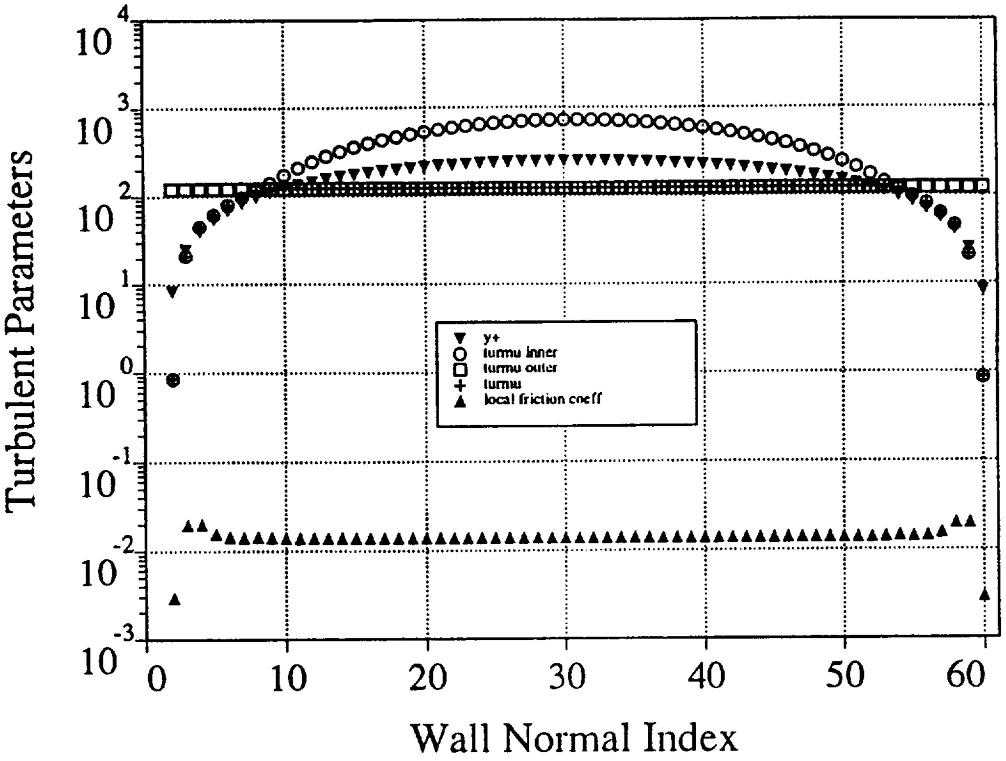

Figure 4. Turbulent parameters for Couette flow at Re = 38,180. with the Baldwin-Lomax model and with 60 grid-points.

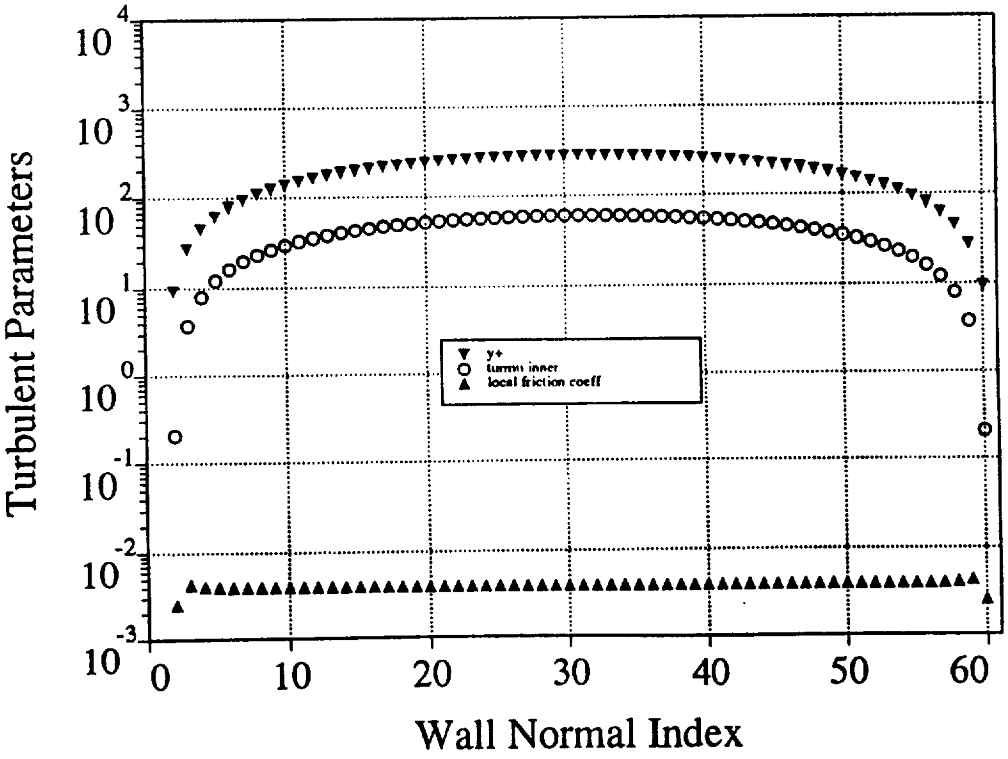

Figure 5. Turbulent parameters for Couette flow at Re = 38,180 with the scaled inner model, with 60 grid-points, and with dis4 = 10^{-6}.

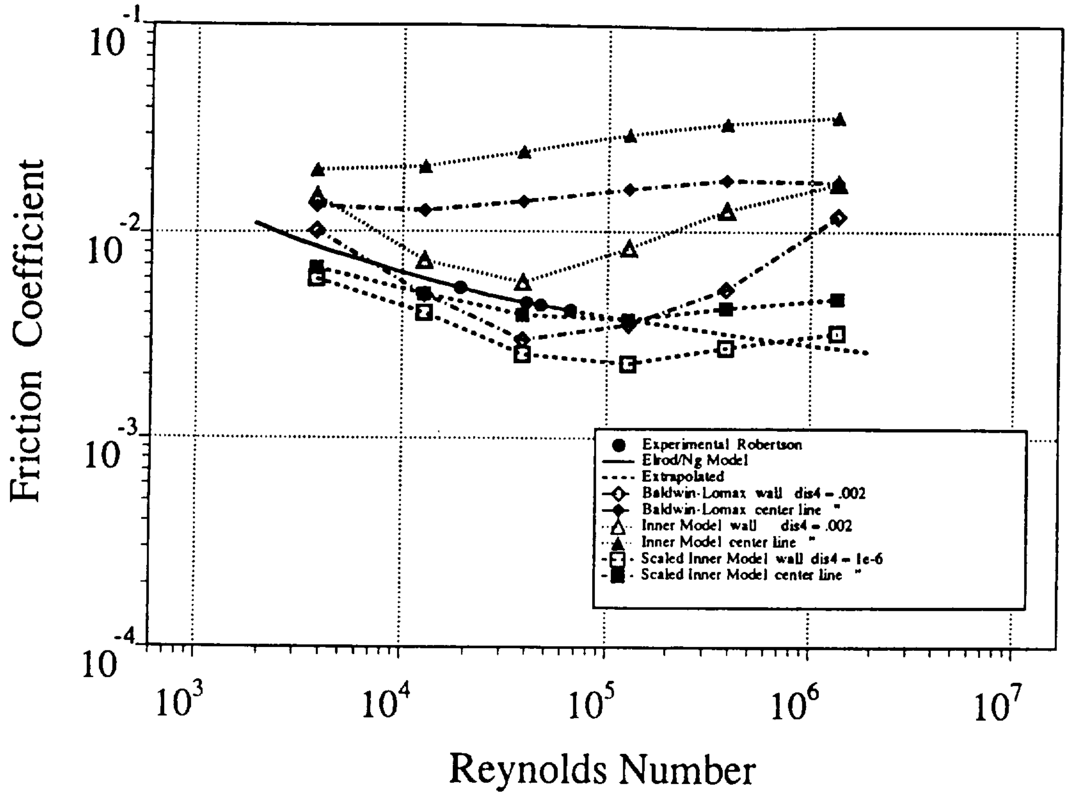

Figure 6. The effect of turbulence model and of numerical dissipation on wall friction and on friction at the centerline, 60 grid-points.

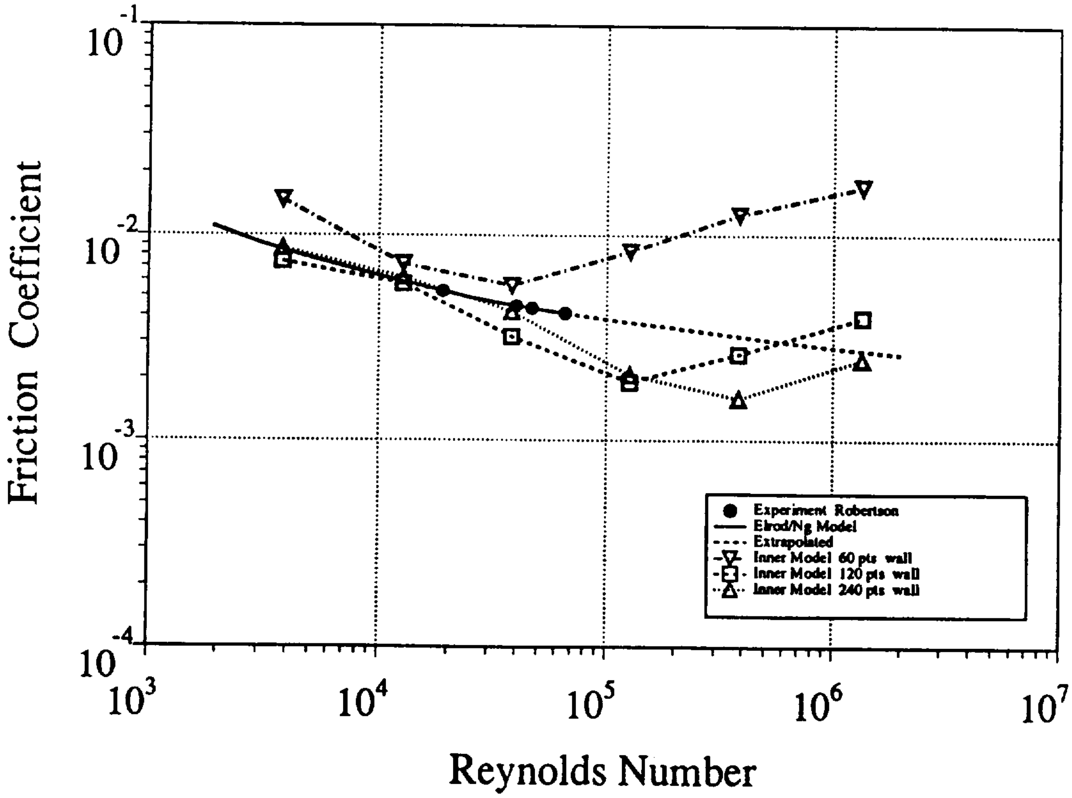

Figure 7. The effect of grid resolution on wall friction with inner model and with dis4 = 0.002.

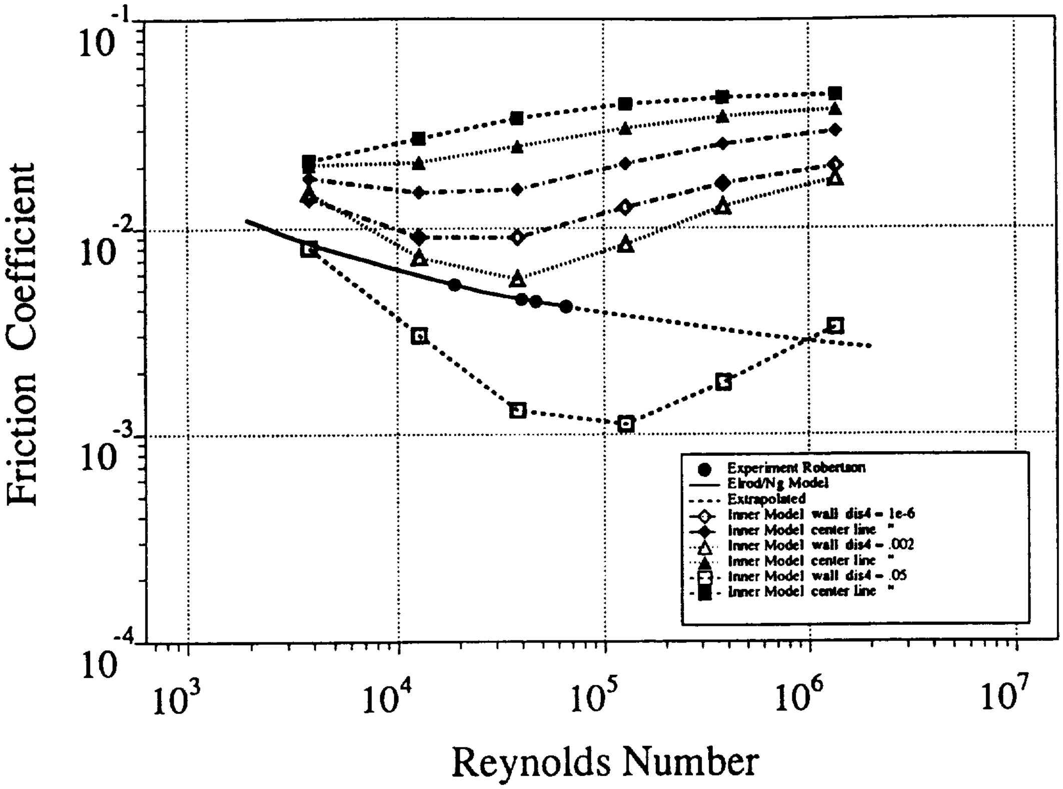

Figure 8. The effect of numerical dissipation on wall friction and on friction at the centerline, 60 grid-points.

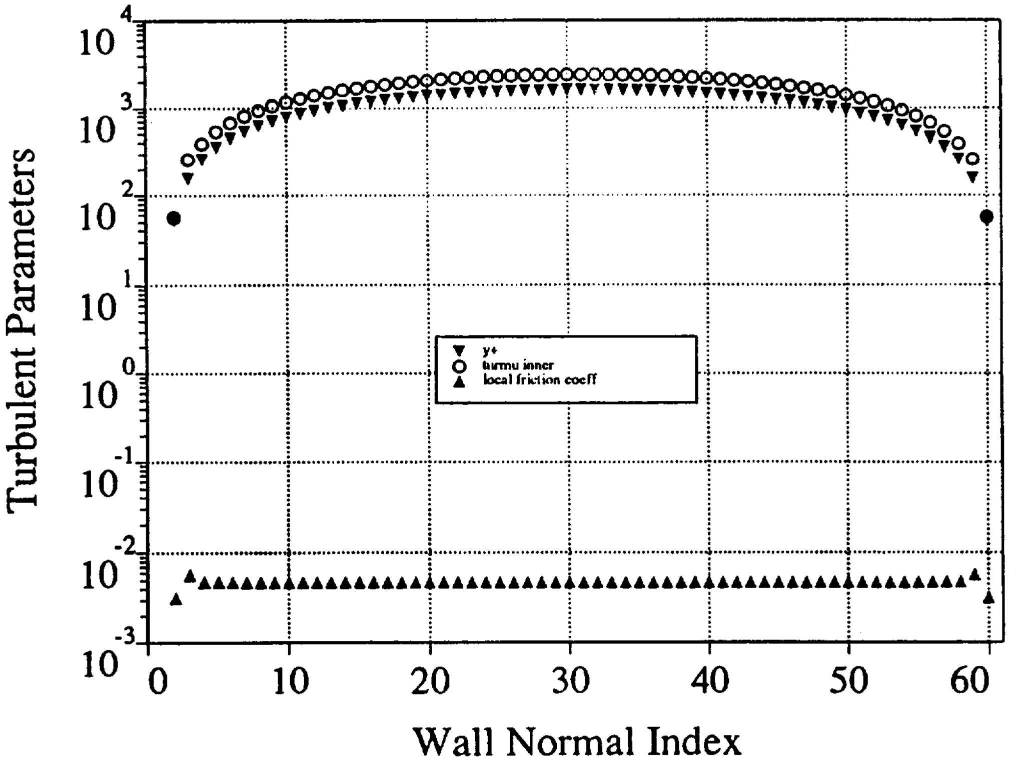

Figure 9. Turbulent parameters for Couette flow at Re = 1,350,000 with the scaled inner model and with 60 grid-points.

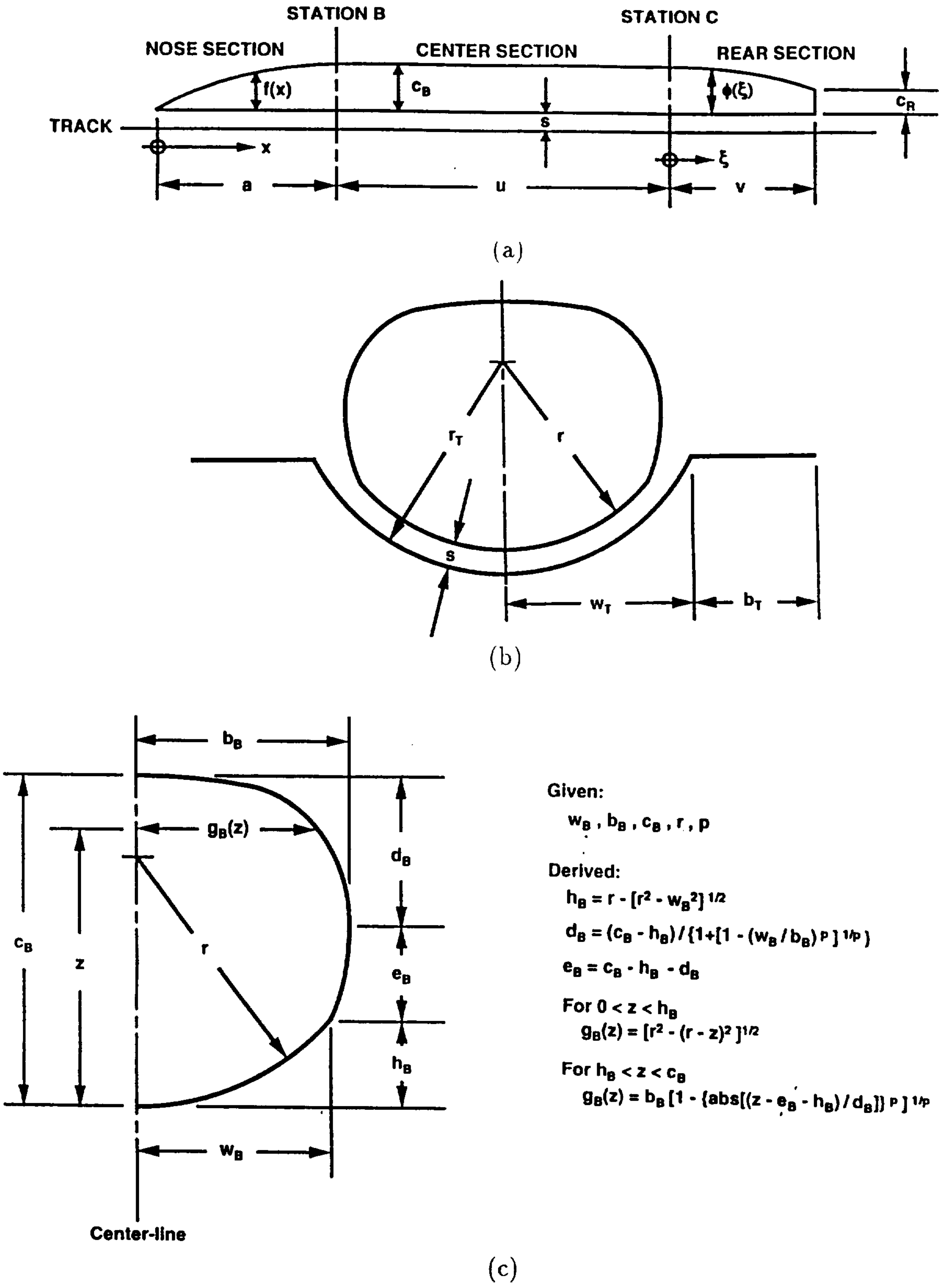
STATION B
STATION C
NOSE SECTION
CENTER SECTION
REAR SECTION
f(x)
c_B
ϕ(ξ)
c_R
TRACK
s
x
ξ
a
u
v
(a)
r_T
r
s
w_T
b_T
(b)
b_B
g_B(z)
d_B
c_B
z
r
e_B
h_B
w_B
Center-line
Given:
w_B, b_B, c_B, r, p
Derived:
h_B = r - [r² - w_B²]^1/2
d_B = (c_B - h_B)/{1+[1 - (w_B/b_B)^p]^1/p}
e_B = c_B - h_B - d_B
For 0 < z < h_B
g_B(z) = [r² - (r - z)²]^1/2
For h_B < z < c_B
g_B(z) = b_B [1 - {abs[(z - e_B - h_B)/d_B]}^p]^1/p
(c)

Figure 10. Magflite vehicle: (a) Side-view in the vertical center-plane; (b) track cross-section; (c) body cross-section at station B. Parameter values: a = 6.10 m, u = 26.25 m, v = 5.00 m, s = 0.15 m, C_B = 2.90 m, C_R = 1.50 m, r = 1.5 m, W_T = 2.05 m, b_T = 1.50 m, r_T = 2.10 m, W_B =1.60 m, b_B = 1.70 m, and p = 3

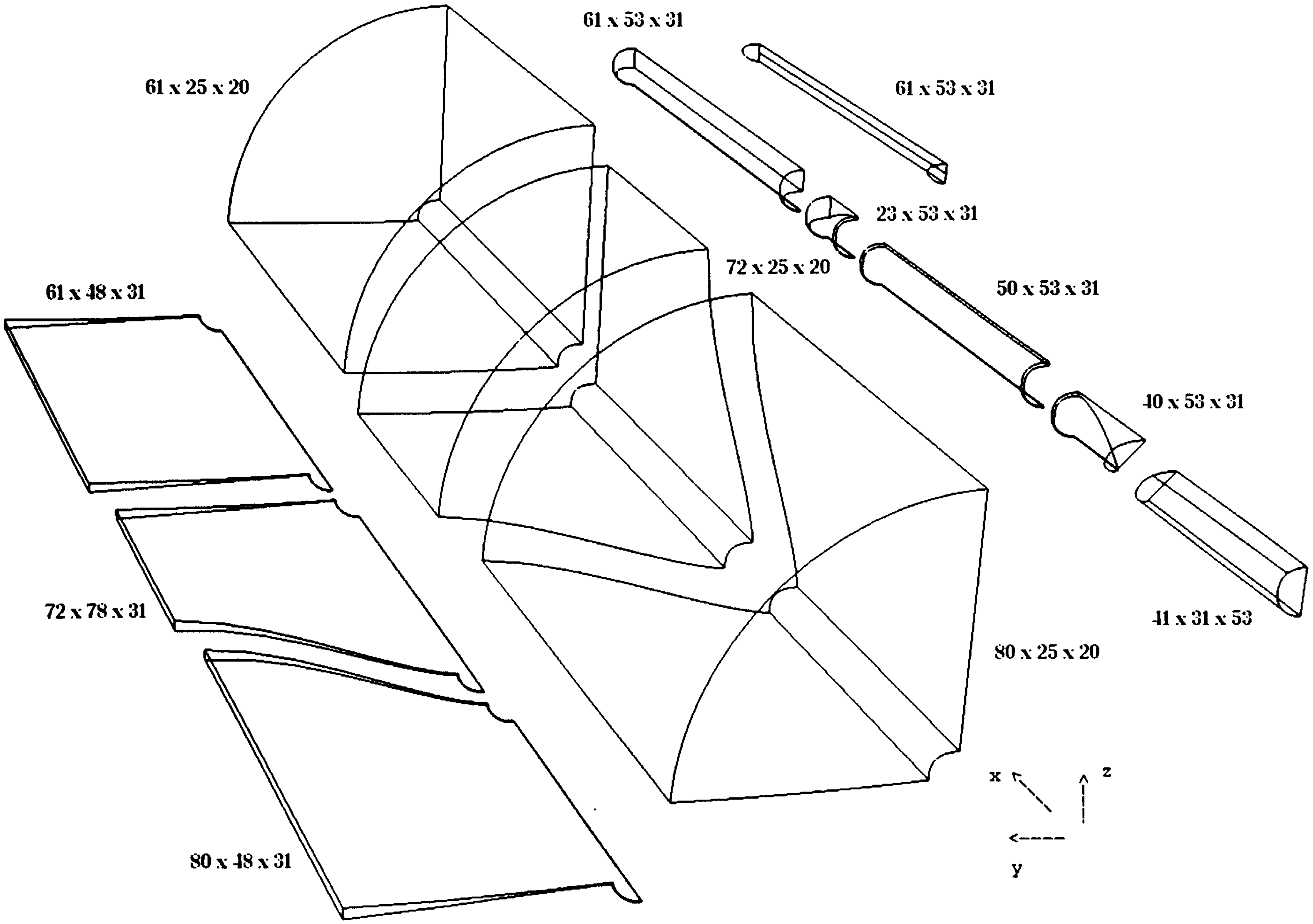
61 x 53 x 31
61 x 25 x 20
61 x 53 x 31
23 x 53 x 31
72 x 25 x 20
50 x 53 x 31
61 x 48 x 31
40 x 53 x 31
41 x 31 x 53
72 x 78 x 31
80 x 25 x 20
x
z
y
80 x 48 x 31

Figure 11. Twelve-zone blocking scheme.

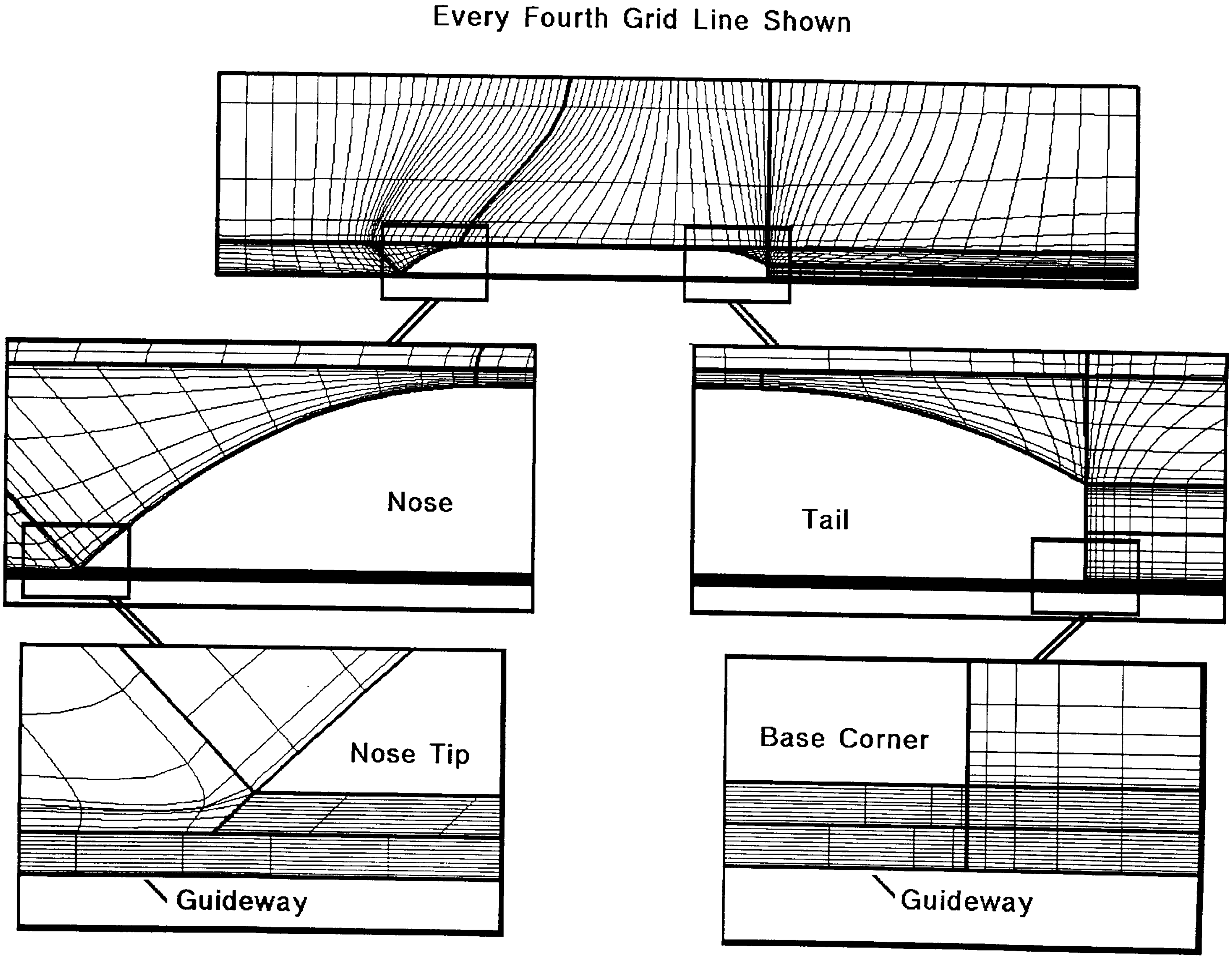
Every Fourth Grid Line Shown
Nose
Tail
Nose Tip
Guideway
Base Corner
Guideway

Figure 12. Patched grid in the symmetry plane of Magflite vehicle.

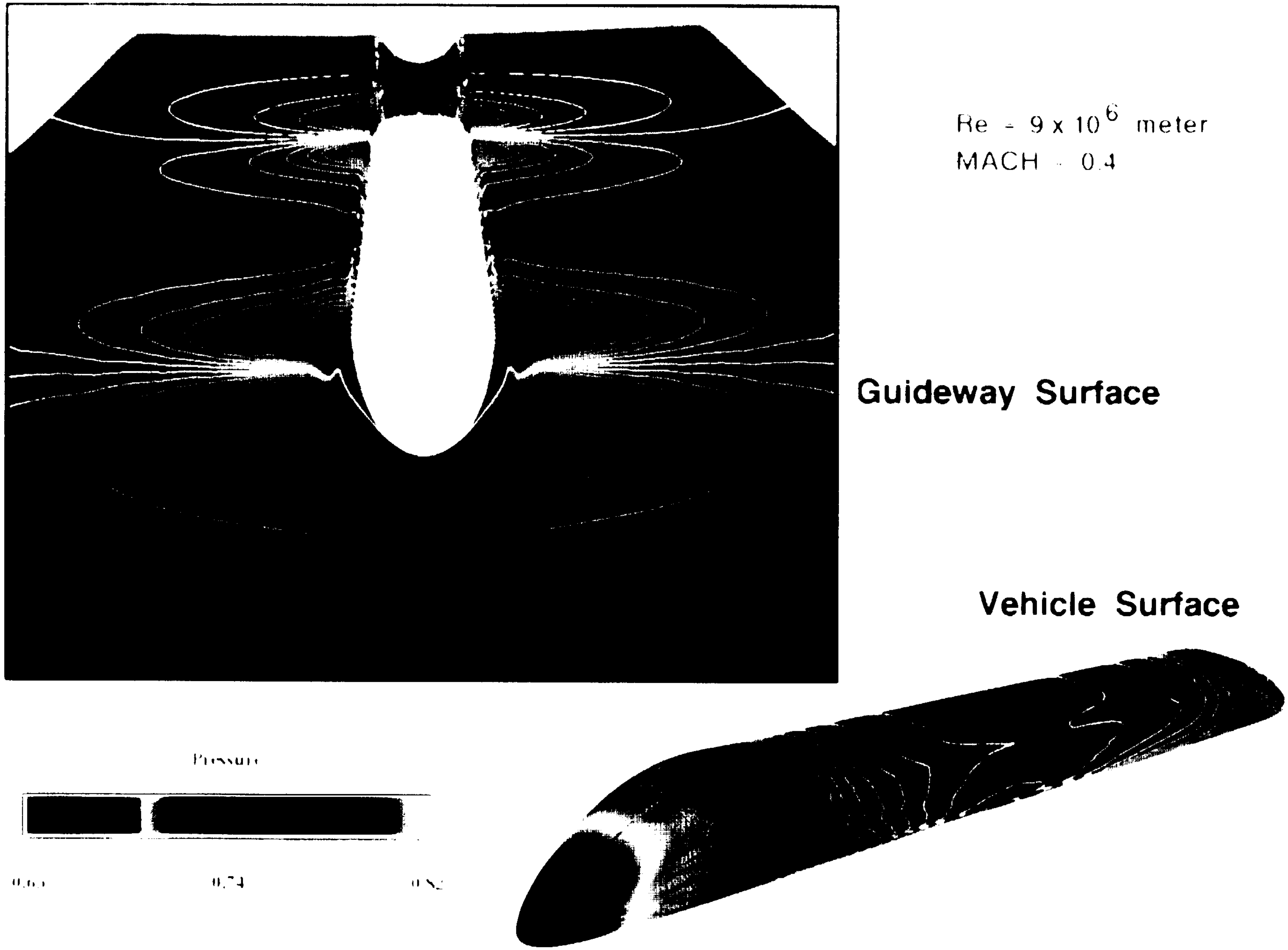
Re = 9 x 10^6 meter
MACH = 0.4
Guideway Surface
Vehicle Surface
Pressure
0.65
0.74
0.82

Figure 15. Pressure contours on guideway surface and vehicle surface.

ORIGINAL PAGE
COLOR PHOTOGRAPH

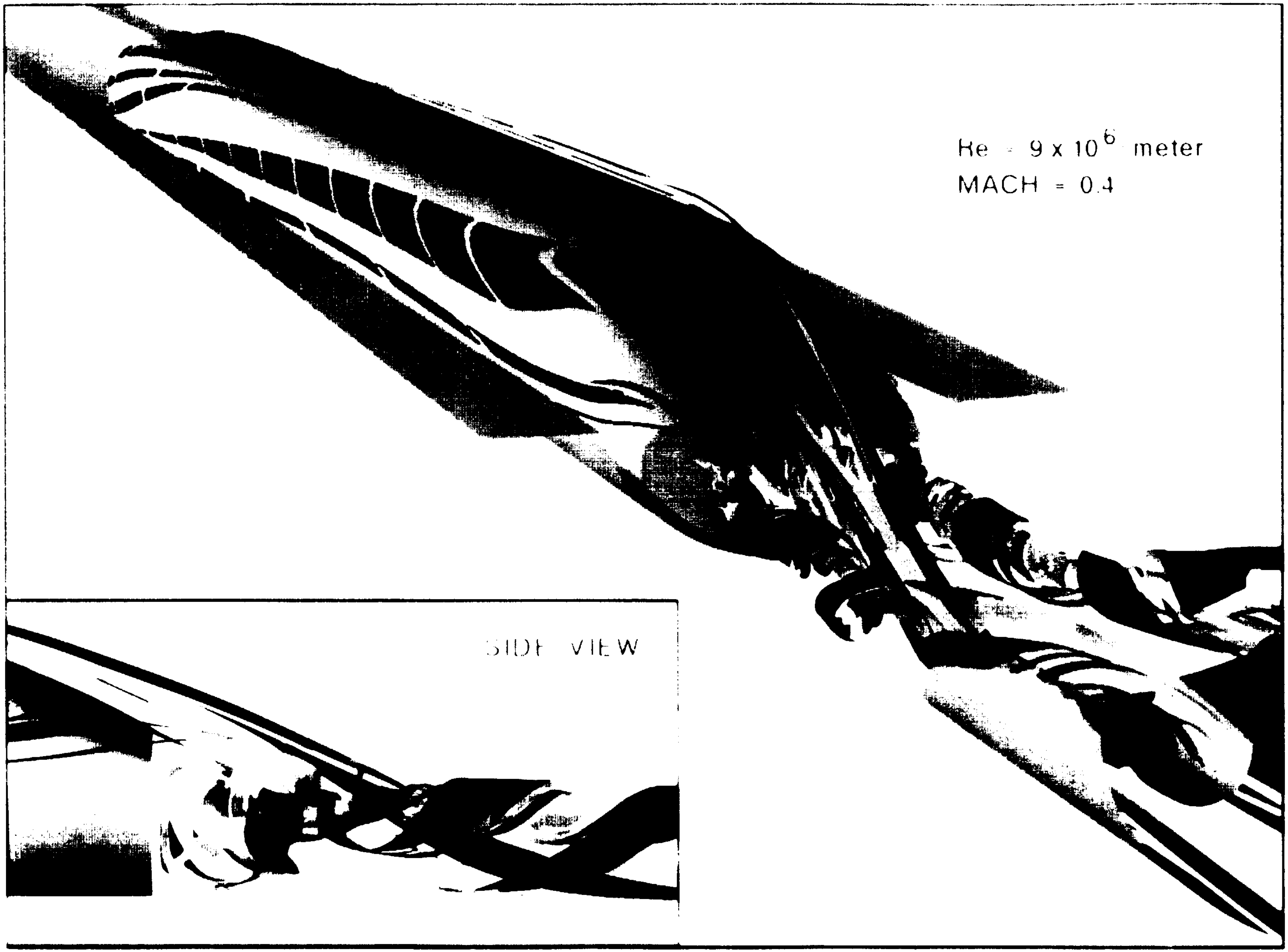
Re = 9 x 10^6 meter
MACH = 0.4
SIDE VIEW

Figure 11. Stream surfaces emanating from the nose and the base region of the vehicle

ORIGINAL PAGE
COLOR PHOTOGRAPH

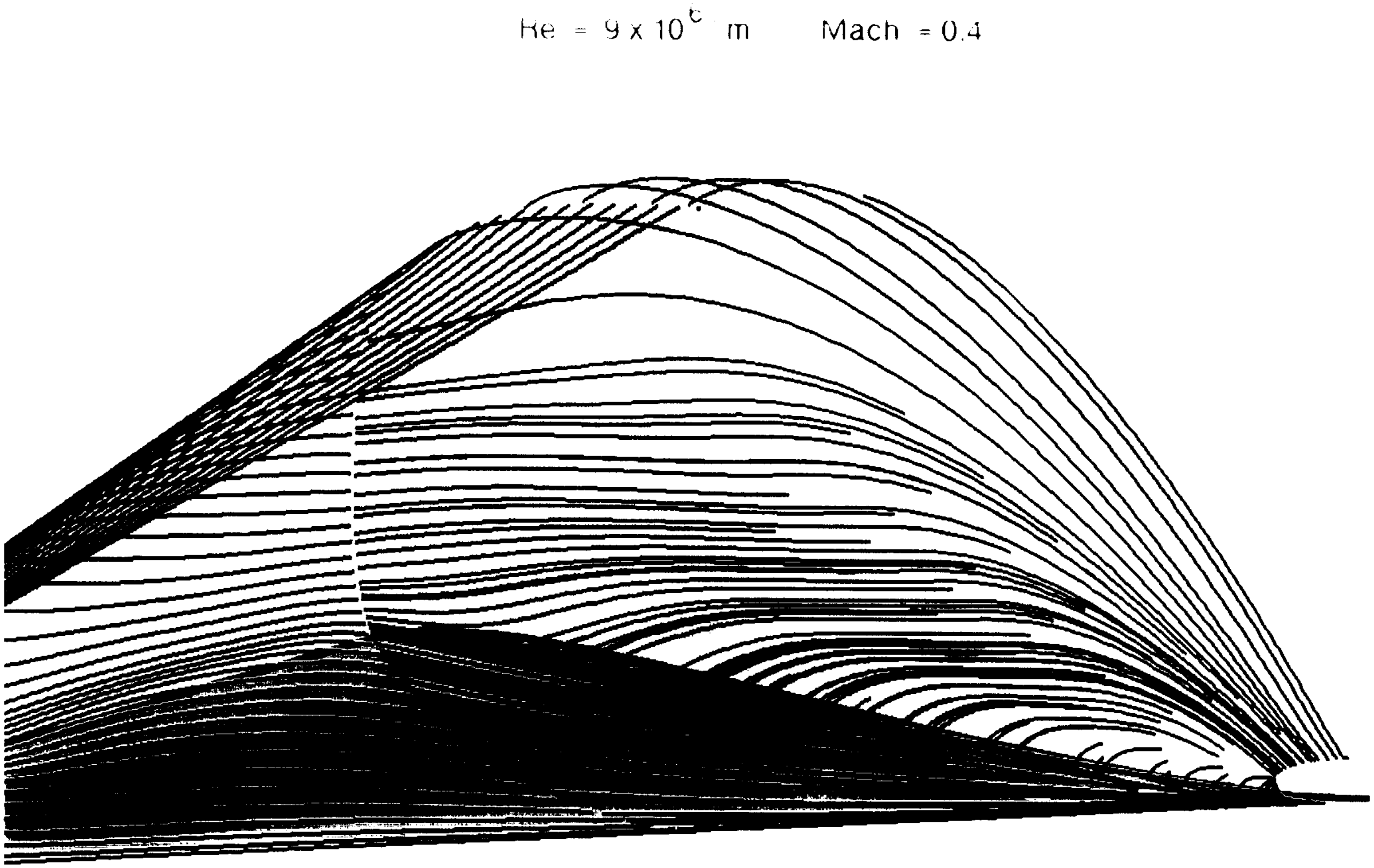
Re = 9×10^6 m Mach = 0.4

Figure 15. Surface particle traces near the nose region

ORIGINAL PAGE
COLOR PHOTOGRAPH

Re = 9×10^6 m Mach = 0.4

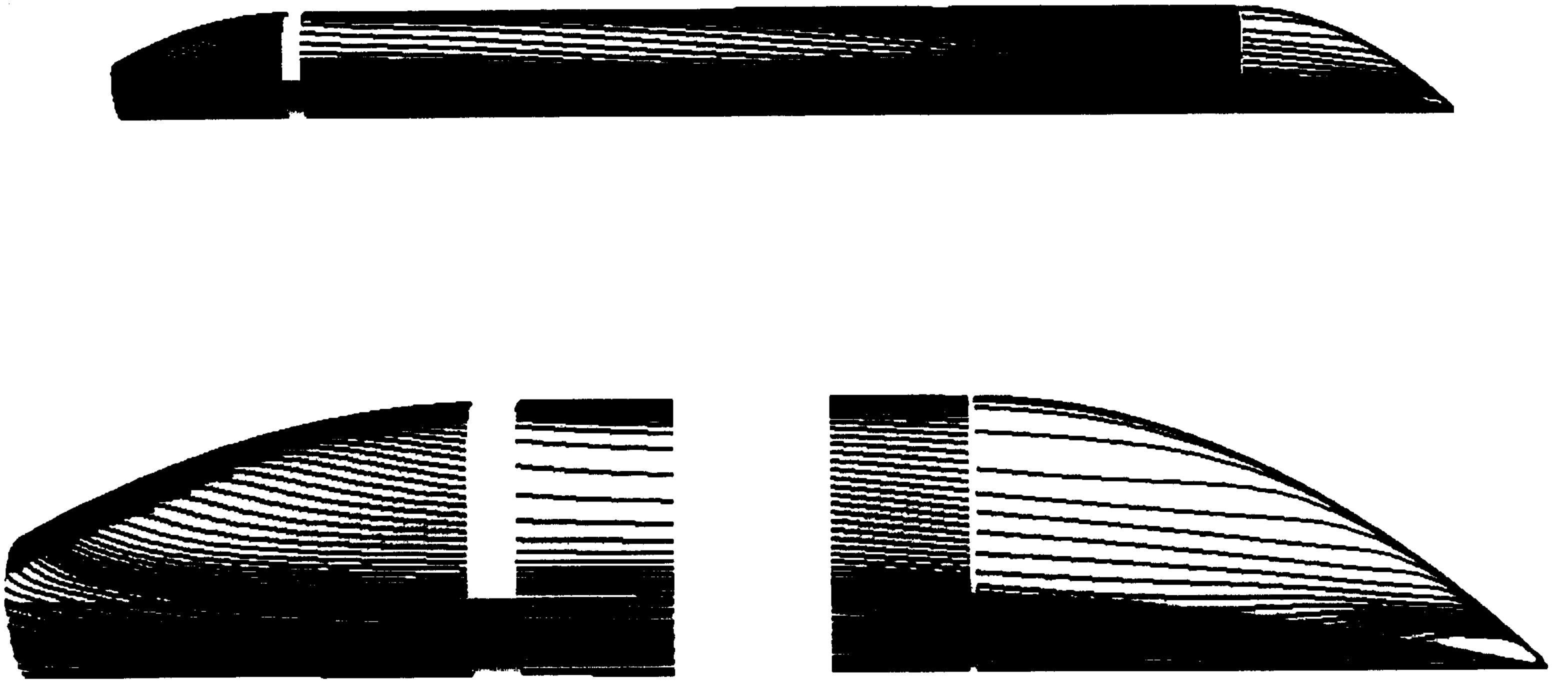

Tail Detail

Nose Detail

[illegible]

ORIGINAL PAGE
COLOR PHOTOGRAPH

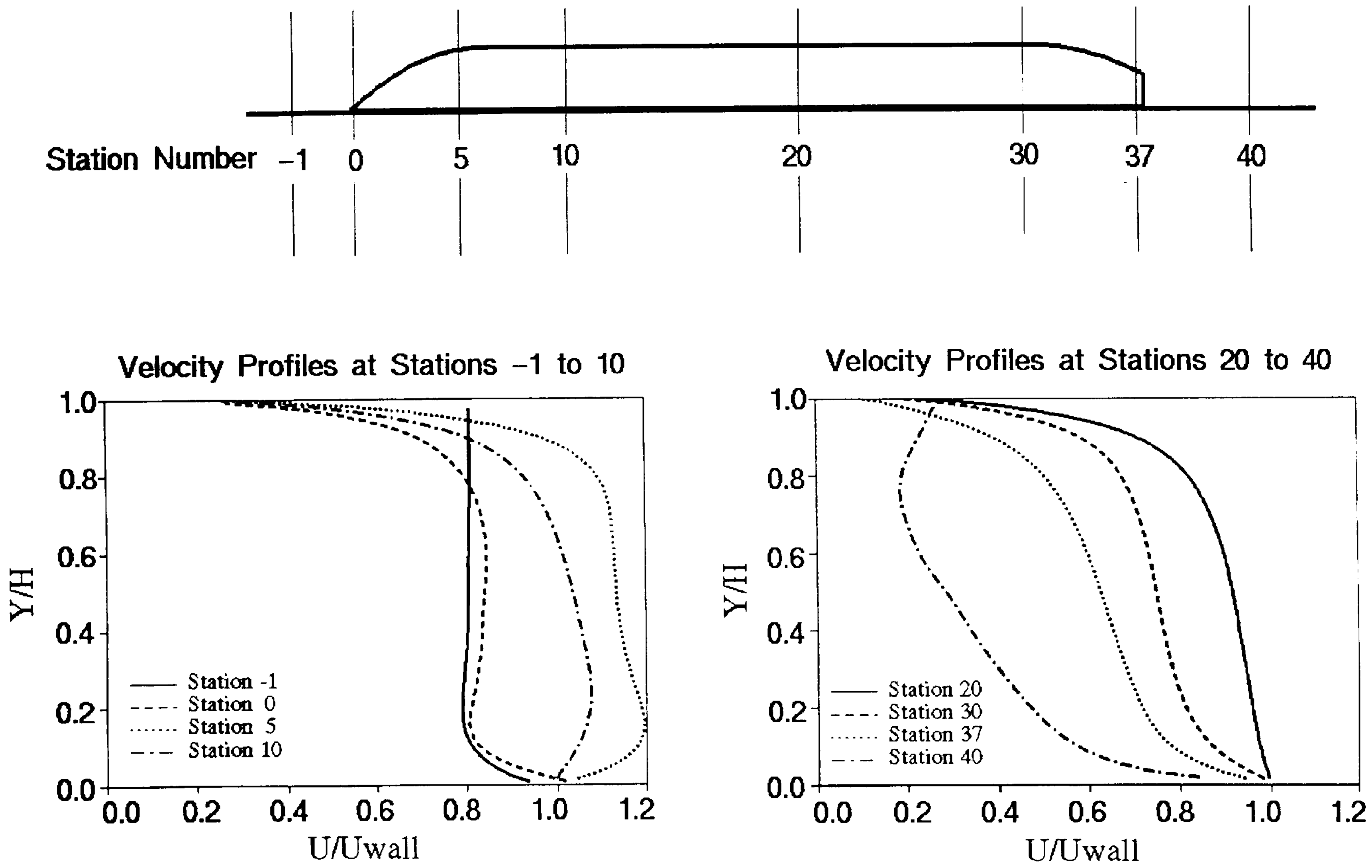

Figure 17. Normalized velocity profiles in the gap symmetry plane.